Winter 2009

Modeling and Simulation of Coaxial Helicopter Rotor Aerodynamics

Murat Gecgel

Old Dominion University

Recommended Citation

Gecgel, Murat. "Modeling and Simulation of Coaxial Helicopter Rotor Aerodynamics" (2009). Doctor of Philosophy (PhD), Dissertation, Mechanical & Aerospace Engineering, Old Dominion University, DOI: 10.25777/n6nw-ng82
https://digitalcommons.odu.edu/mae_etds/53

MODELING AND SIMULATION OF COAXIAL HELICOPTER ROTOR AERODYNAMICS

by

Murat Gecgel
B.S. August 1995, Turkish Air Force Academy, Turkey
M.S. September 2003, Middle East Technical University, Turkey

A Dissertation Submitted to the Faculty of
Old Dominion University in Partial Fulfillment of the
Requirement for the Degree of

DOCTOR OF PHILOSOPHY

AEROSPACE ENGINEERING

OLD DOMINION UNIVERSITY
December 2009

Approved by:

Dr.Oktay Baysal (Director)

Dr.Osama Kandil (Member)

Dr.Ali Beskok (Member)

Dr.Abdurrahman Hacioglu (Member)

ABSTRACT

MODELING AND SIMULATION OF COAXIAL HELICOPTER ROTOR AERODYNAMICS

Murat Gecgel
Old Dominion University, 2009
Director: Dr. Oktay Baysal

A framework is developed for the computational fluid dynamics (CFD) analyses of a series of helicopter rotor flowfields in hover and in forward flight. The methodology is based on the unsteady solutions of the three-dimensional, compressible Navier-Stokes equations recast in a rotating frame of reference. The simulations are carried out by solving the developed mathematical model on hybrid meshes that aim to optimally exploit the benefits of both the structured and the unstructured grids around complex configurations. The computer code is prepared for parallel processing with distributed memory utilization in order to significantly reduce the computational time and the memory requirements.

The developed model and the simulation methodology are validated for single-rotor-in-hover flowfields by comparing the present results with the published experimental data. The predictive merit of different turbulence models for complex helicopter aerodynamics are tested extensively. All but the k–ω and LES results demonstrate acceptable agreement with the experimental data. It was deemed best to use the one-equation Spalart-Allmaras turbulence model for the subsequent rotor flowfield computations.

First, the flowfield around a single rotor in forward flight is simulated. These time–accurate computations help to analyze an adverse effect of increasing the forward flight speed. A dissymmetry of the lift on the advancing and the retreating blades is observed for six different advance ratios. Since the coaxial rotor is proposed to mitigate the dissymmetry, it is selected as the next logical step of the present investigation.

The time–accurate simulations are successfully obtained for the flowfields generated by first a hovering then a forward-flying coaxial rotor. The results for the coaxial rotor in forward flight verify the aerodynamic balance proposed by the previously published advancing blade concept. The final set of analyses aims to investigate if the gap between the two rotors of the coaxial configuration has any significant effect on the generated forces. The present results indicate either little or no such effect on the lift.

Bu günlere gelmemde çok büyük emekleri olan sevgili büyükbabam ve babaanneme

ACKNOWLEDGMENTS

I thank to my advisor Dr. Oktay Baysal, who, with his wisdom not only mentored me, but has also presented a constant example of how to be a director and a researcher.

A sincere and special thank you is owed to my committee members, Dr. Osama Kandil, Dr. Ali Beskok, and Dr. Abdurrahman Hacioglu for their valuable guidance and supports.

Among all the many friends I made in Norfolk, I would like to particularly thank Dr. Isık Ali Ozcer. Thank you for providing help in all times of need.

I appreciate the friendship of my friends, Yavuz Nacakli, Bayram Celik, Bedri Yagiz, Omer San, Eren Yalcin and Murat Barisik for the good times that I shall never forget.

I also thank my family, who always motivated and supported me throughout this journey. I could never come to this point without their love.

TABLE OF CONTENTS

Page

LIST OF FIGURES....................x

LIST OF SYMBOLS....................xvi

CHAPTER

I. INTRODUCTION....................1
- 1.1 Introduction to Helicopter Aerodynamics....................3
- 1.2 Dynamics of a Rotor Blade....................4
- 1.3 Tip Vortices and Rotor Wakes....................6
  - 1.3.1 Airplane Wakes....................12
  - 1.3.2 Helicopter Wake System....................13
  - 1.3.3 Challenges in Modeling the Tip Vortices....................14
  - 1.3.4 BVI-Generated Noise and Vibration....................15
- 1.4 Understanding the Flow Physics....................18
- 1.5 Rotor Configurations....................21
- 1.6 Fully Articulated Rotors....................29
- 1.7 Semi–Rigid (Teetering) Rotors....................31
- 1.8 Rigid Rotors....................31

II. BACKGROUND AND LITERATURE SURVEY....................32
- 2.1 Helicopter Simulations....................32
  - 2.1.1 Potential Flow Simulations....................33
  - 2.1.2 Euler and RANS Simulations....................35
  - 2.1.3 Hybrid Solvers....................40
  - 2.1.4 Fourier–Based Time Integration Solvers....................43
  - 2.1.5 Wind Tunnel Experiments....................44
- 2.2 Coaxial Rotors Studies....................44

III. MOTIVATION AND OBJECTIVES 53
- 3.1 Motivation 53
- 3.2 Objectives 54

IV. MATHEMATICAL FORMULATION AND METHODOLOGY 56
- 4.1 Governing Equations 56
- 4.2 An Overview of Flow Solvers 61
  - 4.2.1 Pressure–Based Solver 62
    - 4.2.1.1 The Pressure–Based Segregated Algorithm 62
    - 4.2.1.2 The Pressure-Based Coupled Algorithm 64
  - 4.2.2 Density–Based Solver 65
- 4.3 Finite Volume Method 69
- 4.4 Boundary Conditions 73

V. VALIDATION OF THE METHODOLOGY 75
- 5.1 Caradonna–Tung Rotor in Hover 75
- 5.2 Computational Domain and Grid Topology 77
- 5.3 Numerical Method of Solution 86
- 5.4 Non–Lifting Case 87
- 5.5 Lifting Cases 91
  - 5.5.1 M_{tip}=0.439 Case 91
  - 5.5.2 M_{tip}=0.877 Case 94

VI. RESULTS AND DISCUSSION 98
- 6.1 Comparison of Turbulence Models 98
  - 6.1.1 The Spalart-Allmaras Model 98
  - 6.1.2 The Standard K-ε Model 101
  - 6.1.3 The RNG K-ε Model 103
  - 6.1.4 The Realizable K-ε Model 105
  - 6.1.5 The Standard K-ω Model 107
  - 6.1.6 Shear-Stress Transport (SST) K-ω Model 109
  - 6.1.7 The Large Eddy Simulation (LES) Model 111
- 6.2 Single Rotor Simulations 114

- 6.2.1 Mesh Generation for Single Rotors 115
- 6.2.2 Single Rotor in Hover 120
  - 6.2.2.1 $\alpha=0^{\circ}$ cases 120
  - 6.2.2.2 $\alpha=8^{\circ}$ cases 126
- 6.2.3 Single Rotor in Forward Flight 131

6.3 Coaxial Rotor Simulations 138
- 6.3.1 Numerical Method of Solution 142
- 6.3.2 Mesh Generation for Coaxial Rotors 142
- 6.3.3 Coaxial Rotor in Forward Flight 146
- 6.3.4 Effect of Rotor Separation Distance on Lift 156

VII. CONCLUSIONS AND RECOMMENDATIONS 162
- 7.1 Conclusions 162
- 7.2 Recommendations as Future Work 164

REFERENCES 167

VITA 179

LIST OF FIGURES

Figure Page

1.1 Flapping, lead-lag, and feathering motion of a rotor blade 5

1.2 Forces acting on a blade about the flap hinge 5

1.3 Design of modern rotors requires detailed structural dynamics (i.e. finite-element based) analysis to minimize aeromechanical instabilities and fatigue stresses 6

1.4 Typical flow phenomena found on a helicopter in forward flight 7

1.5 A NASA study on wingtip vortices produced these pictures of smoke in the wake of an aircraft, clearly illustrating the size and power of the vortices produced 8

1.6 Condensation in the cores of wingtip vortices from an F-15E as it disengages from a KC-10 Extender following midair refueling 8

1.7 Schematic illustrating the effects of the positive straining or “stretching” of a vortex filament when subjected to a velocity gradient 9

1.8 Effects of viscous diffusion of a tip vortex filament 10

1.9 Proposed theory for the generation of a core axial velocity 11

1.10 Tip vortices trailing the rotor blades of Bell AH-1 Cobra 12

1.11 Wake structure of a helicopter rotor. (a) Baseline case: rotor operates in free air. (b) Ground effect: Rotor operates in the presence of ground, which stretches the vortex filaments 14

1.12 Most common BVI events: (a) almost parallel interactions; (b) almost perpendicular interactions; and (c) oblique collision 16

1.13 Direct collision between a blade and a vortex. 16

1.14 Locations of BVI on a four-bladed rotor operating in forward flight 17

1.15 Experimental vs. Computational BVI M=0.5 17

1.16 Sources of rotor vibration 18

1.17 Cross-flow streamlines 19

1.18 Vortex formation along span wise section of a simple fixed wing 20

1.19 Ah-64 A/D Apache Attack Helicopter 21

1.20 Mil V-12, largest helicopter in the world 22

1.21 Tandem rotor design of the MH-47E Chinook 23

1.22 An example of a coaxial rotor: Russian Kamov-50 Alligator 24

1.23 Sikorsky X2 Technology™ Demonstrator 25

1.24 A schematic of the Advancing Blade Concept 26

1.25 Performance comparison of different helicopter types 27

1.26 Comparison of aerodynamic quality in hover 28

2.1 Test conditions for Harrington's experiment 45

2.2 Scale effect on Rotor 1 performance at 327 ft/sec, H/D=0.093 46

2.3 Effect of solidity on rotor figure of merit 46

2.4 Experimental results and equivalent solidity single rotor theory for level flight. (coaxial)=0.054, (single)=0.027, H/D=0.093 47

2.5 Schematic of the advancing blade concept 48

2.6 Comparison of theoretical and experimental static-thrust performance of model ABC rotor, H/D not reported 49

2.7 Coaxial rotor in a wind tunnel 52

4.1 Flowcharts of Segregated and Coupled Algorithms 65

4.2 Flowchart of Density–Based Algorithm 67

4.3 Typical hexahedral cell 71

5.1 a) Wake of a single rotor blade, (b) Experimental set-up of Caradonna-Tung two-bladed model rotor in hover 75

5.2 (a) Geometry of Caradonna-Tung rotor (α=8°), (b) Caradonna-Tung rotor blade dimensions 76

5.3 (a) Inner and outer blocks of unstructured computational mesh, (b) Triangular surface mesh on the blade 80

5.4 Topology of unstructured mesh for Caradonna–Tung rotor 81

5.5 Grid points on the modeled blade surface 83

5.6 Structured block around Caradonna–Tung rotor blade 83

5.7 Hybrid block around Caradonna–Tung rotor 84

5.8 Cross section of the structured block in span wise direction 84

5.9 Cross section of structured block in stream wise direction 85

5.10 Mesh topology near tip region 85

5.11 Pressure contours on the blade and the rotor surfaces, inviscid, hover, M_{tip}=0.52, Ω=132.9 rad/s, α=0°,Re=2.47×10^6 87

5.12 (a) Pressure contours at five stations (r/R=0.5, 0.68, 0.80, 0.89 and 0.96) span wise stations, (b) Pressure contours at r/R=0.89, inviscid, hover, Ω=132.9 rad/s, M_{tip}=0.52, α=0°,Re=2.47×10^6 87

5.13 C_p distributions at three span wise locations (r/R=0.5, 0.80 and 0.96), inviscid, hover, $\alpha=0^{o}$, $M_{tip}=0.52$, $\Omega=132.9$ rad/s, $Re=2.47\text{x}10^{6}$ 88

5.14 C_p distributions at three span wise locations (r/R=0.5, 0.80 and 0.96), laminar, hover, $\alpha=0^{o}$, $M_{tip}=0.52$, $\Omega=132.9$ rad/s, $Re=2.47\text{x}10^{6}$ 90

5.15 Pressure contours on the blade and the rotor surfaces, inviscid, lifting, $M_{tip}=0.439$, $\Omega=112.2$ rad/s, $\alpha=8^{o}$, $Re=2.11\text{x}10^{6}$ 91

5.16 Pressure contours on the blade and the rotor surfaces, laminar, lifting, $M_{tip}=0.439$, $\Omega=112.2$ rad/s, $\alpha=8^{o}$, $Re=2.11\text{x}10^{6}$ 91

5.17 C_p distributions at three span wise locations (r/R=0.5, 0.80 and 0.96), inviscid, hover, $\alpha=0^{o}$, $M_{tip}=0.439$, $\Omega=112.2$ rad/s, $Re=2.11\text{x}10^{6}$ 92

5.18 C_p distributions at three span wise locations (r/R=0.5, 0.80 and 0.96), laminar, hover, $\alpha=0^{o}$, $M_{tip}=0.439$, $\Omega=112.2$ rad/s, $Re=2.11\text{x}10^{6}$ 93

5.19 Pressure contours on the blade and the rotor surfaces, inviscid, lifting, $M_{tip}=0.877$, $\Omega=224.2$ rad/s, $\alpha=8^{o}$, $Re=4.22\text{x}10^{6}$ 94

5.20 Pressure contours on the blade and the rotor surfaces, laminar, lifting, $M_{tip}=0.877$, $\Omega=224.2$ rad/s, $\alpha=8^{o}$, $Re=4.22\text{x}10^{6}$ 94

5.21 C_p distributions at 3 span wise locations (r/R=0.5, 0.80 and 0.96), inviscid, hover, $\alpha=8^{o}$, $M_{tip}=0.877$, $\Omega=224.2$ rad/s, $Re=4.22\text{x}10^{6}$ 95

5.22 C_p distributions at 3 span wise locations (r/R=0.5, 0.80 and 0.96), laminar, hover, $\alpha=8^{o}$, $M_{tip}=0.877$, $\Omega=224.2$ rad/s, $Re=4.22\text{x}10^{6}$ 96

6.1 Pressure contours on the blade and the rotor surfaces, Spalart–Allmaras, lifting, $M_{tip}=0.877$, $\Omega=224.2$ rad/s, $\alpha=8^{o}$, $Re=4.22\text{x}10^{6}$ 99

6.2 C_p distributions at three span wise locations (r/R=0.5, 0.80 and 0.96), Spalart–Allmaras, hover, $\alpha=8^{o}$, $M_{tip}=0.877$, $\Omega=224.2$ rad/s, $Re=4.22\text{x}10^{-6}$ 100

6.3 Pressure contours on the blade and the rotor surfaces. Standard k–ε, lifting, $M_{tip}=0.877$, $\Omega=224.2$ rad/s, $\alpha=8^{o}$, $Re=4.22\text{x}10^{6}$ 101

6.4 C_p distributions at three span wise locations (r/R=0.5, 0.80 and 0.96), Standard k–ε, hover, $\alpha=8^{o}$, $M_{tip}=0.877$, $\Omega=224.2$ rad/s, $Re=4.22\text{x}10^{6}$ 102

6.5 Pressure contours on the blade and the rotor surfaces, RNG k–ε, lifting, $M_{tip}=0.877$, $\Omega=224.2$ rad/s, $\alpha=8^{o}$, $Re=4.22\text{x}10^{6}$ 103

6.6 C_p distributions at three span wise locations (r/R=0.5, 0.80 and 0.96), RNG k–ε, hover, $\alpha=8^{o}$, $M_{tip}=0.877$, $\Omega=224.2$ rad/s, $Re=4.22\text{x}10^{6}$ 104

6.7 Pressure contours on the blade and the rotor surfaces, Realizable k–ε, lifting, $M_{tip}=0.877$, $\Omega=224.2$ rad/s, $\alpha=8^{o}$, $Re=4.22\text{x}10^{6}$ 105

6.8 C_p distributions at three span wise locations (r/R=0.5, 0.80 and 0.96), Realizable k–ε, hover, $\alpha=8^{o}$, $M_{tip}=0.877$, $\Omega=224.2$ rad/s, $Re=4.22\text{x}10^{6}$ 106

6.9 Pressure contours on the blade and the rotor surfaces, Standard *k-ω*, lifting, M_{tip}=0.877, Ω=224.2 rad/s, α=8°, Re=4.22x10^6 107

6.10 C_p distributions at three span wise locations (r/R=0.5, 0.80 and 0.96), Realizable *k-ω*, hover, α=8°, M_{tip}=0.877, Ω=224.2 rad/s, Re=4.22x10^6 108

6.11 Pressure contours on the blade and the rotor surfaces, SST *k-ω*, lifting, M_{tip}=0.877, Ω=224.2 rad/s, α=8°, Re=4.22x10^6 109

6.12 C_p distributions at three span wise locations (r/R=0.5, 0.80 and 0.96), SST *k-ω*, hover, α=8°, M_{tip}=0.877, Ω=224.2 rad/s, Re=4.22x10^6 110

6.13 Pressure contours on the blade and the rotor surfaces, LES, lifting, M_{tip}=0.877, Ω=224.2 rad/s, α=8°, Re=4.22x10^6 111

6.14 C_p distributions at three span wise locations (r/R=0.5, 0.80 and 0.96), LES, hover, α=8°, M_{tip}=0.877, Ω=224.2 rad/s, Re=4.22x10^6 112

6.15 NACA airfoils used in single rotor simulations 116

6.16 (a) Blade surface grid, (b) Structured block around rotor, (c) Cross-section in span wise direction, (d) Cross-section in stream wise direction 117

6.17 (a) Structured block around rotor, (b) Hybrid block around rotor, (c) Hybrid block, upper view, (d) Hybrid block, lateral view 118

6.18 Mesh topology near tip region 119

6.19 Summary of settings for single rotor simulations 119

6.20 Left; pressure contours at five span wise stations (r/R=0.50, 0.68, 0.80, 0.89 and 0.96), right; pressure contours at r/R=0.89, Spalart-Allmaras, α=0°, Re=2.35x10^6, hover, M_{tip}=0.52 121

6.21 C_p distributions for several NACA airfoils at three span wise stations (r/R=0.50, 0.80 and 0.96), Spalart-Allmaras, hover, M_{tip}=0.52, α=0° 124

6.22 Left; pressure contours at five span wise stations (r/R=0.50, 0.68, 0.80, 0.89 and 0.96), right; pressure contours at r/R=0.89, Spalart-Allmaras, α=8°, Re=2.35x10^6, hover, M_{tip}=0.52 126

6.23 C_p distributions for several NACA airfoils at three span wise stations (r/R=0.50, 0.80 and 0.96), Spalart-Allmaras, hover, M_{tip}=0.52, α=8° 129

6.24 Typical flow phenomena found on a helicopter in forward flight 132

6.25 Surface pressure contours and C_p distributions (r/R=0.89) at different azimuth angles, Spalart–Allmaras, forward flight, η=0.2, M_{tip}=0.52, α=8° 133

6.26 Pressure contours at r/R=0.89, left; retreating blade, right; advancing blade, Spalart–Allmaras, forward flight, η=0.2, M_{tip}=0.52, α=8° 134

6.27 Pressure contours on the rotor, Spalart–Allmaras, Forward Flight, η=0.3, M_{tip}=0.52, α=8° 135

6.28 Pressure contours on the rotor, Spalart–Allmaras, forward flight, $\eta=0.4$, $M_{tip}=0.52$, $\alpha=8^{o}$ 135

6.29 Pressure contours on the rotor, Spalart–Allmaras, forward flight, $\eta=0.5$, $M_{tip}=0.52$, $\alpha=8^{o}$ 136

6.30 Pressure contours on the rotor, Spalart–Allmaras, forward flight, $\eta=0.6$, $M_{tip}=0.52$, $\alpha=8^{o}$ 136

6.31 Pressure coefficient distributions on advancing and retreating blades . 137

6.32 Schematic of the Advancing Blade Concept 140

6.33 Structured block around blade 143

6.34 Structured blocks around lower and upper rotor blades 143

6.35 Hybrid block for lower rotor 144

6.36 Lower and upper rotors and inner interface surface between rotor blocks. 145

6.37 Inner and outer parts of interface surface 146

6.38 Pressure contours on the lower and upper rotors at different time steps, forward flight, $\eta=0.1$, $M_{tip}=0.52$, Spalart–Allmaras 148

6.39 Pressure contours on the lower and upper rotors at different time steps, forward flight, $\eta=0.2$, $M_{tip}=0.52$, Spalart–Allmaras 149

6.40 Pressure contours on the lower and upper rotors at different time steps, forward flight, $\eta=0.3$, $M_{tip}=0.52$, Spalart–Allmaras 150

6.41 Pressure contours on the lower and upper rotors at different time steps, forward flight, $\eta=0.4$, $M_{tip}=0.52$, Spalart–Allmaras 151

6.42 Pressure contours on the lower and upper rotors at different time steps, forward flight, $\eta=0.5$, $M_{tip}=0.52$, Spalart–Allmaras 152

6.43 Pressure contours on the lower and upper rotors at different time steps, forward flight, $\eta=0.6$, $M_{tip}=0.52$, Spalart–Allmaras 153

6.44 Pressure contours on the lower and upper rotors at different time steps, forward flight, $\eta=0.7$, $M_{tip}=0.52$, Spalart–Allmaras 154

6.45 Pressure coefficient distributions at $r/R=0.80$ on the lower and upper rotors, forward flight, $M_{tip}=0.52$, Spalart–Allmaras 155

6.46 Pressure contours on the upper and lower rotors, hover, $H/D=0.18$ 156

6.47 Pressure contours at $r/R=0.89$, left; $\psi=90^{o}$, right; $\psi=270^{o}$, $H/D=0.20$ ... 157

6.48 Interaction between the upper and lower rotors; pressure contours at $r/R=0.89$, $\psi=270^{o}$, $H/D=0.20$ 157

6.49 Development of the boundary layer, $r/R=0.89$, $\psi=270^{o}$ 158

6.50 Pressure contours at different time steps, hover, $M_{tip}=0.52$, Spalart–Allmaras, $H/D=0.22$ 159

6.51 Comparison of pressure coefficient distributions on the lower surface for five H/D values, hover, M_{tip}=0.52, Spalart–Allmaras 160

6.52 Comparison of pressure coefficient distributions on the upper surface for five H/D values, hover, M_{tip}=0.52, Spalart–Allmaras 160

6.53 Pressure coefficient distributions on the upper and lower rotors, H/D=0.18, hover, M_{tip}=0.52, Spalart–Allmaras 161

6.54 Pressure coefficient distributions on the upper and lower rotors, H/D=0.22, hover, M_{tip}=0.52, Spalart–Allmaras 161

LIST OF SYMBOLS

a	local speed of sound
AR	aspect ratio
c	airfoil chord
C_l	lift coefficient
C_d	drag coefficient
C_p	pressure coefficient
D	artificial dissipation term
e	internal energy per unit mass
E	total energy per unit mass
E_r	total roenergy
$\vec{F}$	flux vector
$\vec{F}$, $\vec{G}$, $\vec{H}$	inviscid flux components
$\vec{F}_v$, $\vec{G}_v$, $\vec{H}_v$	viscous flux components
H/D	rotor separation distance
k	coefficient of thermal conductivity

MPI	Message Passing Interface Communication Standart
M_∞	freestream Mach Number
M_{tip}	tip Mach number
P	fluid static pressure
R_∞, R_e	fixed and extrapolated Riemann invariants
$\vec{r}$	position vector
R	gas constant
$\vec{R}$	vector of residuals
Re	Reynolds number
$\vec{S}$	area vector
T	static temperature
$\vec{T}$	rotational sources in inertial frame of reference
$\vec{T}_r$	rotational sources in rotating frame of reference
u, v, w	cartesian components of fluid velocity
u_r, v_r, w_r	cartesian components of relative velocity
$\vec{V}$	fluid velocity vector

$\vec{V}_r$	velocity vector relative to a rotating frame of reference
V	control volume
x, y, z	cartesian coordinates
α	collective pitch angle
δt	local time step
Pr	Prandtl Number
γ	ratio of specific heats
q	conservative quantity
μ	dynamic viscosity
Ω	angular velocity
ρ	fluid density
η	forward flight advance ratio

CHAPTER I

INTRODUCTION

A helicopter is a flying machine with rotating wings (i.e., rotors) to provide lift, propulsion, and control forces that enable the aircraft to hover relative to the ground without forward speed or the ability to fly forward or even backward. The thrust on the rotor(s) is generated by the aerodynamic forces created on the spinning blades. To turn the rotor, power from an engine must be transmitted to the rotor shaft. It is the relatively low amount of power required to lift the machine compared to other vertical takeoff and landing (VTOL) aircraft that makes the helicopter unique. Efficient hovering flight with low power requirements comes about by accelerating a large mass of air at a relatively low velocity; hence, we have the large diameter rotors that are one of the obvious characteristics of helicopters.

In addition, a helicopter must be able to fly forward, climb, cruise at speed, and then descend and come back into a hover for landing. This demanding flight capability comes at a price, including mechanical and aerodynamic complexity and high power requirements, than does a fixed wing aircraft of the same gross weight. All these factors influence the design, acquisition and operational costs of the helicopter. Although it is considered by some to be a basic and somehow cumbersome looking aircraft, the modern helicopter is indeed a machine of considerable engineering sophistication and refinement and plays a unique role in modern aviation provided by no aircraft (Leishman, 2006).

For many years the helicopter has played an important role in both military and civilian air transportation, from troop deployment, offshore air taxis, to traffic reporting and medical emergencies. The usefulness of a helicopter over other aircraft is its ability to perform tasks that fixed wing vehicles cannot, such as vertical takeoff and landing and the capacity to hover. In fact, this

---

The format of this dissertation is based on *ODU Dissertation Template*.

maneuverability is one of the driving forces behind helicopter use, and the ability to operate efficiently for long periods in hover is one of the major design considerations (Leishman, 2006).

The numerical simulation of flows around fixed wings has been reported by many authors and aerodynamic loads could be obtained with relative ease at design conditions. For rotary wings, however, the situation appears to be more complicated and CFD analysis is significantly harder. There are several reasons to contribute to this which can be grouped into two categories. First, the flow physics of a rotating wing is rich in terms of fluid mechanics phenomena. Strong vortices interacting with each other and the rotor blades, formation of a complex spiral wake behind the rotor, transition to turbulence and the wide variation of the Mach and Reynolds numbers around the azimuth are a few of the difficult issues with which CFD methods have to cope.

The second family of problems comes from the strong link between the aerodynamics and dynamics of the rotor blades. It is almost impossible to consider one without the other and the link between the two is the balance of forces acting on the rotor which is dictated by, and at the same time dictates, the loading of the blades. The differences in blade normal velocities on the advancing and retreating sides combined with the requirement that the rotor does not produce a pitching or rolling moment on the helicopter creates the main complicating factor. The pitch and roll moments vanish for a blade incidence that depends on the azimuthal position (a smaller incidence on the advancing side and a larger one on the retreating side) and by introducing a flap hinge that gives the blades freedom to flap up and down. However, the pitch settings of the blade and the flapping deflections are not known in advance and form part of the solution. The above phenomenon is commonly known as the trimming problem and further complicates the numerical simulations of rotors in forward flight (Stejil et al., 2006).

An accurate computation of helicopter rotor flows in both hover and forward flight is a particularly challenging problem due to the inherent difficulties that it entails (Sheffer et al., 1997). Aside from the increased complexity generated by interaction with the tail rotor and the effects of the helicopter body, vibration, other aircraft, buildings and ground effect, the flow induced by the rotor alone (even with only a single blade present) is not easily understood.

The strong nonlinear convective effects can cause turbulence and flow separation, which make the flow problem even more intractable since the flow becomes strongly swirling and time-dependent (Xu and Khalid, 2003). Two aspects of these computations stand out as being particularly complex. On the one hand, a reliable prediction of helicopter hover and forward flight performance is heavily dependent on the proper resolution of the blade/vortex interaction that occurs near the tip region. This interaction has a strong influence on the inflow angles and pressure distributions of the blade's outboard sections. On the other hand, the establishment of a full rotor wake in forward flight is a problem of inherent stiffness due to the varying scales present in the problem. While it is necessary to accurately resolve the turning motion of the blade, a large number of revolutions are required for the establishment of a steady wake pattern (Xu and Khalid, 1997). The complexity of rotor flow, directly influenced by the structure, intensity, and trajectories of its blade tip vortices, represents a challenge for the state-of- the-art helicopter design.

1.1 INTRODUCTION TO HELICOPTER AERODYNAMICS

Uniquely, a helicopter exists to perform tasks that a fixed-wing aircraft cannot perform, specifically the ability to take off and land vertically (VTOL) and to hover. There are four flight regimes in which a helicopter operates. The first is hover, where the thrust produced by the rotor disk exactly offsets the weight of the helicopter. The helicopter remains stationary at some height over the ground.

The second flight regime is vertical climb; additional thrust is produced to move the helicopter upward. Third, there is vertical descent. This flight regime is complicated because of the effects of both upward and downward flows through the rotor disk, which can significantly cause blade vibration. Lastly, there is forward flight, where the rotor disk tilts forward in the direction of the flight to create the thrust that can overcome drag. Although vertical climb and descent represent their own unique and challenging problems, the current work focuses on two of the most important flight regimes of helicopter: hover and forward flight. There are additional issues regarding helicopter simulation that are not addressed in this work but deserve to be mentioned such as blade aeroelasticity, inclusion of the tail rotor and fuselage, and the treatment of a fully articulated rotor.

1.2 DYNAMICS OF A ROTOR BLADE

An accurate prediction of helicopter air loads is also dependent on the dynamic motion of the rotor blades. The blades undergo flap, lead-lag, and feathering motions (Figure 1.3) that will vary in degree depending on the flight state. These motions can be rigid or elastic in nature, as well. Articulated rotors (Figures 1.4 and 1.5) use hinges to allow for rigid flap, lag, and pitch. Hingeless rotors only allow for rigid pitch; the flap and lag motions are elastic in nature. These displacements will vary azimuthally and radially across the rotor disk and will affect the the angle of attack and the inflow velocities seen by the rotor blades.

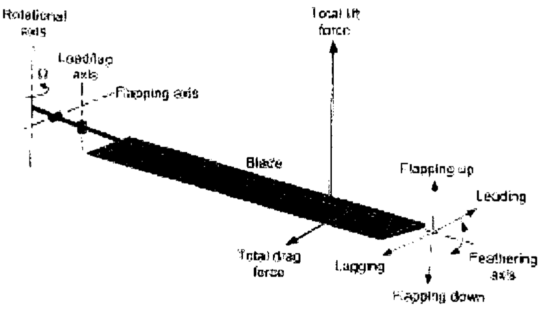

Figure 1.1: Flapping, lead-lag, and feathering motion of a rotor blade.

The flap, lead-lag, and feathering motions of the blade are dependent on a number of different forces. The primary forces that act on a rotor blade (Figures 1.4 and 1.5) are aerodynamic forces (i.e. lift and drag), centrifugal forces (CF), and inertia forces (IF). If the rotor includes damper and/or spring devices, the presence of these components must also be taken into account in any analysis. These blade motions can also be coupled together due to rotor hub design. These couplings must also be considered because they play a significant role in the handling qualities and aeroelastic stability of the helicopter.

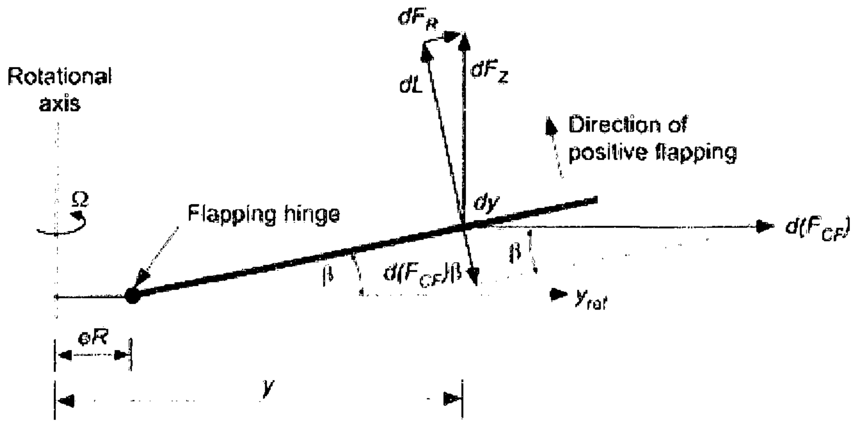

Figure 1.2: Forces acting on a blade about the flap hinge.

Modern blade designs take advantage of advanced materials (e.g. composites) to reduce the weight of blades. Hingeless rotors do not use flap and lead-lag hinges, but use a blade flexure to accommodate these blade motions. Hingeless rotors are mechanically simpler and cleaner aerodynamically than their articulated blade counterparts, but they are also much more difficult to design because of the complexity of their aeroelastic properties. Bearingless rotors (not shown) introduce even more structural complexity by replacing the pitch bearing, in addition to the flap and lead-lag hinges.

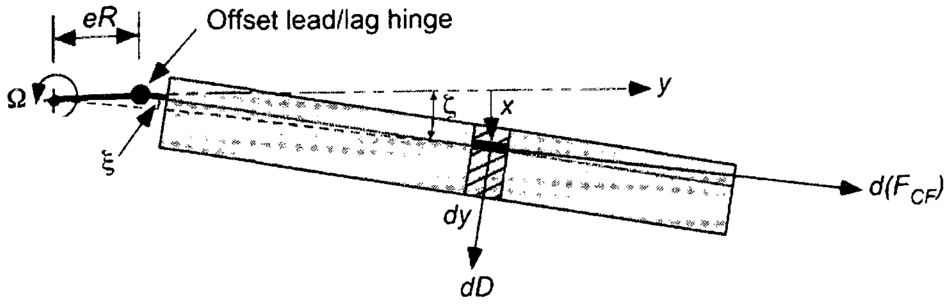

Figure 1.3: Design of modern rotors requires detailed structural dynamics (i.e. finite-element based) analysis to minimize aeromechanical instabilities and fatigue stresses.

1.3 TIP VORTICES AND ROTOR WAKES

During the past two decades, considerable research has been conducted into the problem of measuring the development of blade tip vortices trailed into the wakes of helicopter rotors. The structure of the tip vortices defines the induced velocity field at the rotor, as well as being largely responsible for a number of adverse problems. These problems include unsteady airloads and high noise levels associated with blade vortex interactions (BVI), and significant vibration levels associated with rotor wake/airframe interactions. The reduction of rotor noise has become an extremely important goal from both military and civil perspectives. The community acceptance (or tolerance) of helicopters will depend largely upon the successful reduction of the noise and vibration levels associated with helicopters. This, in part, requires a better understanding of the blade tip vortices and better predictions of the physics of problems such as BVI.

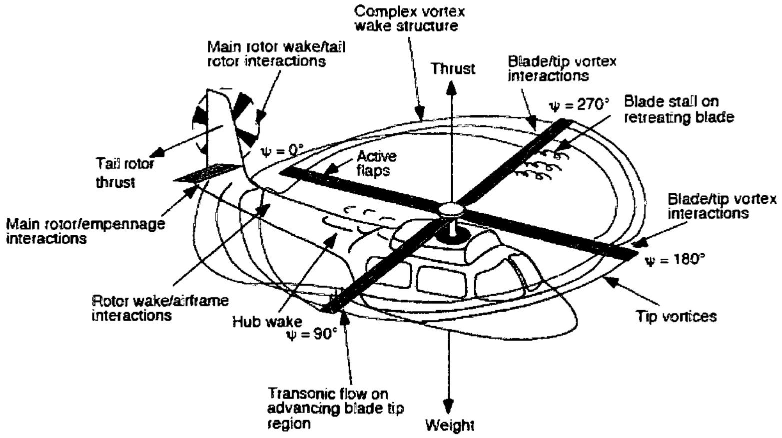

Figure 1.4: Typical flow phenomena found on a helicopter in forward flight.

Determining the characteristics of tip vortices accurately is fundamental to the case of the rotating-wing when compared with the fixed-wing. This argument can be justified using Figure 1.4, which shows representative aerodynamic phenomena found on a helicopter in forward flight. Notice the possible interactions between the tip vortices and various helicopter components. The spatial distance between the tip vortices and the blades, or between the vortices themselves, is considerably smaller, even in normal flight conditions such as hover or forward flight. As a result, a small change in the structure of the tip vortices and their positions relative to the rotor blades can have substantial effects on rotor airload and BVI noise. Furthermore, the rotor wake downwash on the fuselage, tail rotor and/or the empennage can lead to a further degradation in overall helicopter performance. This is not the case with fixed-wings, which trail rectilinear vortices that travel downstream away from the generating wing, and so have a decreasing influence on the wing as the vortices age.

Figure 1.5: A NASA study on wingtip vortices produced these pictures of smoke in the wake of an aircraft, clearly illustrating the size and power of the vortices produced.

Figure 1.6: Condensation in the cores of wingtip vortices from an F-15E as it disengages from a KC-10 Extender following midair refueling.

Most rotor wake measurements, if not all, fundamentally include the effects of stretching in the tip vortex behavior. The magnitude of this "stretching" depends on the flight conditions at which the measurements are made. Vortex filament stretching is often assumed negligible in most work and is not considered when explaining the physics of vortex flows, but its effects are combined to the vortices' net behavior. A schematic explaining the effects of positive filament strain is shown in Figure 1.6 as the vortex convects in the non-uniform flow. While viscous diffusion results in an increased core size and a decreased peak swirl velocity, as shown in Figure. 1.7, positive filament stretching results in a reduced core size and a concentration of vorticity. Conversely, a contraction results in an increased core size. Isolating vortex filament strain from viscous diffusion is, therefore, essential for developing better vortex models for helicopter rotor analyses (Lorber et al.,2000).

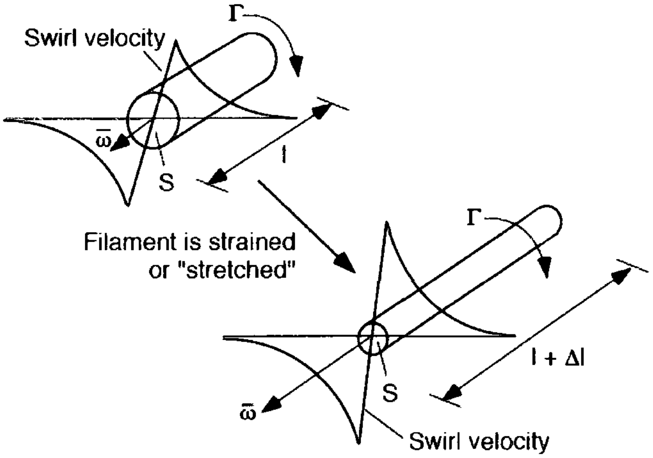

Figure 1.7: Schematic illustrating the effects of the positive straining or "stretching" of a vortex filament when subjected to a velocity gradient.

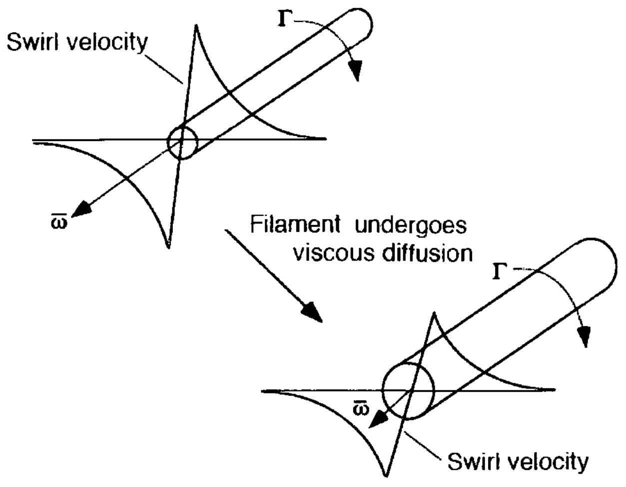

Figure 1.8: Effects of viscous diffusion of a tip vortex filament.

The structure of tip vortices is usually modeled by making a completely laminar or turbulent flow assumption. However, flow rotation has been hypothesized to play a substantial role in determining the overall turbulence structure inside a vortex and, on the evolution of the tip vortices, in general. Although there are measurements that have suggested a multi-region vortex structure (i.e., laminar flow inside the vortex core, followed by a transition region and an outer turbulent flow region), there have been no general vortex models derived from the N–S equations that take into account the effects of flow rotation in determining the turbulent structure and other characteristics of the tip vortices. In this regard, both Reynolds number and Richardson number effects must be considered. Besides filament stretching effects and flow rotation (Richardson number), another important but neglected issue is scaling effects (Lorber et al., 2000). The difficulty in developing an analytical model from the non-linear N–S equations, combined with the unavailability of computer resources to obtain a higher resolution numerical solution, has led to the development of semi-empirical models for the tip vortices trailing from helicopter rotor blades. The empirical constants that are used in these models are mostly estimated from sub-scale rotor or fixed-wing measurements.

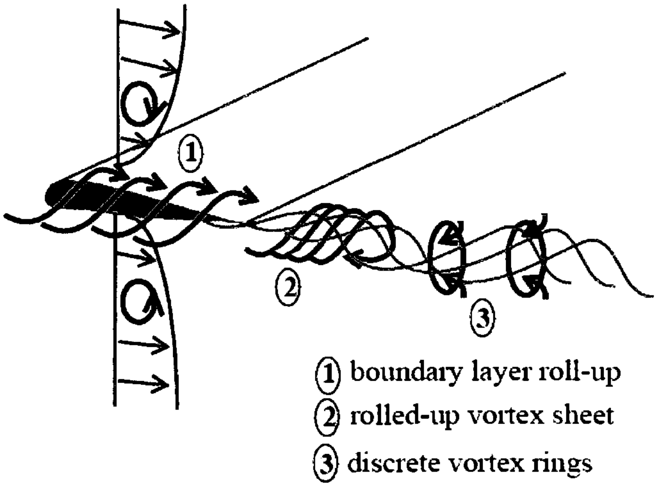

Figure 1.9: Proposed theory for the generation of a core axial velocity.

The ability to confidently predict the behavior of full-scale flight tests using the vortex models that are developed from sub-scale rotor measurements has not been justified. The vortex Reynolds number, which is defined as the ratio of total circulation to the viscosity (v), for sub-scale rotor models, is smaller by orders of magnitude when compared with full-scale flight vehicles. Even though the vortex Reynolds number is known to affect various properties of the tip vortices, existing vortex models used in helicopter applications do not address such scaling issues. The only exception is Iversen's vortex model, which is a function of vortex Reynolds number, but it assumes a fully turbulent vortex.

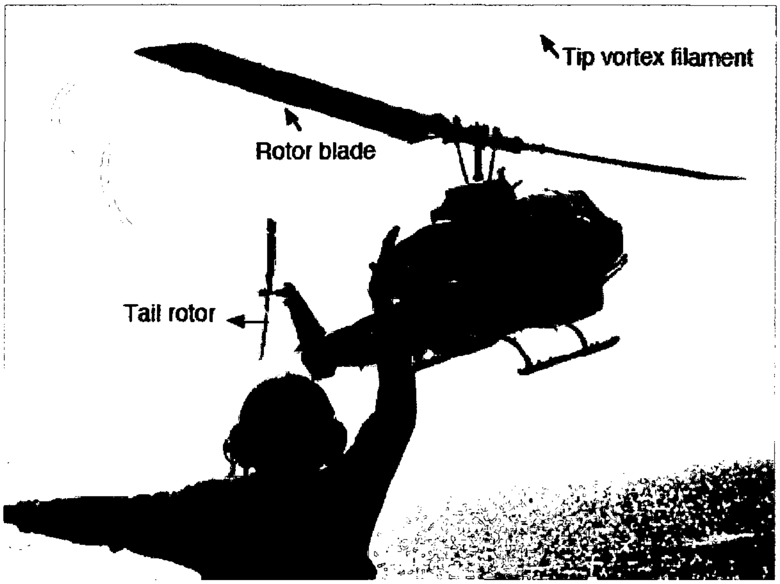

Figure 1.10: Tip vortices trailing the rotor blades of Bell AH-1 Cobra.

1.3.1 AIRPLANE WAKES

The presence of the strong tip vortex near the wing surface causes a significant downwash, reducing the effective angle of attack. This results in an induced drag on the wing. For a typical transport aircraft, induced drag contributes to around 35% of the total drag (Green, 1995). Further, the high energy contained in the tip vortices ultimately comes from the engine power. In typical airplane wakes, tip vortices primarily decay as a result of sinusoidal instabilities that are mutually excited by the pair of counter-rotating vortices from either wings. However, it takes hundreds of span lengths for these instabilities to take effect (Conlisk, 2001) and as a result, the tip vortices remain sufficiently strong for an undesirable amount of time. This proves to be a severe hazard to other aircraft as can be seen from Fig. 1.5. The strong tip vortices can induce severe rolling moments or even cause structural damages to following aircraft. The Federal Aviation Administration (FAA) recommends a separation distance of at least 5 miles between airplanes (Conlisk, 2001). This can restrict the capacity of airports and air-traffic in general.

1.3.2 HELICOPTER WAKE SYSTEM

Unlike an airplane wing, helicopter blades constantly operate in the wake trailed from the preceding blades. The interaction of the wake with the blade (this phenomenon is commonly known as Blade Vortex Interaction or BVI (Sim et al., 2000)) has profound effects on the aerodynamics and structural dynamics of the rotor system. The situation is exacerbated by the fact that these interactions can occur before the vortex has undergone any significant decay. The velocities induced by the unsteady wake results in impulsive changes in the flow encountered by the rotor blades, and can cause high noise and vibration levels.

In flight conditions like hover, climb/descent and low-speed forward flight, multiple turns of the wake remain under the rotor at all times and the resulting induced inflow has a significant effect on the performance. In addition to the effects on the main rotor, the trailed wake can interact with the fuselage, tail rotor etc. The complexity engendered by the returning wake makes the design prediction of helicopter performance very difficult.

The above discussions highlight the importance and need to understand the physics of airplane and helicopter wakes. Also, in both cases, it is apparent that reducing the strength of tip vortices without a significant loss of performance can prove to be very beneficial. Although the study of tip vortex flow fields has been an extremely active area of research over the past century in the form of analytical, experimental and computational studies, comprehensive understanding of the intricate details of vortex formation and evolution is more qualitative than quantitative. The broad objective of this thesis is to develop a high fidelity numerical methodology that can elucidate the process of vortex formation, roll-up and evolution. This is supplemented with theoretical studies and further numerical simulations of vortex control strategies.

(a) Baseline configuration – rotor operates in free-air

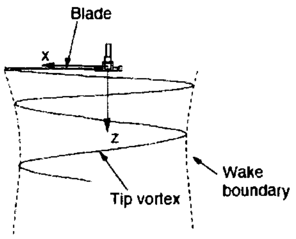

(b) Rotor operates next to ground plane

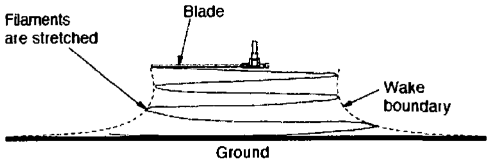

Figure 1.11: Wake structure of a helicopter rotor. (a) Baseline case: rotor operates in free air. (b) Ground effect: Rotor operates in the presence of ground, which stretches the vortex filaments.

1.3.3 CHALLENGES IN MODELING THE TIP VORTICES

An exact solution to the three-dimensional Navier–Stokes (N–S) equations is required to completely describe a viscous trailing vortex. Because an exact solution to these non-linear sets of equations is not possible, most of the vortex models that exist today have been derived by making sweeping assumptions and approximations that lead to simplified solutions to the N–S equations. These assumptions include incompressible, one-dimensional flow and completely laminar or turbulent flow inside the tip vortices. Even though these assumptions result in solutions that can be applied in various applications, the vortex models that are developed based on these assumptions have been found to be inadequate to explain many essential properties of tip vortices as is shown in experiments. For example, the most frequently made one-dimensional assumption eliminates the effects of the three-dimensional induced velocity field on the development of tip vortices. This can be viewed as either a stretching or contraction of the filament, and as previously mentioned can change the induced velocity field. The effects of vortex filament stretching on the growth properties of the tip vortices were found to be substantial, as discussed earlier. From a modeling perspective (development and validation), this is a concern because of the need to isolate stretching effects from the effects of viscous/turbulent diffusion.

1.3.4 BVI-GENERATED NOISE AND VIBRATION

BVI noise is a result of the interaction of a rotating blade with the tip vortex emanating from the previous blade (see Figure 1.13). The interaction of the tip vortex changes the angle of attack on the blade locally and can result in large temporal airloads and an intense acoustic pulse (Ringler et al., 1991; Leishman, 1996; Lim and Tung, 1997). The severity of the noise level depends upon the location of the interaction on the rotor disk, the miss distance between the blade and the vortex, and the vortex properties themselves (swirl velocity, core size etc.) (Boisard and Baeder, 2001). The blades may also interact with vortex filaments that are relatively old in terms of rotor revolutions. During this time, the vortex filaments will have undergone some amount of viscous and turbulent diffusion, as well as encountering steep velocity gradients that can also affect their evolution (Ananthan et al., 2002; Ramasamy and Leishman, 2003). This further complicates the aerodynamic environment at the plane of the rotor, and so results in highly unsteady airloads that are extremely difficult to predict.

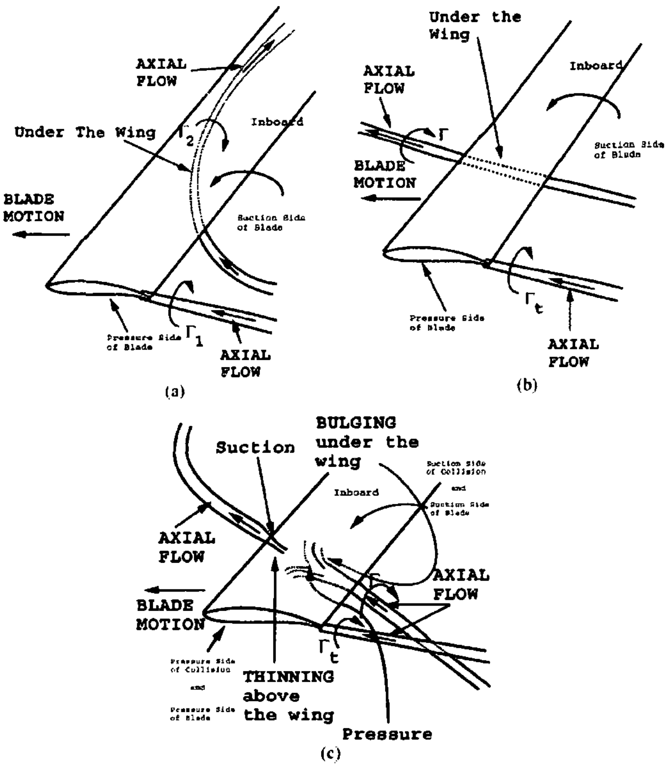

Figure 1.12: Most common BVI events: (a) almost parallel interactions; (b) almost perpendicular interactions; and (c) oblique collision.

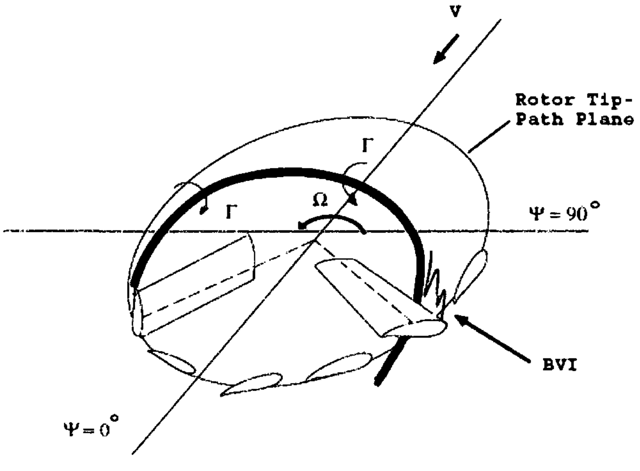

Figure 1.13: Direct collision between a blade and a vortex.

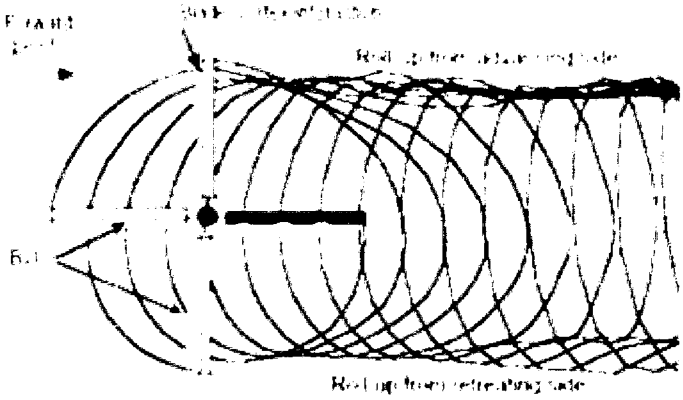

Figure 1.14: Locations of BVI on a four-bladed rotor operating in forward flight.

Figure 1.15: Experimental vs. Computational BVI M=0.5.

Rotor vibration is another adverse characteristic of the helicopter that has its source in the unsteady aerodynamics of the main rotor. Tip vortices from several revolutions (or blades) can form a bundle and can manifest as a single merged vortex that has strength much larger than an individual vortex filament. This results in an extensive localized region of downwash altering the angle of attack on the rotor blades. Consequently, this reduces the lift produced near the tip at a frequency of N_b/rev. These unsteady airloads are transmitted through the hub as vertical airframe vibration. These excessive vibrations contribute greatly to aircrew and passenger discomfort and fatigue, and affect the maintainability, reliability, and operability of the helicopter.

Any strategy aimed at alleviating or controlling these vortex induced adverse phenomena must stem from a better understanding of the structure, strength and various characteristics of the tip vortices emanating from the tip of the rotor blades. This, in turn, should help in developing and validating tip vortex models with higher levels of fidelity to ensure sufficient confidence in the induced airloads predictions, vibrations and noise levels associated with helicopter rotors (Rahier and Delrieux, 1997).

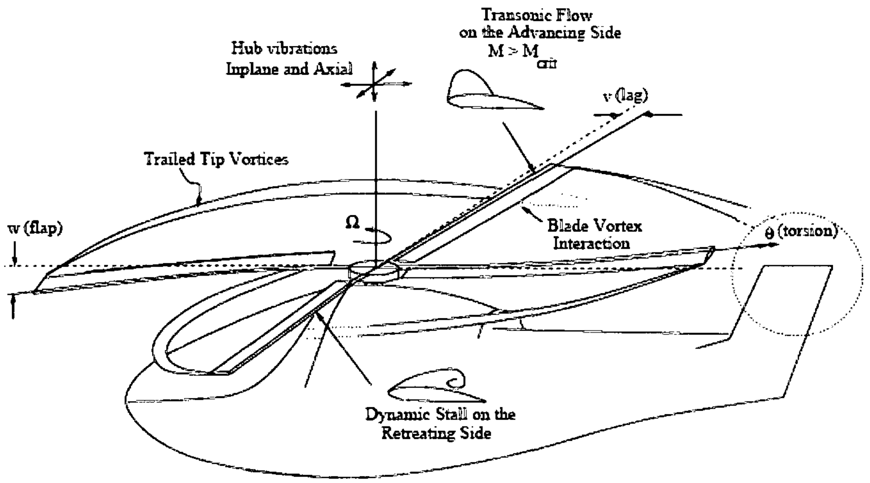

Figure 1.16: Sources of rotor vibration.

1.4 UNDERSTANDING THE FLOW PHYSICS

The physics of the flow is extremely complex in the near-field region since the process is largely turbulent (under flight conditions, the chord based Reynolds numbers for typical airplanes and helicopters can be expected to be in the range of 10^6-10^7 (Leishman, 1998)), highly three-dimensional and involves high-flow gradient regions involving multiple flow separations (Chow et al., 1997). As mentioned earlier, the pressure difference accelerates the flow from the lower surface around the wing tip. This, combined with the free-stream flow, results in the formation of the tip vortex as shown in Figure 1.18. But this is an inviscid description and masks the àctual near- field physics. In practice, the viscous nature of the flow introduces additional effects as shown in Figure 1.15. The cross flow streamlines (Figure 1.17) show transport of fluid particles from the lower surface to the upper surface. As seen from Figure 1.18, the associated boundary layer tends to separate once the pressure gradient weakens on the top surface. In addition, a weaker secondary vortex of opposite sense (to the tip vortex) is formed. These structures continue to evolve on the upper surface of the wing and are ultimately convected downstream of the trailing edge. As observed by Devenport et al. (1996), the primary and secondary vortices orbit around each other and ultimately merge into one coherent vortex. Part of the wake shed by the wing is also entrained into the tip vortex. The formation and structure of the wake system is very sensitive to loading conditions, surface geometry etc.

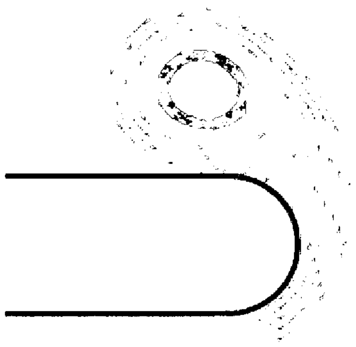

Figure 1.17: Cross-flow streamlines.

In the far field, the vortex is fully rolled-up and is found to be largely axisymmetric. Many studies on wing tip vortices have reported largely reduced turbulence levels in the vortical core even in the near-field. This has been attributed to the near-solid body rotation that exists in the inner core. Analytical studies, based on linear stability theory of isolated vortices (Jacquin and Pantano, 2002), have also supported this argument by showing the damping of imposed small disturbances in the core. The decay rate is primarily governed by the axial and tangential velocities that exist in the vortical core (Qin, 1998; Ragab and Sreedhar, 1995) and in cases with small axial velocities (in relation to the tangential velocities), the major diffusion mechanism seems to be laminar rather than turbulent.

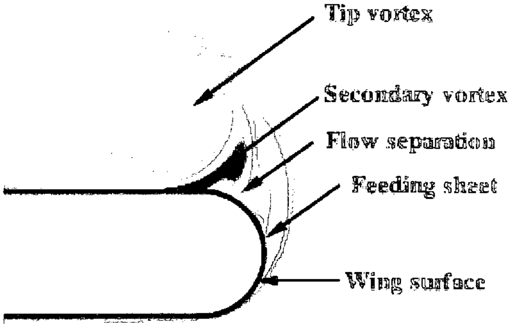

Figure 1.18: Vortex formation along span wise section of a simple fixed wing

In the case of rotary wing tip vortices, different turns of the wake interact with each other (Leishman, 1998) and could possibly merge together, a process that could change the turbulence structure drastically (Leweke, 2001). The magnitude of noise and vibration on a helicopter rotor is very sensitive to the core structure of the vortex and also to the distance and attitude of different turns of the wake with respect to the blades (Sim, 2000). Under some flight conditions, the core of the returning tip vortex could be so close to the blade that it can mutually exchange vorticity with the blade boundary layer.

1.5 ROTOR CONFIGURATIONS

Conventional (single rotor) helicopters are what most of us think of when we hear the word. The configuration consists of a large main rotor rotating in a nominally horizontal plane and a smaller tail rotor rotating in a nominally vertical plane parallel to the aircraft axis to provide anti-torque. Many helicopters have the main rotor canted forward (after all, the vehicle is manufactured to primarily accommodate forward flight) a bit, and sometimes to the side to accommodate subtleties of rotor dynamics.

Figure 1.19: Ah-64 A/D Apache Attack Helicopter.

Tandem rotor (sometimes referred to as dual rotor) helicopters have two large horizontal rotor assemblies a twin rotor system, instead of one main assembly, and a smaller tail rotor.

Single rotor helicopters need a tail rotor to neutralize the twisting momentum produced by the single large rotor. Tandem rotor helicopters, however, use counter-rotating rotors, with each canceling out the other's torque. Counter-rotating rotor blades will not collide with and destroy each other if they flex into the other rotor's pathway. This configuration also has the advantage of being able to hold more weight with shorter blades, since there are two sets. Also, all of the power from the engines can be used for lift, whereas a single rotor helicopter uses power to counter the torque. Because of this, tandem choppers are among some of the most powerful and fastest. The CH-47 Chinook for example, has one of the fastest top speeds of any helicopter in service.

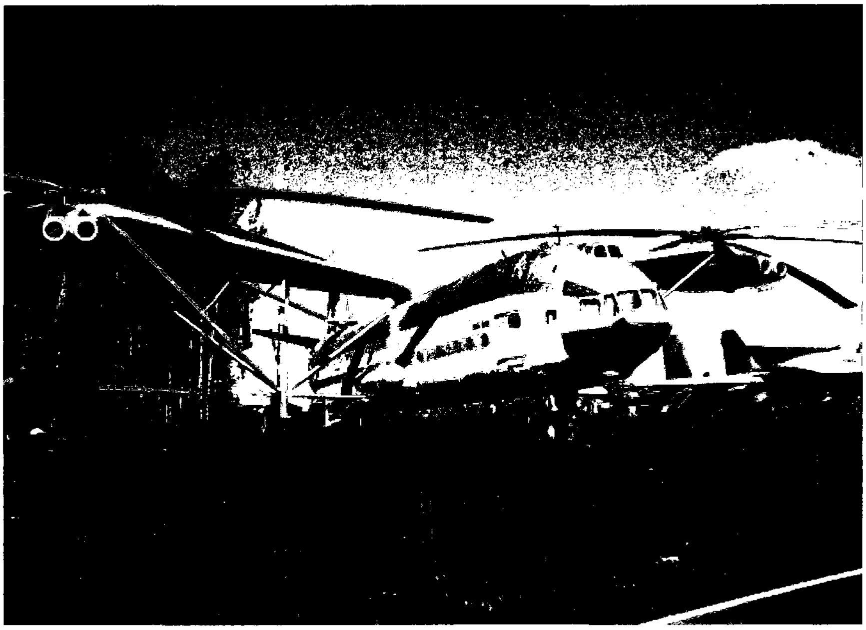

Figure 1.20: Mil V-12, largest helicopter in the world.

Figure 1.21: Tandem rotor design of the MH-47E Chinook.

Each rotor in a coaxial configuration turns in the opposite direction of the other rotor, and they are mounted on a single mast, with the same axis of rotation, one above the other. The coaxial configuration helicopter is so special due to the fact that it embodies a principle of the reactive moment compensation fundamentally different from that of the single-rotor configuration. To compensate for the reactive moment of the single-rotor helicopter's main rotor, the tail rotor's side force is applied to the airframe, while the coaxial-rotor helicopter has its rotors' reactive moments compensating each other directly in their axis of rotation. This removes the need for any additional forces. Rotors' reactive moments are compensated automatically throughout the flight, thus requiring no interference on the part of the pilot.

Figure 1.22: An example of a coaxial rotor: Russian Kamov-50 Alligator.

One of the problems with any single set of rotor blades is the tendency of the helicopter body, once airborne, is to begin spinning in the opposite sense to that of the rotors. This is described by the principle of conservation of angular momentum: initially, the helicopter possesses zero total angular momentum (i.e., is not spinning about the rotor axis). The engines of the helicopter, by turning the rotor blades, input a sizeable amount of angular momentum into the rotor blades. Since the helicopter as a system (treating the rotor blades and the body as two components of that system) remains near zero total angular momentum, the body begins to pivot about the rotor axis in the opposite direction to the rotors. In other words the torque exerted by the engine, as well as turning the blades as intended, also turns the helicopter body in relation to the rotor.

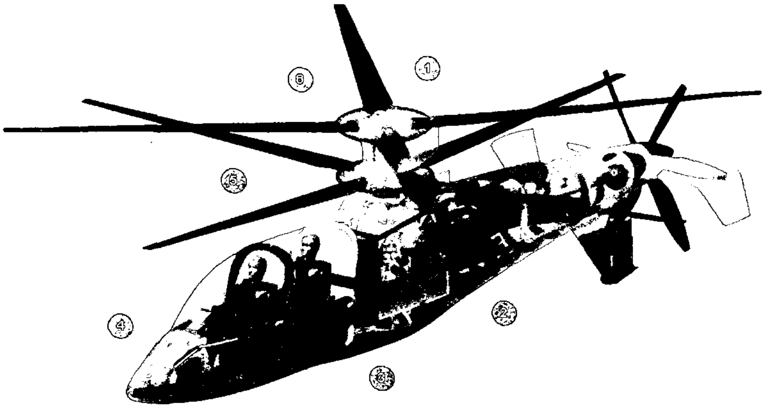

Figure 1.23: Sikorsky X2 Technology™ Demonstrator.

This phenomenon is catastrophic from the pilot's point of view, who wishes to maintain a stable flight. To counteract the effect, the tail rotor was introduced to provide a constant input of angular momentum to the body *in the opposite direction to that from the engine*. Since angular momentum is a directional quantity, the two components of the helicopter system, while possessing equal *magnitudes* of angular momentum, possess it in opposite *directions*, which cancel each other out. Thus, the condition of zero total angular momentum is maintained, but the helicopter's fuselage remains stationary and stable level flight becomes possible. Varying the torque exerted by the tail rotor upon the helicopter's tail boom (which controls the magnitude of the angular momentum input) facilitates controlled turning, and contributes to the helicopter's extreme maneuverability, due to the fact that in the hover condition (no lateral movement relative to the ground) the helicopter can be pivoted about the rotor axis independently of other flight controls. Control of rotational motion with the other two designs is achieved by the simple expedient of ensuring that the two sets of rotor blades rotate in opposite directions, cancelling each other out in terms of angular momentum. Rotational maneuvering is a more complex topic with respect to these designs, however, and involves engineering features that are beyond the scope of this article. Coaxial rotors solve the problem of angular momentum by turning each set of rotors in opposite directions, allowing the fuselage to maintain zero angular momentum until the pilot varies the angular momentum inputs in a controlled fashion to facilitate turning.

Once a single-rotor helicopter is in forward flight, a second phenomenon manifests itself, called “dissymmetry of lift” which possesses the potential to disrupt stable flight at speed. Dissymmetry of lift imposes an upper speed limit (known as the Never-Exceed Speed or VNE) upon single-rotor helicopters, by virtue of the fact that during one rotation of the rotor disc, a rotor blade experiences, in extreme parts of the flight envelope, two widely contrasting unstable conditions. On one side (the advancing side) of the rotor disc, rotor blades travel through the air sufficiently quickly for the airflow over them to become transonic or even supersonic, which causes fundamental changes in the airflow over the rotor blades; while on the other (retreating) side of the rotor disc, the rotors travel through the air much more slowly, possibly slowly enough to enter the stall condition, thus failing to produce lift. Both aerodynamic régimes result in (frequently catastrophic) flight instability. Coaxial rotors solve the problem of dissymmetry of lift because one set of rotors is cancelled by the corresponding increased lift on the same side of the other set of rotors, and vice versa, resulting in a helicopter that can fly, theoretically at least, faster than a single-rotor design, and more stably in extreme parts of the flight envelope.

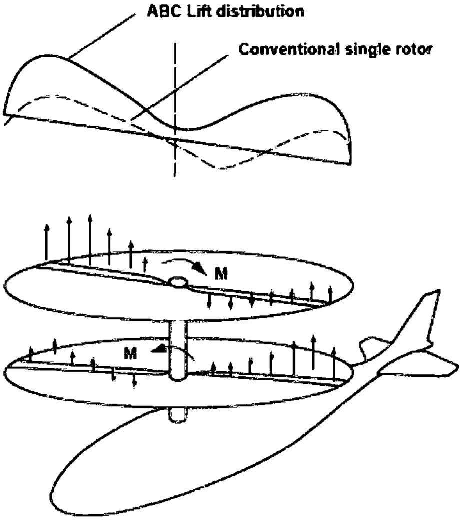

Figure 1.24: A schematic of the Advancing Blade Concept.

One other benefit arising from a coaxial design include increased payload for the same engine power - a tail rotor typically wastes some of the power that would otherwise be devoted to lift and thrust, whereas with a coaxial rotor design, all of the available engine power is devoted to lift and thrust. Reduced noise is a second advantage of the configuration-part of the loud 'slapping' noise associated with conventional helicopters arises from interaction between the airflows from the main and tail rotors, which in the case of some designs can be severe (the UH-1 Iroquois or 'Huey' is a particularly loud example).

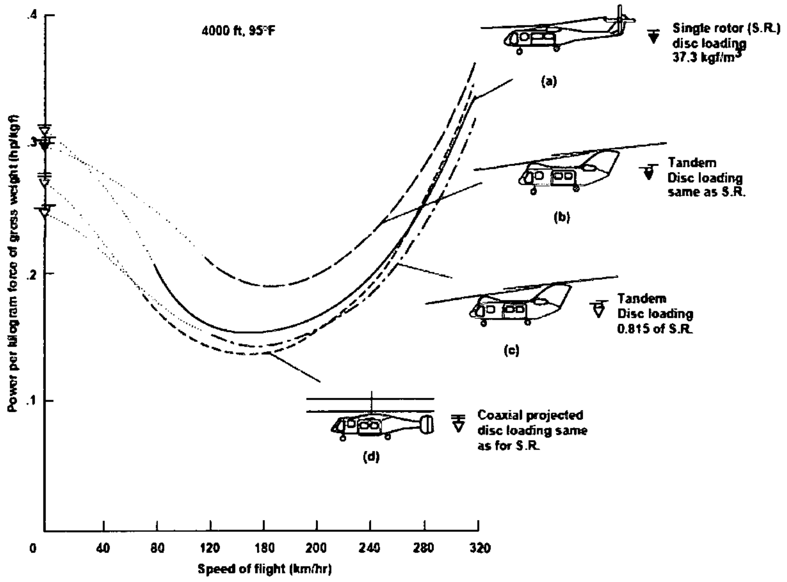

Figure 1.25: Performance comparison of different helicopter types (Stepniewski and Burrowbridge, 1986)

Also, helicopters using coaxial rotors tend to be more compact (occupying a smaller 'footprint' on the ground). Several Kamov designs are used in naval roles, being capable of operating from confined spaces on the decks of ships, including ships other than aircraft carriers (an example being the Kara Class cruisers of the Russian navy, which carry a Ka-25 'Hormone' helicopter as part of their standard fitment).

A principal disadvantage of the coaxial rotor design is the increased mechanical complexity of the rotor hub-linkages and swash plates for two rotor discs needed to be assembled around the rotor shaft, which itself is more complex because of the need to drive two rotor discs in opposite directions. In an elementary engineering sense, the coaxial rotor system is more prone to failure because of the greater number of moving parts and complexity, though the engineering tolerances in aerospace are usually sufficiently precise to mitigate this somewhat.

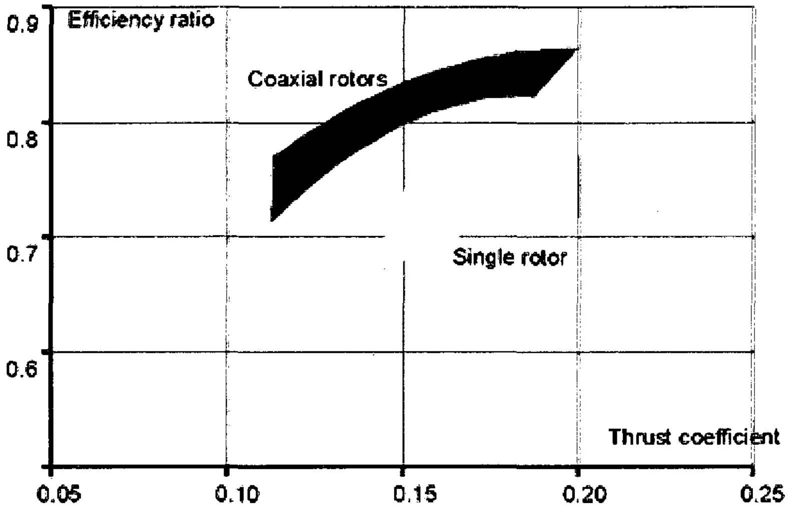

Figure 1.26: Comparison of aerodynamic quality in hover.

Additionally, while the resulting design· has the capacity to be even more maneuverable than a conventional helicopter, achieving this in practice requires some ingenuity. As an example, the Kamov Ka-50 Werewolf (NATO reporting name 'Hokum') took a long time for Kamov to develop from prototype to operational status (though part of this long development time was because of additional complexities, such as the unique K-37-800 ejector seat mechanism on the Werewolf).

1.6 FULLY ARTICULATED ROTORS

Fully articulated rotor systems allow each blade to feather (rotate about the pitch axis to change lift), lead and lag (move back and forth in-plane), and flap (move up and down about an inboard mounted hinge) independent of the other blades. As will be discussed, each of these blade motions is related to each other. Fully articulated rotor systems are found on rotor systems with more than two blades.

As the rotor spins, each blade responds to inputs from the control system to enable aircraft control. The center of lift on the whole rotor system moves in response to these inputs to effect pitch, roll, and upward motion. The magnitude of this lift force is based on the collective input, which changes pitch on all blades in the same direction at the same time. The location of this lift force is based on the pitch and roll inputs from the pilot. Therefore, the feathering angle of each blade (proportional to its own lifting force) changes as it rotates with the rotor, hence the name cyclic control. As the lift on a given blade increases, it will want to flap upwards. The flapping hinge for the blade permits this motion, and is balanced by the centrifugal force of the blade's weight, which tries to keep it in the horizontal plane. Either way, some motion must be accommodated. The centrifugal force is nominally constant, however, the flapping force will be affected by the severity of the maneuver (rate of climb, forward speed, aircraft gross weight).

As the blade flaps, its center of gravity changes. This changes the local moment of blade's inertia with respect to the rotor system and it either speeds up or slows down with respect to the rest of the blades and the whole rotor system. This is accommodated by the lead-lag hinge, and is easier to visualize with the classical ice skater doing a spin image. As the skater moves her arms in, she spins faster because her inertia changes, but her total energy remains constant (neglect friction for purposes of explanation). Conversely, as her arms extend, her spin slows. Lead-lag motion is typically moderated by an in-plane damper. So, following a single blade through a single rotation beginning at some neutral position, as load increases from increased feathering, it flaps up and leads forward. As it continues around, it flaps down and lags backward. At the lowest point of load, it is at its lowest flap angle and also at its most rearward lag position.

Because the rotor is a large, rotating mass, it behaves somewhat like a gyroscope. The effect of this is that a control input is realized on the attached body at a position 90 degrees behind the control input. This is accounted for by the designers so that a forward input of the cyclic control stick results in a nominally forward motion of the aircraft. The effect is transparent to the pilot. There are a few other considerations to the placement of control inputs also transparent to the pilot, but still interesting to discuss. Location of the input links to the rotor blades is related to the phasing of the rotating and stationary controls and also to the amount of blade input rotation required. Because the lead-lag hinge and the flapping hinge are not necessarily coincident, at the location of the input may be located such that as the blade flaps or lead-lags, there may be a change in blade pitch input as flapping or lead-lag occurs (or both). This is a little difficult to visualize, but imagine that the input link is located at the same distance from the center of the rotor hub as the flapping hinge. As the blade flaps, there is no effect on pitch. If the input link is inboard or outboard of the hinge, some coupling (or change in blade angle) results. If an increase in blade angle results because of an increase to blade pitch, the situation compounds. This situation is nominally unstable, but depending on the rotor system, is not necessarily bad. This can similarly occur in lead-lag.

Older hinge designs relied on conventional metal bearings. By basic geometry, this precludes a coincident at flapping and lead-lag hinge and is cause for recurring maintenance. Newer rotor systems use elastomeric bearings, arrangements of rubber and steel that can permit motion in two axes. Besides solving some of the above-mentioned kinematic issues, these bearings are usually in compression, can be readily inspected, and eliminate the maintenance associated with metallic bearings.

1.7 SEMI-RIGID (TEETERING) ROTORS

Semi-rigid rotors are found on aircraft with two rotor blades, such as Robinson, Hiller, and many Bell products. The blades are connected such that as one blade flaps up, the opposite blade flaps down. This is accommodated by allowing the rotor system to teeter at the top of the rotor mast. The Robinson system, although basically teetering, permits some independent flapping of each blade and operates in a similar fashion.

Because the rotors are tied together rigidly in-plane, there is no lead-lag The Hiller design uses the large main blades for lifting, but relies on two smaller blades that are 90 degrees to these for cyclic control between them. The rotor does not necessarily cone but rather tilts up on the side with more lift and tilts down on the other. Flapping is therefore self-balancing. Issues of phasing, gyroscopic precession, and flap coupling are still present, but easier for the designer to manipulate.

1.8 RIGID ROTORS

Rigid rotors want to behave similarly to fully articulated rotors, but do not provide flapping or lead-lag hinges. Instead, the blades accommodate these motions by bending. Because the kinematic loads are not resolved by actual blade motion, high vibration may result. Rigid rotor systems are rare, but may become more common as improvements in material properties and vibration control evolve. They are fundamentally easier to design and potentially offer the best of both teetering and fully articulated systems.

CHAPTER II

BACKGROUND AND LITERATURE REVIEW

This chapter is divided into two parts. The first part discusses the past efforts for helicopter simulations. In the second part, experimental and numerical studies of coaxial rotor configurations are briefly reviewed.

2.1 HELICOPTER SIMULATIONS

An accurate computation of helicopter rotor flows in both hover and forward flights continues to be a complex and challenging problem. Reliable prediction of helicopter performance is heavily dependent on the accurate prediction of the transonic flows on the advancing side of a helicopter rotor and proper resolution of blade–vortex and blade–wake interactions. To account for the former, a robust, fully compressible CFD solver is essential in computing the flow around rotor blades. Most compressible flow solvers, regardless of the numerical algorithms, introduce a certain amount of numerical dissipation, which can be intrinsic to the discretization or explicitly added to avoid numerical instability. In either case, the amount of dissipation is proportional to the mesh size. This is a crucial issue because it may lead to erroneous dissipation of the wake or tip vortices and their subsequent spreading. It is clear that there is a need for a method that captures the vortical structures in order to properly resolve a helicopter wake.

Helicopter simulation remains the subject of ongoing research after many decades. An attempt to entirely simulate the main rotor system of a helicopter requires a multidisciplinary approach, involving coupling of the flow and structure models. In addition, either multi-block structured meshes or unstructured meshes are needed, and massive parallelization is a must for solving a problem related to helicopter including the fuselage and tail rotor. Recent comprehensive surveys of the current status of helicopter aerodynamics including both the theoretical and experimental work can be found in Conlisk (1997) and Leishman (2006), while Friedmann (2004) extensively reviews issues regarding aeroelasticity of rotary-wing aircraft. Caradonna (2000) gives an extensive review on CFD on rotorcraft and discusses unsolved problems and prospects of solution philosophy for solving them. Johnson (1994) and Stepniewski and Keys (1984) also provide excellent background on helicopter and rotary-wing aircraft aerodynamics. The remainder of this section summarizes some of the CFD work that has been done in helicopter aerodynamics and relevant experimental work.

There are many approaches that researchers use in order to simulate problems involving helicopter or rotory-wing aerodynamics. Some of the early approaches focused on the vortex dynamics using momentum theory, blade element theory and actuator vortex theory. However, as the computer power and memory increased, researchers started to work on more complicated governing equations of the fluid starting from the transonic small disturbance equation, the full potential flow equation, the Euler equations, and finally the RANS equations. Solution to the true Navier–Stokes equations for helicopter simulations is still prohibitively expensive. There has been some work done using large eddy simulation (LES) to simulate parts of the geometry, mostly for the blade–vortex interaction, but it is still not computationally feasible to apply LES for the entire helicopter or even just a complete helicopter rotor.

2.1.1 POTENTIAL FLOW SIMULATION

One of the earliest investigations in the field of helicopter simulation was by Caradonna and Isom (1972), who used a compressible potential flow solver to simulate non-lifting hovering helicopter blades. Analytical and numerical results of linearized subsonic three-dimensional flow in the tip region were presented. Caradonna and Isom (1976) made further progress by using the small disturbance potential flow equation with the Murman–Cole (Murman and Cole, 1970) mixed type difference techniques to simulate forward flight of a non-lifting rotor blade. Later, combined experimental and simulations using the potential flow equations were carried out by Caradonna and Philippe (1978) in order to investigate transonic flow on an advancing rotor. The computational model was the two-dimensional transonic small disturbance equation for a non-lifting blade in forward flight. The test model was a modified Alouette II tail rotor with the profiles that were symmetric NACA 00XX (mostly NACA 0012) with a thickness ratio that decreased from root to tip. Three lifting cases were also considered in the paper with sinusoidal variation of the angle of attack. Chattot and Phillipe (1980) at ONERA also studied the pressure distribution on a non-lifting symmetrical helicopter blade in forward flight using the three-dimensional unsteady transonic small disturbance equation. Their numerical results were compared with experimental data, as well as with computational results by RAE and NASA.

The first three-dimensional, full potential flow calculation for the flow of a lifting helicopter blade was achieved by Arieli et al. (1985). The code was called ROT22, and was based on Jameson and Caughey's famous FLO22 (the code was an inviscid, non-conservative, three-dimensional full potential flow solver). The numerical results were compared with laser velocimeter measurements made in the tip region of a non-lifting rotor at a tip Mach number of 0.95 and zero advance ratio (i.e. no forward flight velocity component). In addition, comparisons were made with chordwise surface pressure measurements obtained in the wind tunnel for a non-lifting rotor blade at transonic tip speeds at advance ratios ranging from 0.40 to 0.50.

2.1.2 EULER AND RANS SIMULATIONS

Agarwal and Deese (1987) calculated aerodynamic loads on a multi-bladed helicopter rotor in hovering flight by solving the three-dimensional Euler equations in a rotating coordinate system on body-conforming curvilinear grids around the blades. The Euler equations were recast in the absolute flow variables so that the relative flow is uniform. Equations were solved by finite volume explicit Runge–Kutta time stepping scheme based on the work of Jameson et al. (1981). Rotor–wake effects were modeled by computing the local induced downwash with a free wake analysis method. The far-field boundary condition was solved with one-dimensional Riemann invariant normal to the boundary. As a result, the pressure coefficient on the surface was quite accurately predicted near the tip, but was over-predicted as the distance moved closer towards the hub as compared to the experimental results by Caradonna and Tung (1981). Agarwal and Deese (1988) extended the same computation further by solving the compressible RANS equations. However, the boundary condition for the far field used in this work was still the one-dimensional Riemann invariant type, and the pressure coefficient on the surface was again under-predicted near the tip and over-predicted towards the middle of the blade.

Chen et al. (1990) used a finite volume upwind algorithm based on Roe flux splitting and the implicit time operator was solved by the lower upper symmetric Gauss–Seidel (LU–SGS) based on Jameson and Yoon (1987) to solve the three-dimensional Euler equations with a moving grid.

Srinivasan et al. (1990) performed simulations of a lifting rotor in hover based on the thin-layer Navier–Stokes equations. Their calculation used an implicit upwind finite difference method for space discretization. The monotone upstream-centered schemes for conservation laws (van Leer, 1979; Anderson et al., 1984), most commonly known as the MUSCL scheme, was used to obtain the second or third order accurate fluxes with limiters in order to satisfy the total variation diminishing (TVD) property. The surface pressure calculation showed good agreement with the experimental data of Caradonna and Tung, but the wake structure diffused quickly due to the coarse grids. The authors claimed that this had minimal effects on the predicted surface pressure. Limited comparison with results calculated by the Euler equations were presented.

Srinivasan et al. (1991) studied the planform effects on the airloads using the three-dimensional thin-layer Navier–Stokes equations on lifting hover configurations based on UH–60 and BERP rotors. The numerical finite difference implicit numerical scheme for this work was described in the experiment of Srinivasan et al. (1990). The numerical algorithm used the Roe upwind-biased scheme for all three coordinates with reconstruction by higher order MUSCL schemes in order to model both shocks and propagating acoustic waves. The LU–SGS implicit operator was used to obtain the solution of both the unsteady and convective terms. The hover case was solved in the blade-fixed coordinate system.

Srinivasan and McCroskey (1993) later performed Euler calculations of unsteady interaction of advancing rotor with a line vortex. A prescribed vortex method was chosen to preserve the structure of the interacting vortex. The calculated results were compared to the two-bladed model helicopter rotor experiment by Caradonna and Tung and consisted of parallel and oblique shock interaction. Their results showed that subsonic parallel blade–vortex interaction was almost two-dimensional. However in the transonic regime, the three-dimensional effects were found to be prominent. The governing Euler equations were solved using a two-factor implicit, finite difference numerical scheme (Ying et al., 1986).

A free wake Euler and Navier–Stokes calculation by Srinivasan and Baeder (1992) included the study of blade–vortex interaction (BVI) and high-speed impulsive (HSI) noise. The BVI noise is caused by the interaction of the vortical wake with the rotating blades and is more difficult to model because of the three-dimensional wake effects. HIS on the other hand, is caused by the compressibility effects. The numerical schemes were identical to those used in the paper by Srinivasan et al. (1990). Boniface, J. C. and Sid`es, J. (1993) performed a numerical study of steady and unsteady Euler flows around multi-bladed helicopter rotors both for hover and forward flight cases. For the hover case, a source term was added and the Euler equations were solved as a steady problem. A finite volume, space-centered flux discretization that did not require artificial viscosity were used. For the time marching scheme, the authors used a modified Lax–Wendroff approximation with one predictor in each space and a corrector. However, for the forward flight simulations, an artificial viscosity needed to be added to the equations. The hover simulations were compared with the Caradonna and Tung experiment, and also data for four-bladed rotor of IMF of Marseille. Two forward flight cases were simulated corresponding to the Caradonna et al. (1984) experiment and a three-bladed ONERA model rotor with cyclic pitching.

Sheffer et al. (1997) performed simulations of helicopter rotor flows including aeroelastic effects for both hover and forward flight using BDF for the time integration and with the JST and CUSP artificial dissipation schemes (Jameson et al.,1981; Jameson, 1995b). Their Euler and RANS results were in good agreements with the Caradonna and Tung model helicopter hover experiment. For the forward flight, the Euler calculation, coupled with a structural model, 36 time steps per revolution with 50 multi grid cycles for each time step were used. After 6 revolutions, the simulation nearly reached periodic state. This simulation took 9 hours with 30 processors on IBM SP-2 machines. The total number of mesh size was 860,160 cells with 90 blocks.

Boelens et al. (2000) from the NLR performed computations for a helicopter rotor in hover, focusing their results on vortex capturing since complete vortex wake prediction for a helicopter in hover is an important requirement for predicting the rotor performance in the hover flight regime. The compressible Euler equations expressed in an Arbitrary Lagrangian-Eulerian (ALE) reference frame were used in this work. The space discretization was a second order Galerkin finite element method on hexahedral mesh. The capture of vortices was achieved by local mesh refinement in regions where they were expected to form. The results were benchmarked with experimental results from Caradonna and Tung. The multi-block grid was specially generated given a grid uniform distribution to account for the blade's tip vortex downward and inward. Even for a simple hover case with only one section of the blade, rather than the full two-bladed rotor, 55 blocks were used with the total of 726,784 elements and 823,599 mesh points. The C_p prediction of the lower surface was good but the Cp prediction of the upper surface was not that accurate as it over-predicted the pressure peak compared to the experimental data.

Pomin and Wagner (2001, 2002) performed Euler/RANS hybrid computations for the hovering 7A model rotor and a low aspect ratio NACA 0012 profile in non-lifting forward flight using both periodic and overset grids. The periodic grid was a mono-block C–H type and the computation was limited to hover cases only. The overset grid approach was used for all the helicopter flight spectrum. The C–H grids surrounding the blades were embedded into the background grid. RANS calculations were performed only in the inner regions and the Euler solver was used in the background mesh. For hover calculations, aeroelastic effects were taken into consideration via the coupling of the flow solver and a finite element model of the blade based on Timoshenko beam theory. An implicit finite volume scheme was applied for the numerical solution of the governing equation using a backward difference time discretization. The unsteady computations were second order accurate in time, and first order accurate for the hover analysis on periodic grids. The implicit system of equations was solved iteratively by a Newton method combined with LU–SGS. The hover boundary condition was based on the one-dimensional momentum theory and was applied in conjunction with a three-dimensional sink in order to determine the inflow and outflow velocities. The hover boundary condition described in these two articles is concise and better explained than others. Similar work on the hover boundary condition is also available in an article by Strawn and Ahmad (2000). Pomin and Wagner (2002, 2004) included a better structural model based on Timoshenko beam with the deformable overset grids. The simulation was carried out for a fully articulated 7A model rotor for both hover and high speed forward flight. Comparative rigid blade simulations were carried out to assess the effects of blade dynamics and elasticity on the numerical results. The emphasis of these two articles was on the wake structure, aeroelasticity effects of the blades, and comparison of global thrust and torque coefficients in both hover and forward flight.

Allen (2003) performed detailed simulations of steady and unsteady inviscid flow for hovering. For the unsteady simulation, the BDF time integration method used 30, 60, 120 and 360 steps per revolution and up to 20 revolutions. 30,000 iterations were required to obtain a converged solution for comparison with a transonic hover case from Caradonna and Tung with a tip Mach number of 0.784 and a collective pitch of 8^0. Allen (2003) further worked on forward flight simulation on a single processor based on the Caradonna and Tung two-bladed rotor model with a tip Mach number of 0.6 and a collective pitch of 8^o. The advance ratio was set at $\mu=1/3$. Simulation was run with 36 steps per revolution and 20 revolutions in total for convergence. The computation for this simulation took 40,000 time steps with 1.3 million mesh points. The actual time of simulation was one week on an EV6 500 MHz processor. Allen (2007) ran simulation of an ONERA 7A four-bladed rotor with up to 192 blocks, 32 million mesh points and up to 1,024 processors. Steijl et al. (2006) described and demonstrated their approach to helicopter rotor in both hover and forward flight simulation with RANS calculations. The time accurate simulation used dual time stepping with the BDF scheme. For each pseudo time solution, 25–35 steps of generalized conjugate gradient method were required to drive the residual down three orders of magnitude. The far field at the bottom of the domain for the hover case followed an empirical relation first given by Biava and Vigevano (2002), rather than the more commonly used relation of Srinivasan and McCroskey (1993). The authors suggested that periodic rotor blade motions were required to trim the rotor in forward flight. However, the blades were assumed to be rigid but the rotor was fully articulated with separate hinges for each blade. Their approach allowed for rotors with different numbers of blades and hub layouts. They used a grid deformation scheme that preserved the quality of their multi-block, structured, body-fitted mesh. Comparison of both hover and forward flight for rigid and fully articulated rotor were demonstrated using the Caradonna and Tung rotor and ONERA 7A/7AD1 rotors. For the latter, pitch changes, flapping and lead–lag deflections were included in the forward flight simulation.

2.1.3 HYBRID SOLVERS

Recently, the idea of a hybrid solver in which wake model is integrated into a regular flow solver has proved to be popular. The model is coupled with either a full potential flow or Euler solver in the outer region far from the rotor and a RANS solver near the rotor region.

Hassan et al. (1992) used a finite difference scheme for the prediction of three dimensional blade–vortex interactions via the velocity transpirational approach because of its simplicity and low implementation cost. The interaction velocity field was obtained through a nonlinear superposition of the rotor flow field computed by the unsteady three-dimensional Euler equations. The embedded vortex wake flow field was computed using the Biot–Savart law. The three-dimensional grid was constructed by stacking two-dimensional, near orthogonal C-mesh grids generated around the blade radial. The two-dimensional grids were constructed using the method suggested by Jameson (1974). A hybrid (implicit–explicit) alternate direction implicit (ADI) scheme was used to solve the discretized equations. In the spanwise direction, the fluxes were solved explicitly while in the normal and chordwise directions, the fluxes were implicitly evaluated. Time stepping was carried out by a two-point first order backward difference scheme. The non lifting forward flight calculation was compared to the experiment of Caradonna et al. (1984) with good agreement for the upstream generated vortex.

Yang et al. (2002) carried out helicopter rotor simulations using a hybrid solver with a potential flow solver in the outer region far from the rotor and a RANS solver near the blade region. Free and prescribed wake models were added to account for the tip vortex. The full potential solver accounts for inviscid isentropic flow in the far field. The simulation was capable of resolving the moving mesh with elastic deformations. The free and prescribed wake models were used to account for tip vortex effects once the vortex generated by the blade leaves the viscous flow region and enters the region that is in the potential flow solver. The inviscid fluxes were computed using an upwind essentially non oscillatory (ENO) scheme. The unsteady term was solved using a three-factor ADI scheme. Baldwin–Lomax (Baldwin and Lomax, 1978) turbulence model was used to calculate the eddy viscosity. Sample results were presented for the two-bladed AH–1G rotor in descent and the UH–60A rotor in high speed forward flight with reasonable accuracy.

Similarly, Zhao et al. (2006) coupled a full potential flow solver with a RANS solver and a free wake model for prediction of the three-dimensional viscous flow field of a helicopter rotor under both hover and forward flight. The compressible RANS solver was used for the blade and near blade area for the viscous effects. The compressible full potential flow was used to model the inviscid isentropic potential in the region far from the rotor and finally, the free wake model was used to account for tip vortex effects in the potential flow after the vortex leaves the region of the RANS solver. The BDF scheme was used for time integration and the MUSCL scheme for spatial discretization with flux difference splitting scheme without the use of artificial viscosity. The embedded grids used in this study consisted of the cylindrical O–H background grids and the body-fitted C–H mesh around the blade. The number of grid points for the background mesh was 41 x 71 x 72 with 41 points in the radial direction, 71 points in the axial direction and 72 points in the circumferential direction. 65 x 33 x 193 mesh points were used for the blade with 65 points in the span wise direction, 33 points in the normal direction and 193 points in the chord wise direction. An implicit dual-time stepping scheme with a second order BDF was adopted, using an explicit

Runge–Kutta five stage scheme for integrating the pseudo time solution for each step. Five cases were simulated; two hover cases and three forward flight cases. The numerical results using the hybrid solver were in good agreement with the experimental data for the hover case, and quite good for the forward cases considering that the data came from flight tests and the grids used in this work only covered the entire rotor without the fuselage or tail rotor. It was also shown that the computational effort using the hybrid solver was reduced by approximately 43 % compared to a typical RANS solver (38 hours vs. 62 hours).

Bhagwat et al. (2005) recently developed a new potential flow based model for hover performance prediction with focus on the capture of the wake system (location and circulation distribution). Hover performance prediction tools traditionally consists of prescribed wake and free wake methods coupled to full potential flow, Euler or RANS solver. These methods, including Lagrangian free wake methods are susceptible to instabilities. Additionally, most methods require wake trajectories, which are not actually free and have to be derived from experimental data sets. The authors derived a new method called vorticity embedding, which claimed to permit free wake vortex convection. This is the second generation of such a method. The first generation vorticity embedding method can be found in the paper of Ramachandran et al. (1994). A hybrid RANS solver coupled with a free wake model was also tested. The numerical results were compared with UH–60A performance. An approximate factorization scheme based on Jameson (1979) was used to solve the full potential flow equation. Bhagwat et al. (2006) later placed more emphasis on the RANS solver by placing a small C-mesh around the blade region coupled with the vorticity embedding wake model. The solver used in the work was the TURNS code developed by Srinivasan et al. (1990).

Approaching the problem via commercial software, Xu et al. (2005) simulated a rigid two-bladed rotor of Caradonna et al. and a Robin four-bladed rotor in forward flight with cyclic pitching using a Chimera moving grid approach. They used the commercial code CFD–FASTRAN, in which the compressible Euler equations are spatially discretized using a finite volume method. The flux vectors were evaluated using Roe linearization with different limiters. The time marching algorithm was the Jacobi iterative implicit scheme (this is a first order accurate scheme). For the four-bladed Robin rotor, 30 x 143 x 63 grid points were used for blade with 30 points in the normal direction, 143 points in the chord wise direction and 63 points in the span wise direction. Additionally, the parent grid size was 64 x 60 x 87 for one half of the cylindrical domain. Thus for the entire computational domain, there were just over 1.75 million mesh points. Each time step corresponded to 1.184 x 10^{-5} seconds, this represents the incremental rotational angle of only 0.15. Results for forward flight showed quite good agreement in comparison with experimental data.

2.1.4 FOURIER-BASED TIME INTEGRATION SOLVERS

Recently, there have been two other groups who have been working on Fourier-based time integration solves for rotorcraft simulation purposes. The first group of people are from Syracuse University (Kumar and Murthy, 2007, 2008), and the second is from Duke University (Ekici et al., 2008). The first group's method is based on forward and backward Fourier transforms similar to the NLFD technique. However, their results show large discrepancy with experimental data. The group from Duke University has shown good results compared to the experimental data, although their code still required thousands of time steps to converge to a reasonable solution. Additionally, Ekici et al.(2008) also proposed a new periodic boundary condition so that it is possible to perform forward flight calculation using only one blade (as opposed to simulating the entire rotor as has been traditionally done).

2.1.5 WIND TUNNEL EXPERIMENTS

One of the most cited experimental works in helicopter simulation is the experiment of a model helicopter rotor in hover by Caradonna and Tung (1981) due to its simplicity. It is still widely used today as a benchmark test case for simulation of helicopter rotor in hover. Their experiment included a wide range of tip Mach numbers from subsonic to transonic flow regimes. They used a large chamber with special ducting designed to eliminate the circulation caused by the rotor. The rotor was a two-bladed model with NACA 0012 profile which was untwisted and untapered. The aspect ratio of the blades was six, with a radius of 1.143 meter. NASA Rotorcraft Division has also conducted other experiments on model helicopter rotors in forward flight such as those described in the NASA Technical Reports of Caradonna et al. (1984, 1988) and Owen and Tauber (1986). The results in chapter 5 compare the computational results with the data from Caradonna et al. (1984). The model used in this experiment was a two-bladed teetering-rotor system equipped with full collective and cyclic control. The blades were 7 feet in diameter and 6 inches in chord with an untapered and untwisted NACA 0012 profile; this gives an aspect ratio of 7. These blades were constructed almost entirely of balsa and carbon/epoxy composites, so they were quite stiff.

2.2 COAXIAL ROTOR STUDIES

The aerodynamics of a 1.67 ft (0.509 m) diameter coaxial rotor in the static-thrust condition was investigated by Taylor (1950). The rotor had H/D=0.17, solidity of 0.08, and $Re_{0.75}=0.0825\times10^6$. Flow visualization was accomplished by introducing balsa dust into the air flow and photographing the results. For the coaxial configuration, it was found that the vortex filaments emanating from the blade tips of the upper and lower rotors did not merge or cancel one another but retained their separate identities in the wake. Taylor reported that "the blade-tip vortex patterns for the upper and lower rotors of the coaxial configuration bracket the pattern obtained for the single-rotor arrangement due to mutual interference effects." This implied that the upper and lower rotor wakes contracted radially inward at a faster and slower rate, respectively, than an isolated single (upper or lower) rotor and that this effect was caused by rotor mutual interaction.

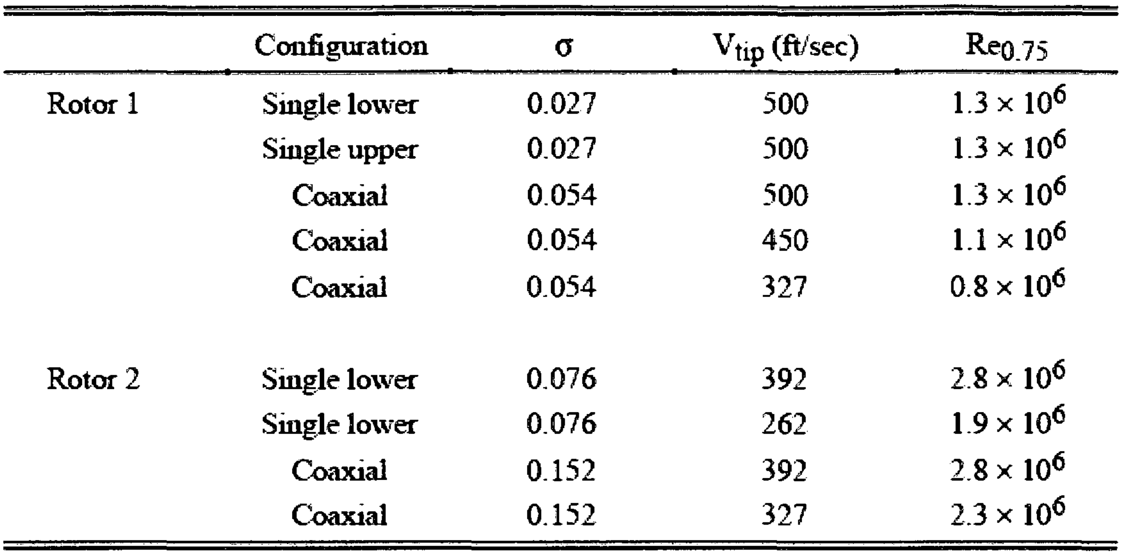

	Configuration	σ	V_{tip} (ft/sec)	$Re_{0.75}$
Rotor 1	Single lower	0.027	500	1.3×10^6
	Single upper	0.027	500	1.3×10^6
	Coaxial	0.054	500	1.3×10^6
	Coaxial	0.054	450	1.1×10^6
	Coaxial	0.054	327	0.8×10^6
Rotor 2	Single lower	0.076	392	2.8×10^6
	Single lower	0.076	262	1.9×10^6
	Coaxial	0.152	392	2.8×10^6
	Coaxial	0.152	327	2.3×10^6

Figure 2.1: Test conditions for Harrington's experiment (Harrington, 1951).

An experimental investigation of the static-thrust performance of a coaxial rotor was carried out by Harrington (1951) in the Langley Full-Scale Tunnel (LFST) in 1951. Two untwisted 25 ft (7.62 m) diameter rotors were tested in both coaxial and single-rotor configurations. Rotor 1 had H/D = 0.093 with blades tapered in planform and thickness. The maximum disc loading of rotor 1 was 3.3 lb/ft2 (158 N/m2). Rotor 2 had H/D=0.080 with blades tapered in thickness but not in planform. The maximum disc loading for rotor 2 was 2.5 lb/ft2 (120 N/m2).

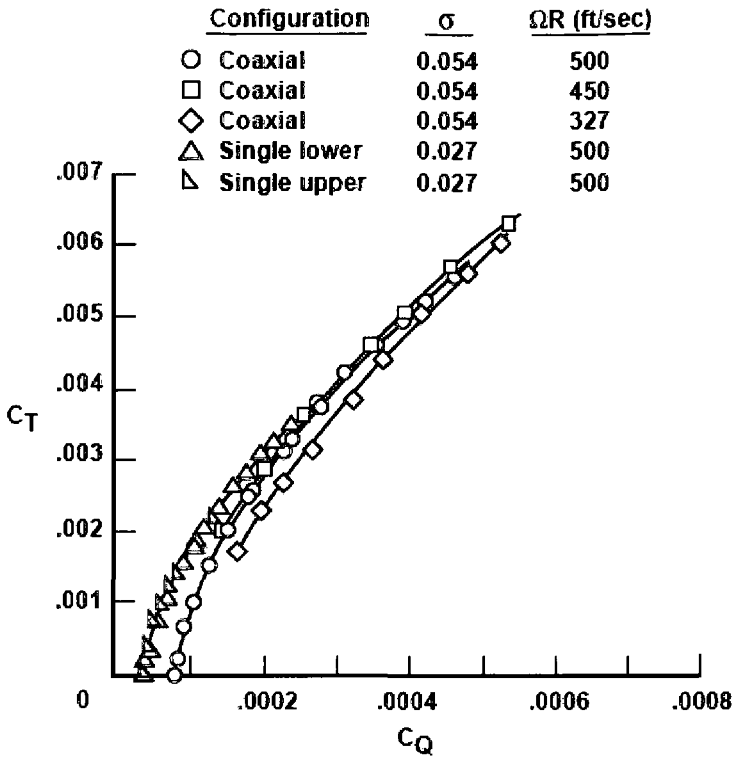

Figure 2.2: Scale effect on Rotor 1 performance at 327 ft/sec, H/D=0.093 (Harrington, 1951).

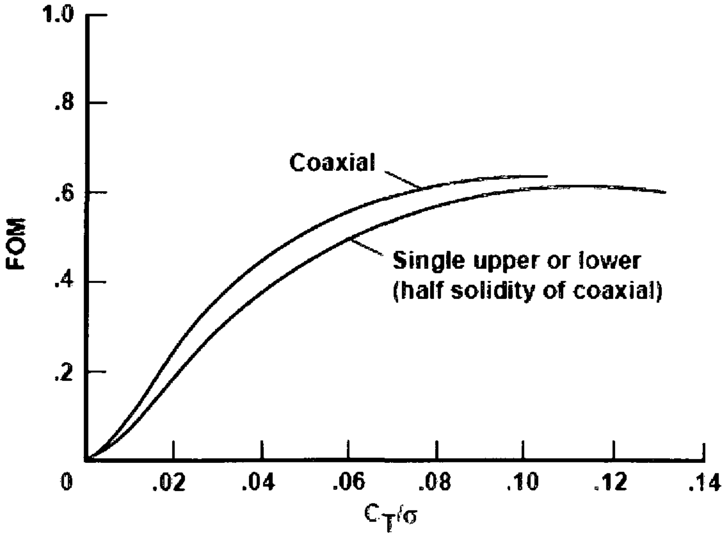

Figure 2.3: Effect of solidity on rotor figure of merit (Harrington, 1951).

When Rotor 1 was tested, a performance offset caused by a scale effect was observed at a tip speed of 327 ft/sec ($Re_{0.75}=0.8 \times 10^6$), which led to an average 7% increase in power for a given thrust (Figure 2.2). This scale effect was lessened for tip speeds of 450 and 500 ft/sec, ($Re_{0.75}=1.1 \times 10^6$ and 1.3×10^6, respectively). Differential collective pitch was also applied to both rotors to deliberately create a non-torque-balanced coaxial system. This resulted in a 2% increase in power compared with the torque-balanced data. Figure 2.3 summarizes Harrington's (1951) figure of merit results for rotor 1. The calculated difference is due to a difference in solidity (0.027 vs. 0.054) and not due to a difference in rotor configuration.

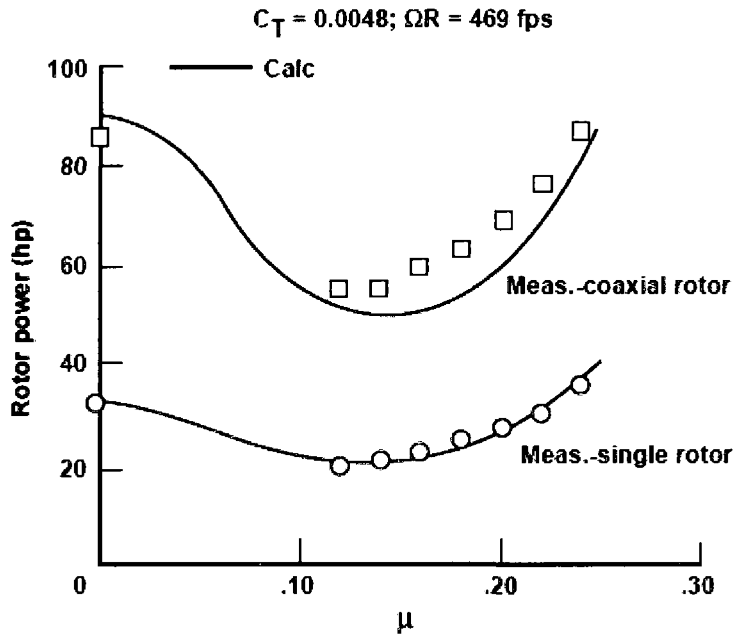

Figure 2.4: Experimental results and equivalent solidity single rotor theory for level flight. (coaxial) = 0.054, (single) = 0.027, H/D = 0.093 (Dingeldein, 1954).

The forward flight performances of single and coaxial rotors were also obtained by Dingeldein (1954) using rotor 1. The tests were performed at constant thrust coefficient and rotor speed for various advance ratios. The theoretical predictions for a single rotor agreed well with the experimental single rotor. It was found that up to 14% more power was required for the coaxial rotor than for a theoretical single rotor of equivalent solidity under the same conditions. It was concluded that this difference was caused by increases in both profile and induced losses associated with interference effects. Analysis methods employed that time could not model this effect. Dingeldein (1954) concluded, "the indications remain, however, that the coaxial arrangement tested required more power in forward flight than an equivalent single rotor, although there are certain advantages to the configuration which may offset the larger power requirement in certain applications."

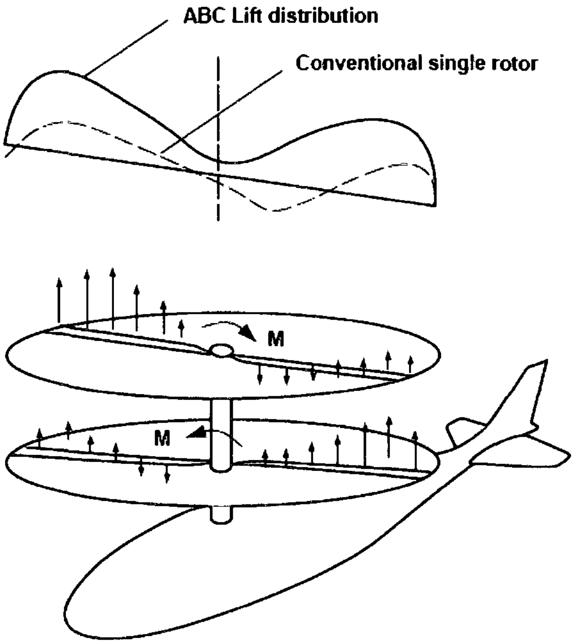

Figure 2.5: Schematic of the advancing blade concept.

The ABC rotor system, consisting of two coaxial counter-rotating, hingeless rotors with a small rotor spacing, took advantage of the aerodynamic lift potential of the advancing blades. At high speeds, the retreating blades were unloaded, with most of the load being carried on the advancing sides of both rotors, thereby eliminating the penalties of retreating blade stall.

Developmental work began in 1965 at the United Aircraft Research Laboratories (UARL) which included small scale rotor tests and theoretical studies.

Performance data and flow visualization pictures were taken in order to compare coaxial with single rotors. Vortices from the upper rotor were seen to move radially inward and downward faster than vortices from the lower rotor. Figure 2.6 shows performance data at an unspecified rotor spacing.

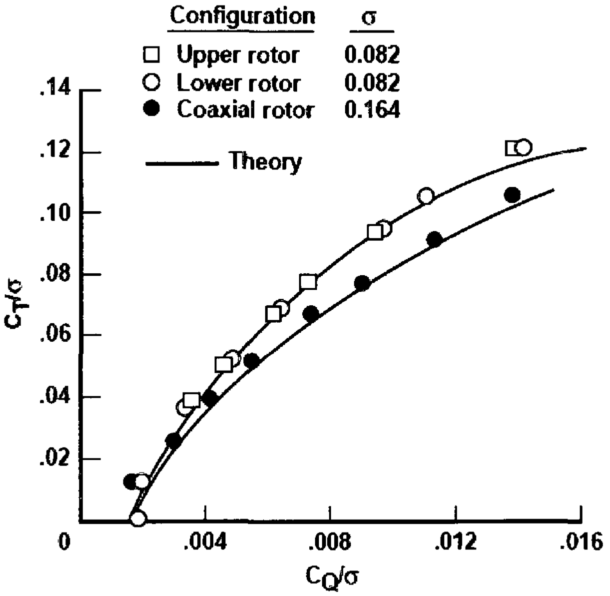

Figure 2.6: Comparison of theoretical and experimental static-thrust performance of model ABC rotor, H/D not reported (Cheney, 1969).

Total power for the coaxial rotor experiment was 3–9% less than the equivalent single-rotor theory; these results are comparable to those obtained by Harrington. It was inferred that there was a beneficial effect on total performance which was attributed to reduced swirl velocity in the rotor wake, although this conclusion cannot be justified based on the experimental results. It was also concluded that rotor spacing had little effect on performance (although only two different rotor spacings were tested). Forward flight performance and blade stress characteristics were examined with a 1/10-scale rotor with dynamically scaled blades. Forward speeds from 60 to 180 knots were tested, with spacings between H/D=0.07 and H/D=0.10; no significant effects on performance or stress were observed.

The first flight of the ABC aircraft (XH-59A) in pure helicopter mode occurred July 26, 1973. The aircraft had a 36 ft (10.97 m) diameter rotor, H/D=0.069, total rotor solidity of 0.127, blade taper ratio of 2:1 with –10° nonlinear twist, and disc loading of 10.3 lb/ft2 (493 N/m2). On August 24, 1973, this first aircraft, while flying at 25–30 knots at an altitude of about 50 ft (15.24 m), pitched nose-up, lost altitude, and was extensively damaged in a hard, tail-first landing.

Russia is the world's largest user of coaxial rotor helicopters. Their knowledge of the design can be attributed to both the work done by the Kamov Design Bureau and the research conducted by the Central Aero-hydro-dynamics Institute (TsAGI). Despite the extensive Soviet research, very few Soviet works have been translated and published in the West; only recently has some of this material been released.

Coaxial rotor aerodynamic theory is mentioned in two translated Soviet texts published in the West, "Theory of the Lifting Airscrew" and "Helicopters". The first of these covers a wide spectrum of analytical methods which include modeling blades by both lifting line and vorticity surfaces, using various wake types (free wakes and cylindrical wakes with skew angles from 0° to 90°), and applying vortex (Joukowsky) theory. These methods are simplified in "Helicopters" with an emphasis on obtaining practical application tools. Rotor blades are modeled solely by single lifting lines, and rotor wakes are assumed to be cylindrical in both hover and climb and flat in forward flight.

"Helicopters" also develops a rotor performance estimate based on a separation distance of H/D=0.1, which is a typical value. The individual rotors were treated as being in a climb, where the climb speed was equal to the velocity induced by the other rotor (and therefore different for each rotor). In solving the induced velocities, it was found that $C_{Tlow}/C_{Tupp}=0.86$. Experiments by A. D. Levin on a coaxial rotor model of diameter 6.67 ft (2.034 m), s=0.0445, H/D=0.0985 with blades of –12° twist and $C_{Tco}=0.0036$ gave $C_{Tlow}/C_{Tupp}=0.87$. The main conclusion derived here was that "the average aerodynamic characteristics of a coaxial configuration are practically independent of the distance between the rotors". According to the author, this conclusion is said to be confirmed by tests performed by Lessley reported in TsAGI Report No. 31, 1941, by V. I. Shaydakov (1941) who applied momentum theory and also by V. S. Vozhdayev who applied blade vortex theory. It was also concluded that the "distance between rotors in the coaxial configuration affects only the distribution of thrust between the upper and lower rotors." Consequently, a coaxial rotor in axial flight is treated as an equivalent solidity single rotor, while accounting for the rotor mutual influence.

Another design method for coaxial rotors in axial flow was reported by Kvokov. The rotors were represented by lifting discs in which the circulation distribution was constant in azimuth but varied with radial position. A prescribed trajectory prepositioned the wake vortices. Assuming an ideal, incompressible fluid, expressions were obtained for the total induced velocity at an arbitrary point in the flow. Two-dimensional blade element theory was used to calculate the lift and drag of the rotors, with profile-drag losses and a tip loss factor being added. The single-rotor wake geometry was also corrected to allow for the mutual interaction of the rotors. Consequently, theoretical results were "tuned" to fit the experimental data.

A coaxial rotor experiment was described by Antopov (1980). Figure 2.7 shows a rotor of 6.56 ft (2 m) diameter rotor with variable spacing ($0.06 < H/D < 0.12$) used for axial flight testing. The rotor system can also be tilted 90° into a vertical position, with the free-stream flow approaching edgewise, to simulate forward flight [Coleman, 1997]. Results of tests conducted by A. D. Levin (1980) using the above apparatus at $H/D=0.088$ showed that the effect of the upper rotor on the lower is much greater than the reverse, and that this difference decreases with increasing advance ratio. The upper rotor was said to have the largest effect on the lower rotor at an advance ratio of 0.05, while the lower effects the upper the greatest at an advance ratio of 0.1.

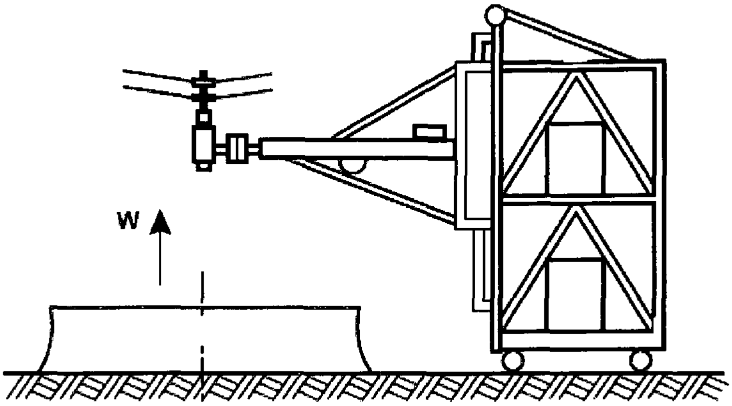

Figure 2.7:. Coaxial rotor in a wind tunnel (Antopov, 1980).

The aerodynamic coupling between the two rotors is strongly influenced by descending flight (Anikin, 1991). Extensive experimental and theoretical research was carried out in the area of unsteady blade flapping motion (this phenomenon was not exactly defined). The minimum separation distance between any two passing blades as a function of advance ratio was also discussed by Anikin (1991).

More recently, Su and Cao (2002) used a nonlinear inverse method to study the coaxial helicopter maneuvers. A framework to model the aerodynamics of coaxial heliocopters was also suggested by Kim and Brown (2008). Wachspress and Quackenbush (2006) investigated the impact of coaxial rotor design on performance and noise. Finally, Bermes, et al. (2008) reported on the center of gravity steering of a coaxial helicopter.

CHAPTER III

MOTIVATION AND OBJECTIVES

3.1 MOTIVATION

An accurate computation of helicopter rotor flows in both hover and forward flight is a particularly challenging problem due to the inherent difficulties that it entails. Many authors have undertaken the numerical simulation of flows around rotary wings. Successful results have been reported for conventional (single) rotors in hover and forward flight regimes. However, the effect of dynamic stall on a retreating blade is still a challenging problem for high forward flight speeds.

Once a single-rotor helicopter is in forward flight, a phenomenon manifests itself, called "dissymmetry of lift" which possesses the potential to disrupt stable flight at speed. Dissymmetry of lift imposes an upper speed limit (known as the Never-Exceed Speed or V_{NE}) upon single-rotor helicopters, by virtue of the fact that during one rotation of the rotor disc, a rotor blade experiences, in extreme parts of the flight envelope, two widely contrasting unstable conditions. On the advancing side of the rotor disc, the blades travel through the air sufficiently fast for the airflow over them to become transonic or even supersonic, which causes fundamental changes in the airflow over the rotor blades. On the retreating side of the rotor disc, the rotors move through the air much slower, possibly slow enough to enter the stall condition, thus failing to produce lift.

Coaxial rotors may solve the problem of dissymmetry of lift because one set of rotors is cancelled by the corresponding increased lift on the same side of the other set of rotors, and vice versa. The result is a helicopter that can fly, at least theoretically, faster than a single-rotor design, and be more stable in the extreme parts of the flight envelope. Although there are a few helicopters in service with coaxial rotors, a computational model to analyze the interaction of the flows generated by the two rotors has not been yet reported. Furthermore, a parametric study to achieve better coaxial rotor designs cannot be found at least in the open literature.

3.2 OBJECTIVES

The main goal of this study is to model, simulate and analyze the flowfields around coaxial rotors. However, building up to this goal, the scope of the investigation has been broadened and required the following objectives:

- Validation of the presently constructed mathematical and computational methodologies for rotorcraft aerodynamics within the limitations of the data available
- Test different types of turbulence models for the validation cases and compare their degrees of success
- Develop computational simulations of the flowfields around a single-rotor in hover then in forward flight
- Compare the lift produced by blades made of different NACA airfoil cross sections when the rotor is in hover
- Observe and analyze the dissymmetry on the advancing and the retreating blades at various forward flight speeds
- Extend the computational model to coaxial rotors in hover then in forward flight
- Study the effect of rotor seperation distance on the produced lift
- Verify the aerodynamic symmetry in forward flight proposed by the "advancing blade concept"

It should be noted that the blade-vortex interaction (BVI) is outside the scope of the present work. Also, dynamic stall and reverse flow region on the retreating blade, which are important topics for rotorcraft aerodynamics, are not considered herein. To simplify the analyses, the rotor blades are assumed to be rigid, hence the aeroelastic effects are not been considered, either. Finally, the present study does not include a survey on the effects of phase shift between rotors that may produce the optimal operation.

CHAPTER IV

MATHEMATICAL FORMULATION AND METHODOLOGY

Explained in this chapter are the governing equations and the common numerical formulations used in constructing the mathematical and the computational models. Further details of some of the numerical algorithms for specific cases are deferred to be discussed in the subsequent chapters.

4.1 GOVERNING EQUATIONS

The Navier–Stokes Equations are the most general description of the fluid flow in thermodynamic equilibrium (Berkman and Sankar, 1997). It is basically the collection of the conservation of mass, the conservation of momentum and the conservation of energy equations written for a Newtonian fluid. The integral form, which is also the basis of all finite volume algorithms, can be written as,

$$\frac{\partial}{\partial t}\int_{\Omega}\vec{q}\,d\Omega+\oint_{S}\vec{F}\cdot d\vec{S}=0 \qquad (2.1)$$

The differential form can be written as,

$$\frac{\partial\vec{Q}}{\partial t}+\frac{\partial\left(\vec{E}-\vec{E}_v\right)}{\partial x}+\frac{\partial\left(\vec{F}-\vec{F}_v\right)}{\partial y}+\frac{\partial\left(\vec{G}-\vec{G}_v\right)}{\partial z}=0 \qquad (2.2)$$

where $\vec{q}$ is the vector containing the conservative variables.

$$\vec{q} = \begin{bmatrix} \rho \\ \rho u \\ \rho v \\ \rho w \\ E \end{bmatrix} \tag{2.3}$$

and $\vec{F}$ is the matrix containing the flux terms. The columns of $\vec{F}$ are as follows:

$$\vec{F}_1 = \begin{bmatrix} \rho u \\ \rho u^2 + p - \sigma_{xx} \\ \rho uv - \tau_{xy} \\ \rho uw - \tau_{xz} \\ (E+p)u - u\sigma_{xx} - v\tau_{xy} - w\tau_{xz} - k\dfrac{\partial T}{\partial x} \end{bmatrix} \tag{2.4}$$

$$\vec{F}_2 = \begin{bmatrix} \rho v \\ \rho uv - \tau_{xy} \\ \rho v^2 + p - \sigma_{yy} \\ \rho vw - \tau_{yz} \\ (E+p)v - u\tau_{xy} - v\sigma_{yy} - w\tau_{yz} - k\dfrac{\partial T}{\partial y} \end{bmatrix} \tag{2.5}$$

$$\vec{F}_3 = \begin{bmatrix} \rho w \\ \rho uw - \tau_{xz} \\ \rho vw - \tau_{yz} \\ \rho w^2 + p - \sigma_{zz} \\ (E+p)w - u\tau_{xz} - v\tau_{yz} - w\sigma_{zz} - k\dfrac{\partial T}{\partial z} \end{bmatrix} \tag{2.6}$$

Where

$$\sigma_{xx} = 2\mu\frac{\partial u}{\partial x} - \frac{2}{3}\mu\nabla\cdot\vec{V} \tag{2.7}$$

$$\sigma_{yy} = 2\mu\frac{\partial v}{\partial y} - \frac{2}{3}\mu\nabla\cdot\vec{V} \tag{2.8}$$

$$\sigma_{zz} = 2\mu\frac{\partial w}{\partial z} - \frac{2}{3}\mu\nabla\cdot\vec{V} \tag{2.9}$$

$$\tau_{xy} = \mu\left(\frac{\partial u}{\partial y} + \frac{\partial v}{\partial x}\right) \tag{2.10}$$

$$\tau_{xz} = \mu\left(\frac{\partial u}{\partial z} + \frac{\partial w}{\partial x}\right) \tag{2.11}$$

$$\tau_{yz} = \mu\left(\frac{\partial v}{\partial z} + \frac{\partial w}{\partial y}\right) \tag{2.12}$$

Note that,

$$\vec{F}_1 = \left(\vec{E} - \vec{E}_v\right) \tag{2.13}$$

$$\vec{F}_2 = \left(\vec{F} - \vec{F}_v\right) \tag{2.14}$$

$$\vec{F}_2 = \left(\vec{G} - \vec{G}_v\right) \tag{2.15}$$

There are six unknowns, ρ , u , v , w , p , E and T , but five equations. To close the system of equations, an equation of state is used:

$$p = (\gamma - 1)\left[E - \frac{\rho}{2}\left(u^2 + v^2 + w^2\right)\right] \tag{2.16}$$

$$T = \frac{\gamma - 1}{R}\left[\frac{E}{\rho} - \frac{1}{2}\left(u^2 + v^2 + w^2\right)\right] \tag{2.17}$$

where R is the gas constant and γ is the ratio of specific heats. $R = 287 m^2/s^2 K$ and $\gamma = 1.4$ for air.

A relation also can be established between the dynamic viscosity and the temperature by using the Sutherland's formula:

$$\mu = 1.458 \times 10^{-6}\, kg \Big/ \left(msK^{\frac{1}{2}}\right) \frac{T^{\frac{3}{2}}}{T + 110.4K} \tag{2.18}$$

k is the thermal conductivity coefficient and can be related to the dynamic viscosity by using Prandtl number $\Pr$, which describes the ratio of momentum and thermal diffusivities:

$$\Pr = \frac{\mu C_p}{k} \tag{2.19}$$

C_p is the specific heat coefficient under constant pressure. With these definitions, we now can define the fluid conductivity as:

$$k = \frac{\mu C_p}{\Pr} \tag{2.20}$$

For the applications in which a rotational motion exists, such as those for turbomachinery or propeller aircraft, a rotating (blade fixed) frame of reference has to be introduced properly to the conservation equations. By using a properly defined rotational frame together with the absolute (inertial) reference of frame and establishing the transformations between the relative and the absolute variables, one can obtain a system of equations to be solved for the proper solutions of flowfields around rotating bodies.

Let us denote the angular velocity of a system rotating steadily by Ω. V_R is the velocity relative to the rotating system and V is the velocity relative to the absolute reference system. Then, the relation between the absolute and the relative velocities can be written as:

$$\vec{V} = \vec{V}_R + \vec{\Omega} \times \vec{r} \tag{2.21}$$

Here, $\vec{r}$ is the distance vector from the center of rotation to cell centers. The term $\vec{\Omega} \times \vec{r}$ is simply the grid velocity or entrainment velocity. Two additional terms comes with momentum equation. First one is the Coriolis force per unit volume defined as:

$$\vec{F}_{cor} = -2\rho\left(\vec{\Omega} \times \vec{V}_r\right) \tag{2.22}$$

and the second one is the centrifugal force per unit volume :

$$\vec{F}_{cent} = -\rho\vec{\Omega} \times \left(\vec{\Omega} \times \vec{r}\right) \tag{2.23}$$

Once the relations are defined properly between absolute and relative velocities, the system of Navier-Stokes equations in relative frame of reference can be written as follows:

$$\frac{d}{dt}\int_{\Omega} \vec{q}_r dV + \oint_{S} (\vec{F}_r - F_v) \cdot d\vec{S} + \int_{\Omega} \vec{T}_r dV = 0 \tag{2.24}$$

This system includes relative velocities and can be solved for the relative flow variables. If one decides to solve the system of equations for the absolute flow variables, the equations have to be rewritten for absolute velocities:

$$\frac{\partial}{\partial t}\int_{\Omega}\vec{q}\,dV + \oint_{S}\left(\vec{F} - \vec{F}_{v}\right)\cdot d\vec{S} + \int_{\Omega}\vec{T}\,dV = 0 \qquad (2.25)$$

The obtained set of equations can be assigned to acquire steady–state, viscous flow solutions around hovering helicopter rotor blades.

4.2. AN OVERVIEW OF FLOW SOLVERS

A typical CFD solver allows us to choose one of the two numerical methods:

- pressure-based solver
- density-based solver

Historically, the pressure-based approach was developed for low-speed incompressible flows, while the density-based approach was mainly used for high-speed compressible flows. Recently, however, both methods have been extended and reformulated to solve and operate for a wide range of flow conditions beyond their traditional or original intent. In both methods the velocity field is obtained from the momentum equations. In the density-based approach, the continuity equation is used to obtain the density field while the pressure field is determined from the equation of state. On the other hand, in the pressure-based approach, the pressure field is extracted by solving a pressure or pressure correction equation which is obtained by manipulating the continuity and momentum equations.

Using either method, the solver should render a solution to the governing integral equations for the conservation of mass and momentum, and (when appropriate) for energy and other scalars, such as, turbulence and chemical species. In both cases a control-volume-based technique is used that consists of the following tasks:

- Divide the domain into discrete control volumes using a computational grid.
- Integrate the governing equations on the individual control volumes to construct algebraic equations for the discrete dependent variables ("unknowns") such as velocity components, pressure, temperature, and conserved scalars.
- Linearize the discretized equations and solution of the resultant linear equation system to yield updated values of the dependent variables.

Both numerical methods employ the finite-volume discretization, but the approach used to linearize and solve the discretized equations is different.

4.2.1 PRESSURE-BASED SOLVER

A pressure-based solver employs an algorithm which belongs to a general class of methods called the “projection method.” In the projection method, the constraint of mass conservation (continuity) of the velocity field is achieved by solving a pressure (or pressure correction) equation. The pressure equation is derived from the continuity and the momentum equations in such a way that the velocity field, corrected by the pressure, satisfies the continuity. Since the governing equations are nonlinear and coupled to one another, the solution process involves iterations wherein the entire set of governing equations is solved repeatedly until the solution converges.

4.2.1.1 THE PRESSURE-BASED SEGREGATED ALGORITHM

The pressure-based solver uses a solution algorithm where the governing equations are solved sequentially (i.e. segregated from one another). Because the governing equations are non-linear and coupled, the solution loop must be carried out iteratively in order to obtain a converged numerical solution.

In the segregated algorithm, the individual governing equations for the solution variables (e.g., *u, v, w, P, T, k,* ε, etc.) are solved one after another. Each governing equation, while being solved, is "decoupled" or "segregated" from other equations, hence its name. The segregated algorithm is memory-efficient, since the discretized equations need only be stored in the memory one at a time. However, the solution convergence is relatively slow, inasmuch as the equations are solved in a decoupled manner. With the segregated algorithm, each iteration consists of the steps illustrated in Figure 4.1 and outlined below:

1. Update fluid properties (e.g. density, viscosity, specific heat) including turbulent viscosity (diffusivity) based on the current solution.

2. Solve the momentum equations, one after another, using the recently updated values of pressure and face mass fluxes.

3. Solve the pressure correction equation using the recently obtained velocity field and the mass-flux.

4. Correct face mass fluxes, pressure, and the velocity field using the pressure correction obtained from Step 3.

5. Solve the equations for additional scalars, if any, such as turbulent quantities, energy, species, and radiation intensity using the current values of the solution variables.

6. Update the source terms arising from the interactions among different phases (e.g., source term for the carrier phase due to discrete particles).

7. Check for the convergence of the equations.

These steps are continued until the convergence criteria are met.

4.2.1.2 PRESSURE-BASED COUPLED ALGORITHM

Unlike the segregated algorithm described above, the pressure-based coupled algorithm solves a coupled system of equations comprising the momentum equations and the pressure-based continuity equation. Thus, in the coupled algorithm, Steps 2 and 3 of the segregated solution algorithm are replaced by a single step in which the coupled system of equations are solved. The remaining equations are solved in a decoupled fashion as in the segregated algorithm.

Since the momentum and continuity equations are solved in a closely coupled manner, the rate of solution convergence significantly improves when compared to the segregated algorithm. However, the memory requirement increases by 1.5 to 2 times that of the segregated algorithm since the discrete system of all momentum and pressure-based continuity equations needs to be stored in the memory when solving for the velocity and pressure fields (rather than just a single equation, as is the case with the segregated algorithm).

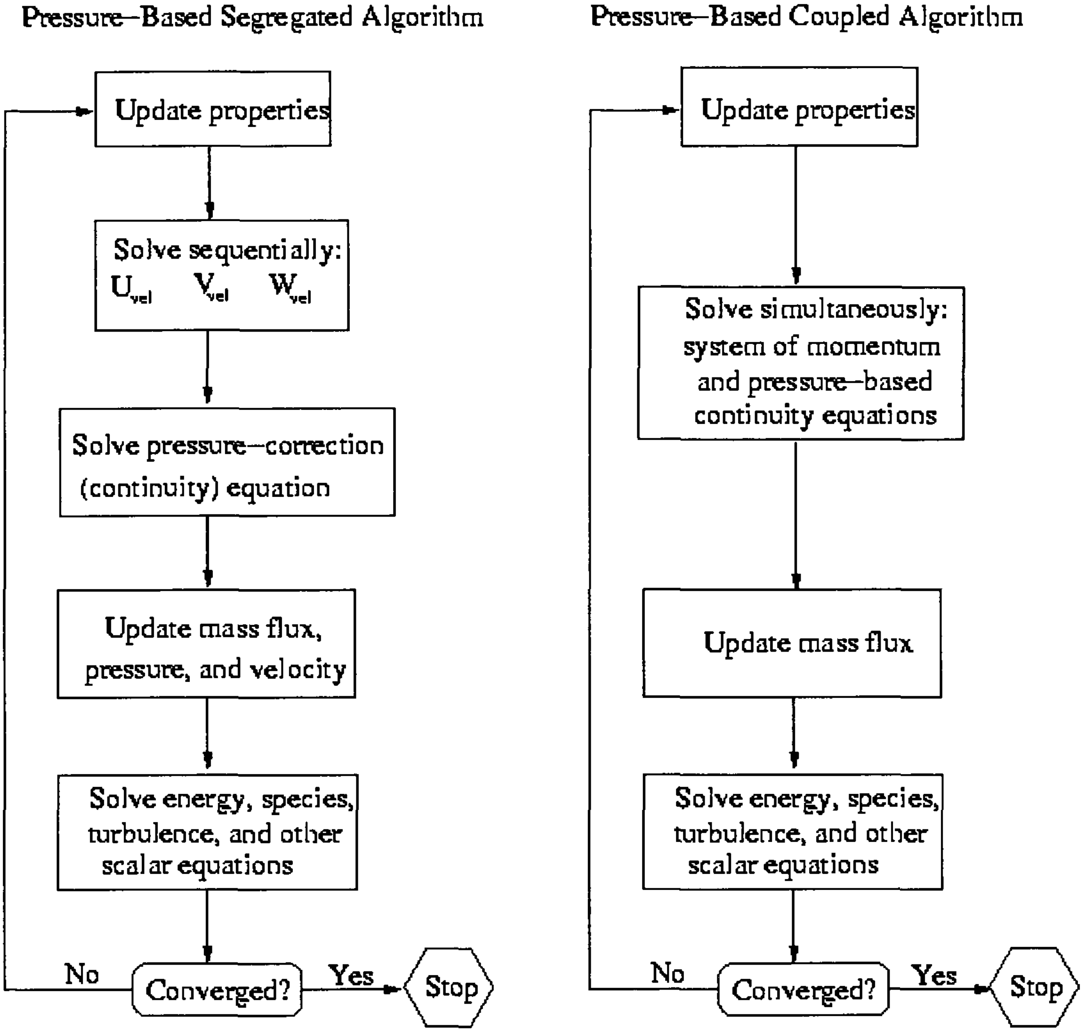

Figure 4.1: Flowcharts of Segregated and Coupled Algorithms.

4.2.2 DENSITY–BASED SOLVER

The density-based solver handles the governing equations of continuity, momentum, and (where appropriate) energy and species transport simultaneously (i.e., coupled together). Governing equations for additional scalars are solved subsequently (i.e., segregated from one another and from the coupled set). Because the governing equations are non-linear (and coupled), several iterations of the solution loop must be performed before a converged solution is obtained. Each iteration consists of the steps illustrated in Figure 4.2 and outlined below:

1. Update the fluid properties based on the current solution. (f the calculation has just begun, the fluid properties will be updated based on the initialized solution.

2. Solve the continuity, momentum, and (where appropriate) energy and species equations simultaneously.

3. Where appropriate, solve equations for scalars such as turbulence and radiation using the previously updated values of the other variables.

4. When interphase coupling is to be included, update the source terms in the appropriate continuous phase equations with a discrete phase trajectory calculation.

5. Check for convergence of the equation set.

These steps are continued until the convergence criteria are met.

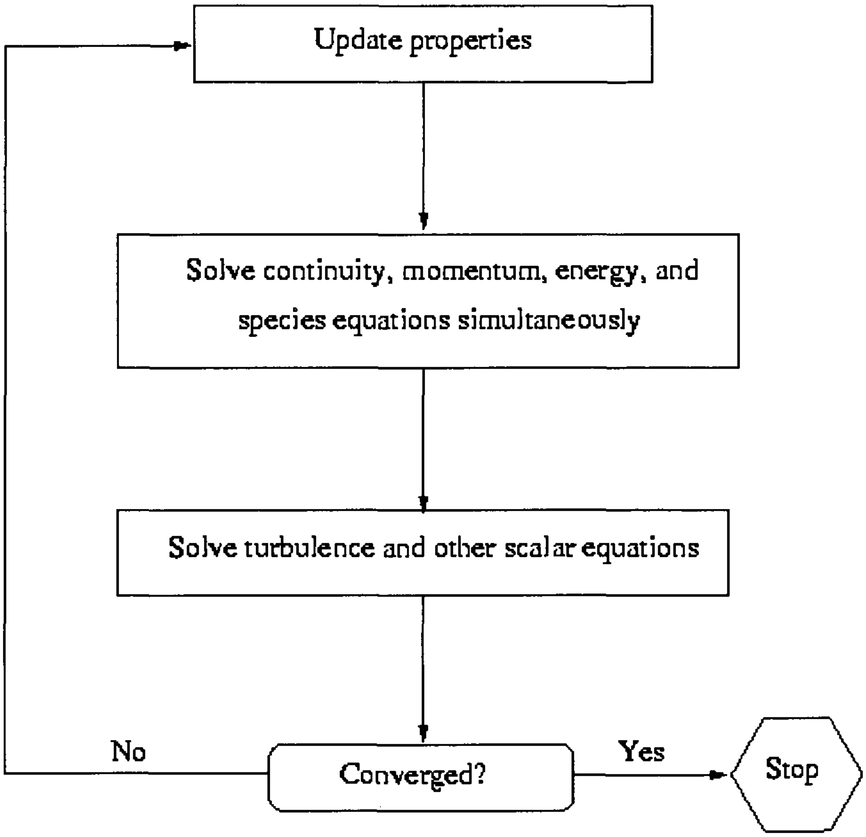

Figure 4.2: Flowchart of Density–Based Algorithm.

In the density-based solution method, one can solve the coupled system of equations (continuity, momentum, energy and species equations if available) using, either the coupled-explicit formulation or the coupled-implicit formulation. The main distinction between the density-based explicit and implicit formulations is described next.

In the density–based solution methods, the discrete, non-linear governing equations are linearized to produce a system of equations for the dependent variables in every computational cell. The resultant linear system is then solved to yield an updated flow-field solution.

The manner in which the governing equations are linearized may take an "implicit" or "explicit" form with respect to the dependent variable (or set of variables) of interest. By implicit or explicit we mean the following:

- **implicit:** For a given variable, the unknown value in each cell is computed using a relation that includes both existing and unknown values from neighboring cells. Therefore, each unknown will appear in more than one equation in the system, and these equations must be solved simultaneously to give the unknown quantities.

- **explicit:** For a given variable, the unknown value in each cell is computed using a relation that includes only existing values. Therefore, each unknown will appear in only one equation in the system and the equations for the unknown value in each cell can be solved one at a time to give the unknown quantities.

In the density-based solution method one has a choice of using either an implicit or explicit linearization of the governing equations. This choice applies only to the coupled set of governing equations. Transport equations for additional scalars are solved segregated from the coupled set (such as turbulence, radiation, etc.). Regardless of whether you choose the implicit or explicit methods, the solution procedure shown in Figure 4.2 is followed.

If one chooses the implicit option of the density-based solver, each equation in the coupled set of governing equations is linearized implicitly with respect to all dependent variables in the set. This will result in a system of linear equations with N equations for each cell in the domain, where N is the number of coupled equations in the set. Because there are N equations per cell, this is sometimes called a "block" system of equations.

A point implicit linear equation solver (Incomplete Lower Upper (ILU) factorization scheme or a symmetric block Gauss-Seidel) is used in conjunction with an algebraic multigrid (AMG) method to solve the resultant block system of equations for all N dependent variables in each cell. For example, linearization of the coupled continuity, x, y, z momentum, and energy equation set will produce a system of equations in which P, u, v, w, and T are the unknowns. A simultaneous solution of this equation system (using the block AMG solver) yields at once updated pressure, *u, v, w* velocity, and temperature fields. In summary, the coupled implicit approach solves for all variables (*P, u, v, w, T)* in all cells at the same time.

If one chooses the explicit option of the density-based solver, each equation in the coupled set of governing equations is linearized explicitly. As in the implicit option, this too will result in a system of equations with *N* equations for each cell in the domain and likewise, all dependent variables in the set will be updated at once. However, this system of equations is explicit in the unknown dependent variables. For example, the *x*-momentum equation is written such that the updated *x* velocity is a function of existing values of the field variables. Because of this, a linear equation solver is not needed. Instead, the solution is updated using a multi-stage (Runge-Kutta) solver. Here you have the additional option of employing a full approximation storage (FAS) multigrid scheme to accelerate the multi-stage solver. In summary, the density-based explicit approach solves for all variables (*P, u, v, w, T)* one cell at a time.

4.3 FINITE VOLUME METHOD

The conservation laws of fluid motion may be expressed mathematically in either differential or integral form. Finite volume methods are based on the discretization of the integral form of the conservation equations directly in the physical space [19]. When a numerical scheme is applied to the differential form of equations, the domain of solution is divided into discrete points, upon which the finite difference equations are solved. On the other hand, when the integral form of the equations is utilized, the domain of solution is divided into small volumes (or areas for a two-dimensional case) whose vertices are the grid points. Since the majority of physical domains are irregular in shape, a coordinate transformation from a physical space to a computational space is performed where the computational domain is rectangular. However, even the coordinate transformation is available, domains which are highly irregular would create serious difficulties in accuracy and convergence of the solution. The reason is that the metrics and the Jacobian of transformation and the corresponding gradients which are used in the governing equations may include numerical discontinuities if the grid system is not relatively smooth. In general, the finite difference methods possess inherited weaknesses for highly complicated domains while finite volume schemes do not encounter such waeknesses (Bridges, 2000). Because the independent variables are integrated directly on the physical domain and therefore, grid smoothness is no longer an important issue.

The computational grid divides the flowfield into computational cells where the grid points are the cell vertices. The finite volume method is based on the discretization of the general form of conservation law with the surface integral replaced by the sum of discrete integrals over the faces of the computational cell. The discretized form of equation can be written as:

$$\frac{\partial}{\partial t}\left(q_{i,j,k}\Delta V_{i,j,k}\right)+\sum_{sides}\left(\vec{F}\cdot\vec{S}\right)=0 \qquad (2.26)$$

Here, $q_{i,j,k}$ refers to the value of q at the cell center (i,j,k), $\Delta V_{i,j,k}$ refers to the volume of the computational cell and the term with the summation mark refers to total flux through all external faces. It is generally considered that $q_{i,j,k}$ is the average value of q in the (i, j, k) ordered cell. But in order to calculate a surface flux, it is convenient to think of $q_{i,j,k}$ as the value of q at some average point in the cell. A charecteristic of the finite volume method is that the precise location of this average point is not required during the calculation (Hirsch, 1998). Only in the output of the solution, the location of this point is desired. Some investigators have suggested the cell centroid for this point. This is strictly valid if and only if all the components of q vary linearly througout the cell. Since the distribution of q is not known, the centroid has no particular advantage over the cell center defined as the vectorial average of the cell vertices. The latter point is easier to calculate, and is therefore preferable. One also has to define how to estimate the volume and cell surface areas, and how to approximate the fluxes at the faces. On the other hand, the sum of the cell volumes should be equal to the volume of whole domain. Another important constraint that has to be satisfied is the closed–cell condition which is defined as follows:

$$\sum_{sides} \vec{S} = 0 \tag{2.27}$$

For a three-dimensional problem, the computational cells are hexahedrons as illustrated in Figure 3.1, where ξ, η and ζ denote the curvilinear coordinates. For a hexahedron, the cell surface areas can be approximated as the cross products of the diagonal vectors. Here, one has to properly take into account the direction of the surface normal. The surface area vectors are computed such that the surface normal of a constant ξ-face always points positive ξ-direction.

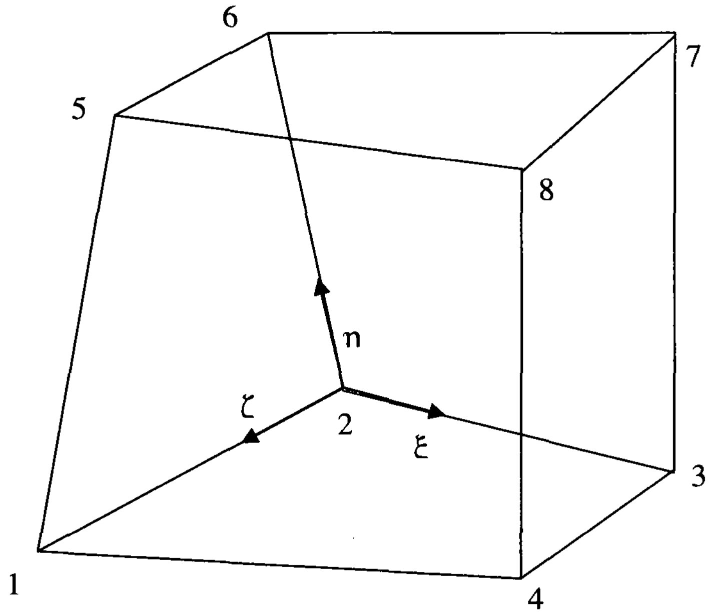

Figure 4.3: Typical hexahedral cell.

Here, one has to properly take into account the direction of the surface normal. The surface area vectors are computed such that the surface normal of a constant ξ-face always points positive ξ-direction. Then, the surface area vector of face 1562, for example, can be computed as (Hirsch, 1998):

$$\vec{S}_{1562} = \frac{1}{2}\left(\vec{r}_{61} \times \vec{r}_{25}\right) \tag{2.28}$$

The cell volume can be computed with the following equation (Hirsch, 1998):

$$\Delta V_{12345678} = \frac{1}{6}\left[\left(\vec{S}_{1485} + \vec{S}_{1234} + \vec{S}_{1562}\right)\cdot\left(\vec{r}_7 - \vec{r}_1\right)\right] \tag{2.29}$$

where i, j and k denote the indices in the ξ, η and ζ surfaces respectively. The integer subscripts indicate the cell centers and the fractional subscripts indicate cell faces. Equation (2.26) can be rewritten as:

$$\begin{aligned} &\frac{\partial}{\partial t}\left(q_{i,j,k}\Delta V_{i,j,k}\right) + \vec{F}_{i+\frac{1}{2},j,k}\cdot\vec{S}_{i+\frac{1}{2},j,k} - \vec{F}_{i-\frac{1}{2},j,k}\cdot\vec{S}_{i-\frac{1}{2},j,k} \\ &\quad + \vec{F}_{i,j+\frac{1}{2},k}\cdot\vec{S}_{i,j+\frac{1}{2}} - \vec{F}_{i,j-\frac{1}{2},k}\cdot\vec{S}_{i,j-\frac{1}{2},k} \\ &\quad + \vec{F}_{i,j,k+\frac{1}{2}}\cdot\vec{S}_{i,j,k+\frac{1}{2}} - \vec{F}_{i,j,k-\frac{1}{2}}\cdot\vec{S}_{i,j,k-\frac{1}{2}} = 0 \end{aligned} \tag{2.30}$$

4.4 BOUNDARY CONDITIONS

The numerical solution of the governing equations requires the appropriate application of the boundary conditions. In this thesis different types of boundary conditions are applied such as wall boundary conditions, farfield boundary conditions, and the periodic boundary conditions.

Wall boundary conditions are applied at the airfoil surfaces. Computation of the fluxes are performed by using absolute velocities. But boundary conditions are applied at the wall surface using relative velocities. Therefore, absolute velocities are transformed to relative velocities. That is performed as:

$$u_{rel} = u_{abs} + \omega \times z(i, j, k) \qquad (2.31)$$

$$v_{rel} = v_{abs} \qquad (2.32)$$

$$w_{rel} = w_{abs} - \omega \times x(i, j, k) \qquad (2.33)$$

For viscous flow calculations no slip boundary conditions are applied for the velocity as:

$$\vec{V}_{rel}\Big|_{surface} = 0 \qquad (2.34)$$

The pressure is obtained by setting the normal pressure gradient to zero. That is:

$$\frac{\partial P}{\partial n}\bigg|_{surface} = 0 \qquad (2.35)$$

The density is extrapolated from the interior. Total energy is obtained from the equation of state.

One–dimensional Riemann invariants are utilized for the farfield boundary conditions. For a subsonic farfield, the fixed and the extrapolated Riemann invariants are defined as (Agarwal and Deese, 1997):

$$R_\infty = V_{n\infty} - \frac{2c_\infty}{\gamma - 1} \tag{2.36}$$

$$R_e = V_{ne} - \frac{2c_e}{\gamma - 1} \tag{2.37}$$

where ∞ and e indicates freestream and the values extrapolated from the interior cells, respectively, V_n and c are the velocity component normal to the boundary and the local speed of sound, respectively.

Actual normal velocity and the actual speed of sound at the farfield boundary can be obtained by using these invariants as:

$$V_n = \frac{1}{2}(R_e + R_\infty) \tag{2.38}$$

$$c = \frac{1}{4}(\gamma - 1)(R_e - R_\infty) \tag{2.39}$$

At the outflow boundary, tangential velocity components and entropy are extrapolated from the interior cells while at an inflow boundary they are assigned as having farfield values.

CHAPTER V

VALIDATION OF THE PRESENT METHODOLOGY

5.1 CARADONNA–TUNG ROTOR IN HOVER

The validation methodology has been performed using the experimental data obtained by Caradonna and Tung in (1981). This test case is extensively used by the helicopter community for the validation of CFD codes applied to rotorcraft problems. The test cases range from simple, two-bladed, non-lifting rotors of simple plan-form, to lifting cases with high tip Mach numbers.

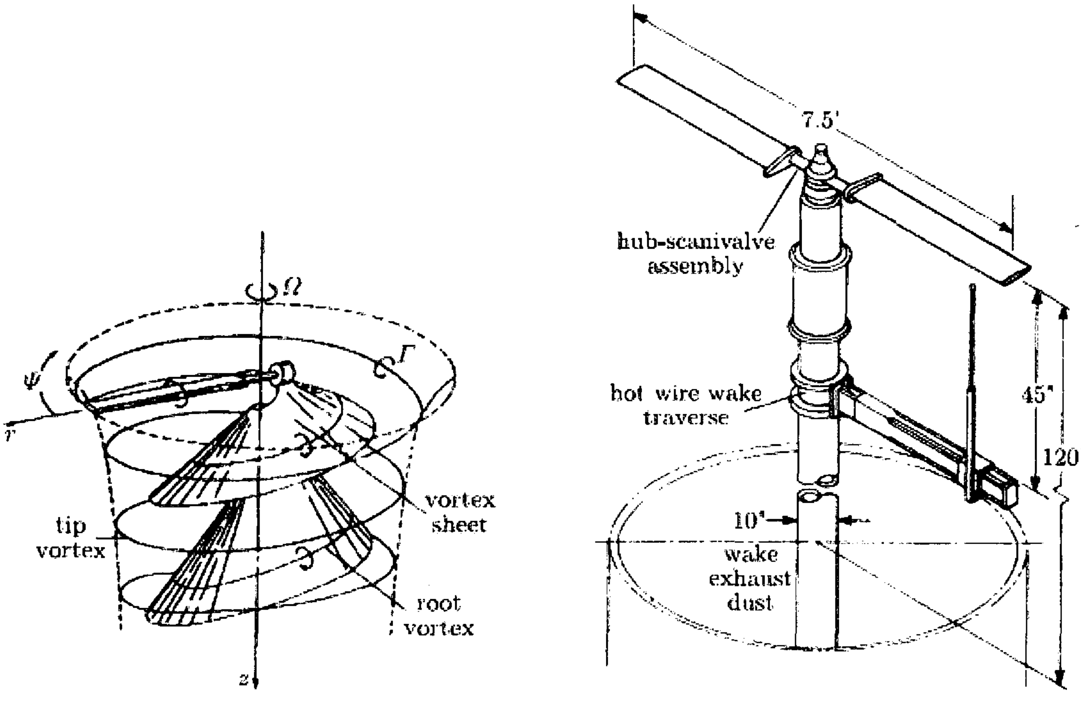

(a)

(b)

Figure 5.1: (a) Wake of a single rotor blade, (b) Experimental set-up of Caradonna-Tung two-bladed model rotor in hover.

Caradonna and Tung (1981) carried out an experimental and analytical study of a model helicopter rotor in hover. The experimental study involved simultaneous blade pressure measurements and tip vortex surveys. The model rotor consists of two rectangular, untwisted and untapered NACA-0012 rigid blades mounted on a tall column containing a drive shaft located in a large chamber with special ducting designed to eliminate room recirculation (Figure 5.1.b). The rotor aspect ratio, defined as the ratio of rotor radius and blade chord was six. The model rotor for CFD simulations had a diameter of 2.286 m, and a chord length of 0.191 m. The computational model utilizes flat tip surfaces and sharp trailing edges for all blades.

A large set of test conditions has been applied with the tip Mach number ranging from M_{tip}=0.226 to M_{tip}=0.890 and the collective pitch setting of $\theta=0^\circ$ to 12° at ambient conditions. Pressure distributions have been measured at five span wise cross-sections (r/R=0:50, 0.68, 0.80, 0.89 and 0.96) of the blade and tip vortex trajectory has been extracted using a hotwire technique. The modeled geometry of the Caradonna-Tung rotor is shown in Figure 5.2.

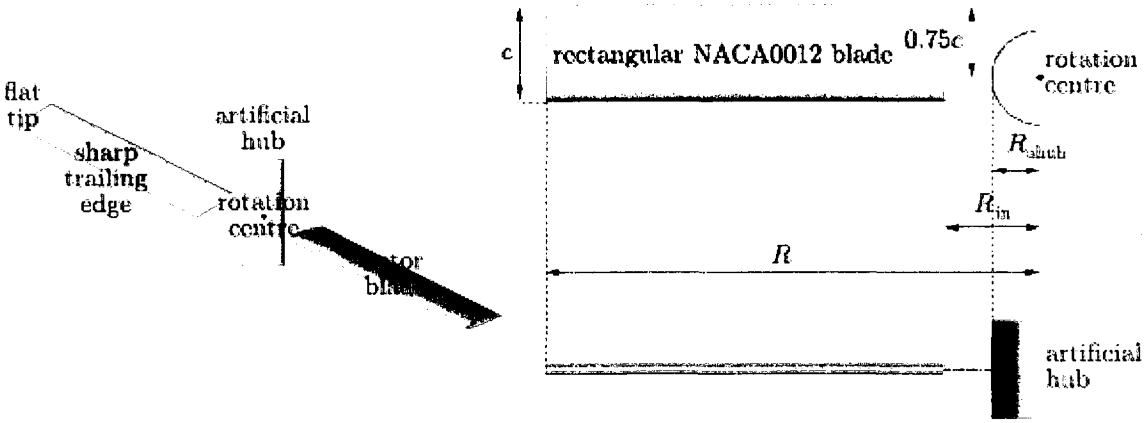

(a) (b)

Figure 5.2: (a) Geometry of Caradonna-Tung rotor ($\alpha=8^\circ$), (b) Caradonna-Tung rotor blade dimensions ($\alpha=0^\circ$, AR=6, $R_{ahub}=0.5c$, $R_{in}=c$, $R=6c$).

5.2 COMPUTATIONAL DOMAIN AND GRID TOPOLOGY

Grid generation is often considered as the most important and most time-consuming part of any CFD simulation. The quality of the grid plays a direct role on the quality of the analysis, regardless of the flow solver that is used. Additionally, the solver will be more robust and efficient when using a well constructed mesh. It is important for the CFD analyst to know and understand all of the various grid generation methods. Only by knowing all the methods can the user select the right tool to solve the problem at hand.

Structured grid methods take their name from the fact that the grid is laid out in a regular repeating pattern called a block. These types of grids utilize quadrilateral elements in 2D and hexahedral elements in 3D in a computationally rectangular array. Although the element topology is fixed, the grid can be shaped to be body fitted through stretching and twisting of the block. Really good structured grid generators utilize sophisticated elliptic equations to automatically optimize the shape of the mesh for orthogonality and uniformity.

It used to be that structured meshes could only consist of one block. The user was forced to make due with just one block and various cell flagging schemes were used to "turn off" portions of the block to model obstructions. Later, multiblock structured grid generation schemes were developed which allow several blocks to be connected together to construct the whole domain. Over the years, several block to block connection methods have evolved. These include: 1) point to point, where the blocks must match topologically and physically at the boundary; 2) many points to one point, where the blocks must be topologically similar but not the same at the boundary; and 3) arbitrary connections, where the blocks must be physically similar at the boundary, but can have significant topological differences. While multiblock grids give the user more freedom in constructing the mesh, the block connection requirements can be restricting and are often difficult to construct. Additionally, the various degrees of block connectivity freedom come at the expense of solution accuracy and solver robustness.

There is domain decomposition method which seeks to avoid the problems associated with block connections. Overset grid methods allow the individual blocks to conform to the physical boundaries, but be free form and overlapping at the block connections (Baysal et al., 1991). Sophisticated post-processing programs are run on the overlapping mesh to determine "hole cutting" locations and interpolation factors around block boundaries. What these methods gain in user convenience, they usually give up in solution accuracy. However, these methods can be enablers for geometries which would be too daunting a task with conventional methods (modeling helicopters with moving rotor blades and aircraft store separation are cases in point).

Structured grids enjoy a considerable advantage over other grid methods in that they allow the user a high degree of control. Because the user places control points and edges interactively, he has total freedom when positioning the mesh. In addition, hexahedral and quadrilateral elements, which are very efficient at filling space, support a high amount of skewness and stretching before the solution is significantly affected. This allows the user to naturally condense points in regions of high gradients in the flow field and expand out to a less dense packing away from these areas. Also, because the user interactively lays out the elements, the grid is most often flow-aligned, thereby yielding greater accuracy within the solver. Structured block-flow solvers typically require the lowest amount of memory for a given mesh size and execute faster because they are optimized for the grid's structured layout. Lastly, post processing of the results on a structured block grid is typically a much easier task because the logical grid planes make excellent reference points for examining the flowfield and for plotting the results.

The major drawback of structured block grids is the time and expertise required to lay out an optimal block structure for an entire model. Often this comes down to past user experience and brute force placement of control points and edges. Some geometries, e.g. shallow cones and wedges, do not lend themselves to structured block topologies. In these areas, the user is forced to stretch or twist the elements to a degree which drastically affects solver accuracy and performance. Grid generation times are usually measured in days if not weeks.

Unstructured grid methods utilize an arbitrary collection of elements to fill the domain. Because the arrangement of elements has no discernible pattern, the mesh is called unstructured (Singh at al.,1995). These types of grids typically utilize triangles in 2D and tetrahedral in 3D. While there are some codes which can generate unstructured quadrilateral elements in 2D, there are currently no production codes which can generate unstructured hexahedral elements in 3D.

As with structured grids, the elements can be stretched and twisted to fit the domain. These methods have the ability to be automated to a large degree. Given a good CAD model, a good mesh generator can automatically place triangles on the surfaces and tetrahedral in the volume with very little input from the user. The automatic meshing algorithm typically involves meshing the boundary and then either adding elements that touch the boundary (advancing front) or adding points in the interior and reconnecting the elements (Delaunay).

The advantage of unstructured grid methods is that they are very automated and, therefore, require little user time or effort. The user need not worry about laying out block structure or connections. Additionally, unstructured grid methods are well suited to inexperienced users because they require little user input and will generate a valid mesh under most circumstances. Unstructured methods also enable the solution of very large and detailed problems in a relatively short period of time. Grid generation times are usually measured in minutes or hours.

The major drawback of unstructured grids is the lack of user control when laying out the mesh. Typically any user involvement is limited to the boundaries of the mesh with the mesh generator automatically filling the interior. Triangle and tetrahedral elements are problematic in that they do not stretch or twist well, therefore, the grid is limited to being largely isotropic, i.e. all the elements have roughly the same size and shape. This is a major problem when trying to refine the grid in a local area, often the entire grid must be made much finer in order to get the point densities required locally. Another drawback of the methods is their reliance on good CAD data. Most meshing failures are due to some (possibly minuscule) error in the CAD model. Unstructured flow solvers typically require more memory and have longer execution times than structured grid solvers on a similar mesh. Post processing the solution on an unstructured mesh requires powerful tools for interpolating the results onto planes and surfaces of rotation for easier viewing.

In order to compute the flow field around Caradonna–Tung rotor and to perform a validation study, different types of grids have been generated and utilized. In the beginning of the analyses, simulations have been carried out by employing unstructured grids. For this purpose, unstructured grids with different volume cell numbers changing from 1 million to 6 million have been tested. However, it was observed that pressure contours on the rotor upper and lower surfaces were not regular. It was concluded that unstructured grids used in computations were not eligible for computing flow properties near solid boundaries where flow field gradients are high.

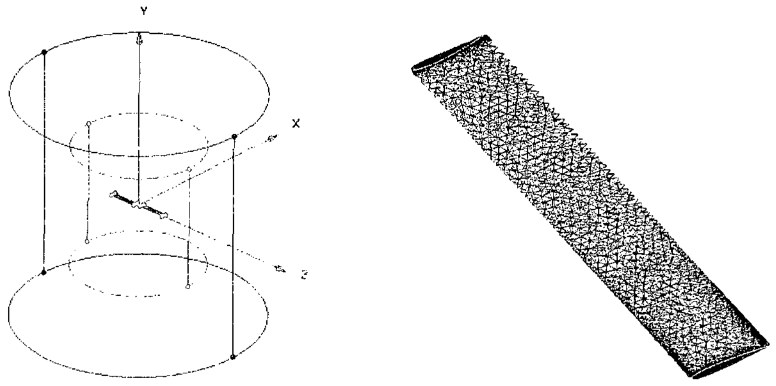

(a) (b)

Figure 5.3: (a) Inner and outer blocks of unstructured computational mesh, (b) Triangular surface mesh on the blade.

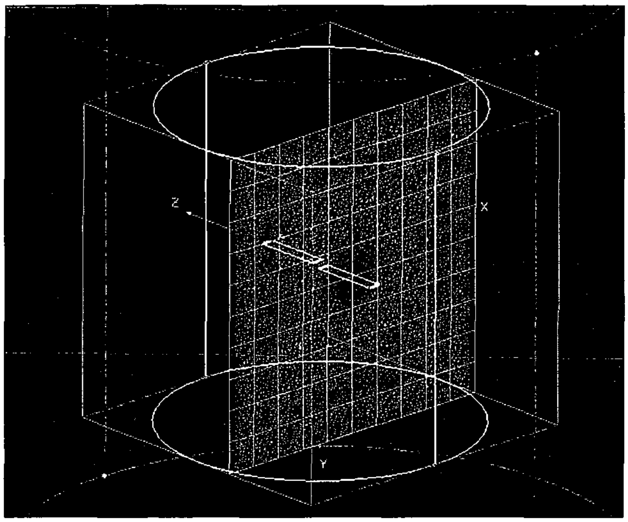

Figure 5.4: Topology of unstructured mesh for Caradonna–Tung rotor.

Hybrid grid methods are designed to take advantage of the positive aspects of both structured and unstructured grids. Hybrid grids utilize some form of structured grid in local regions while using unstructured grid in the bulk of the domain.

Hybrid grids can contain hexahedral, tetrahedral, prismatic, and pyramid elements in 3D and triangles and quadrilaterals in 2D. The various elements are used according to their strengths and weaknesses. Hexahedral elements are excellent near solid boundaries (where flow field gradients are high) and afford the user a high degree of control, but are time-consuming to generate. Prismatic elements (usually triangles extruded into wedges) are useful for resolving near wall gradients, but suffer from the fact that they are difficult to cluster in the lateral direction due to the underlying triangular structure. In almost all cases, tetrahedral elements are used to fill the remaining volume. Pyramid elements are used to transition from hexahedral elements to tetrahedral elements. Many codes try to automate the generation of prismatic meshes by allowing the user to define the surface mesh and then marching off the surface to create the 3D elements. While very useful and effective for smooth shapes, the extrusion process can break down near regions of high curvature or sharp discontinuities.

Another type of hybrid grid is the quasi-structured or "cooper" grid method. While basically a form of the prismatic grid extrusion technique, the quasi-structured method allows for some sophisticated forms of growing the 3D mesh using a sweeping concept within a CAD solid model.

The advantage of hybrid grid methods is that you can utilize the positive properties of structured grid elements in the regions which need them the most and use automated unstructured grid techniques where not much is happening in the flow field. The ability to control the shape and distribution of the grid locally is a powerful tool which can yield excellent meshes.

The disadvantage of hybrid methods is that they can be difficult to use and require user expertise in laying out the various structured grid locations and properties to get the best results. Hybrid methods are typically less robust than unstructured methods. The generation of the structured portions of the mesh will often fail due to complex geometry or user input errors. While the flow solver will use more resources than a structured block code, it should be very similar to an unstructured code. Post processing the flow field solution on a hybrid grid suffers from the same disadvantages as an unstructured grid. The time required for grid generation is usually measured in hours or days.

After having unsatisfactory results by using unstructured grids, hybrid grid technique has been utilized for generation of computational mesh. Firstly, a structured mesh block consists of hexahedral cells around the rotor has been created. The structured block is H-type in stream wise and span wise directions while it is O-type in normal direction. There are 41x41x41 grid points in stream wise, span wise and normal directions, respectively. Then, the rest of the domain has been filled with tetrahedral, prismatic, and pyramid elements. The hybrid mesh consists of 288,000 hexahedral and 990,704 mixed cells. Details of computational mesh are displayed in Figures 5.5-5.11.

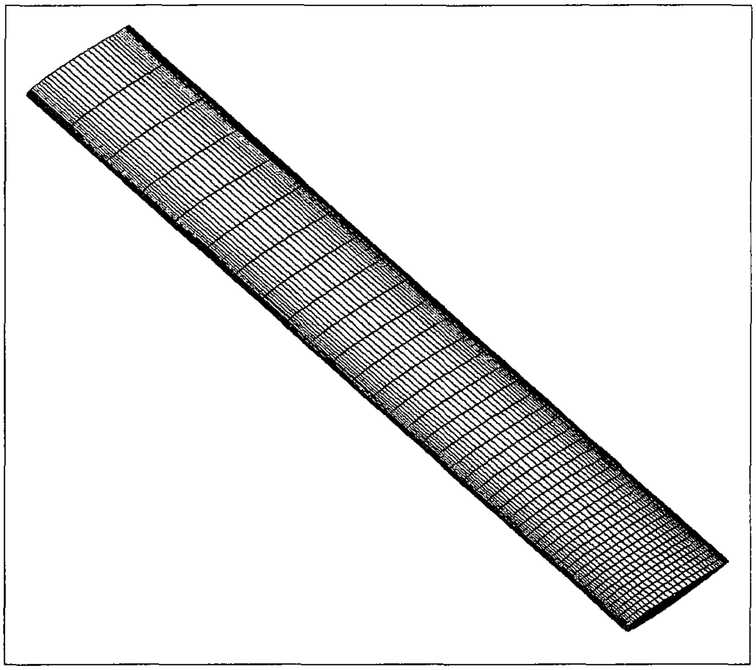

Figure 5.5: Grid points on the modeled blade surface.

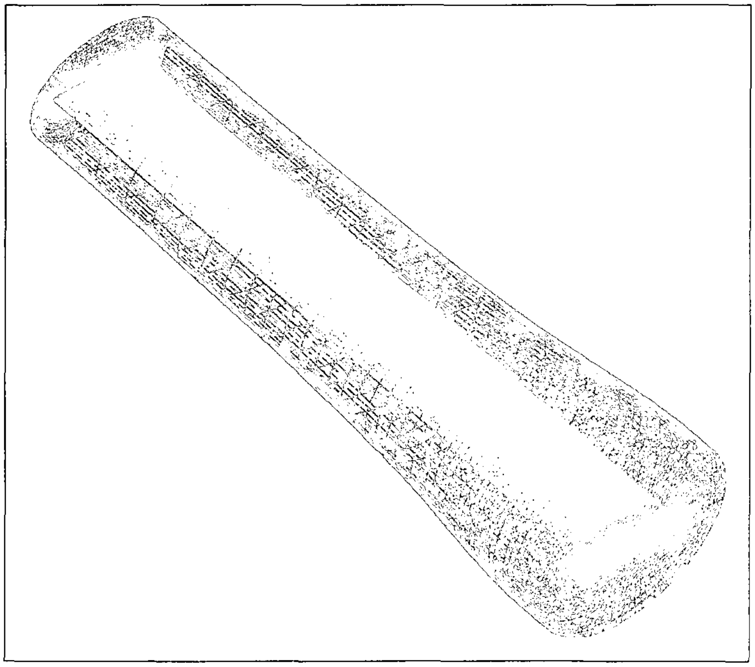

Figure 5.6: Structured block around Caradonna–Tung rotor blade.

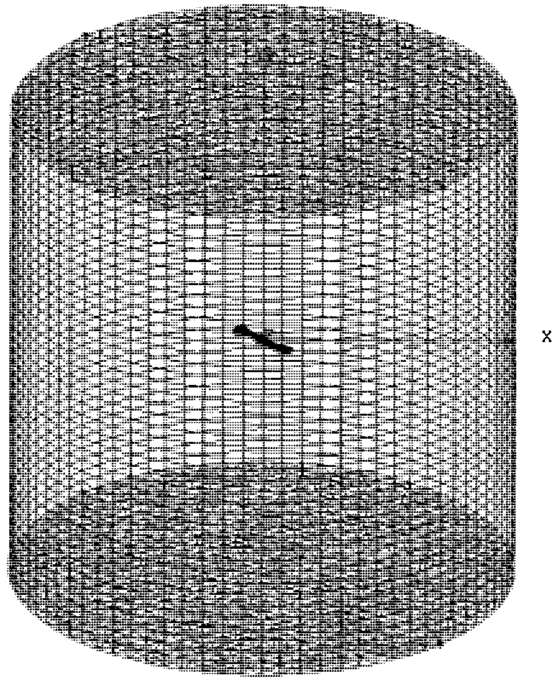

Figure 5.7: Hybrid block around Caradonna–Tung rotor.

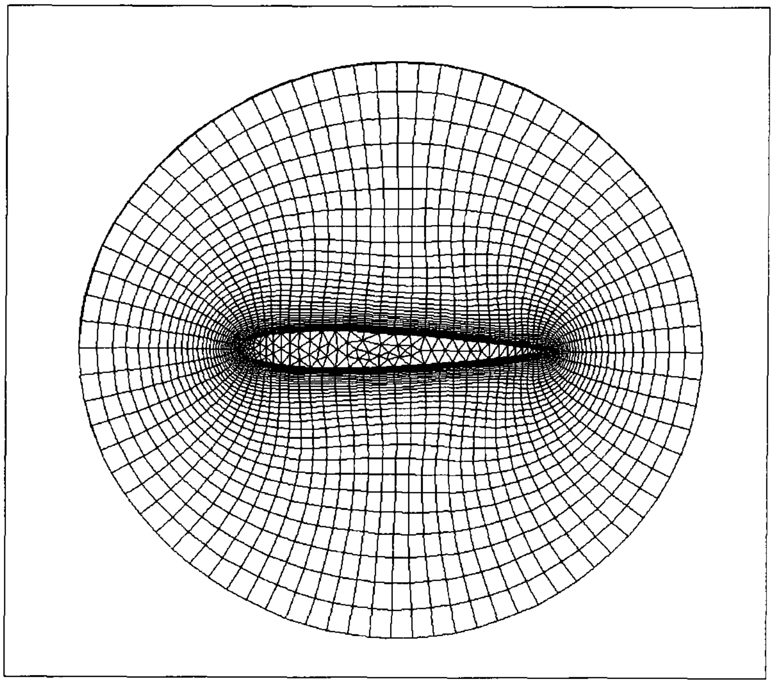

Fig.5.8: Cross section of the structured block in span wise direction.

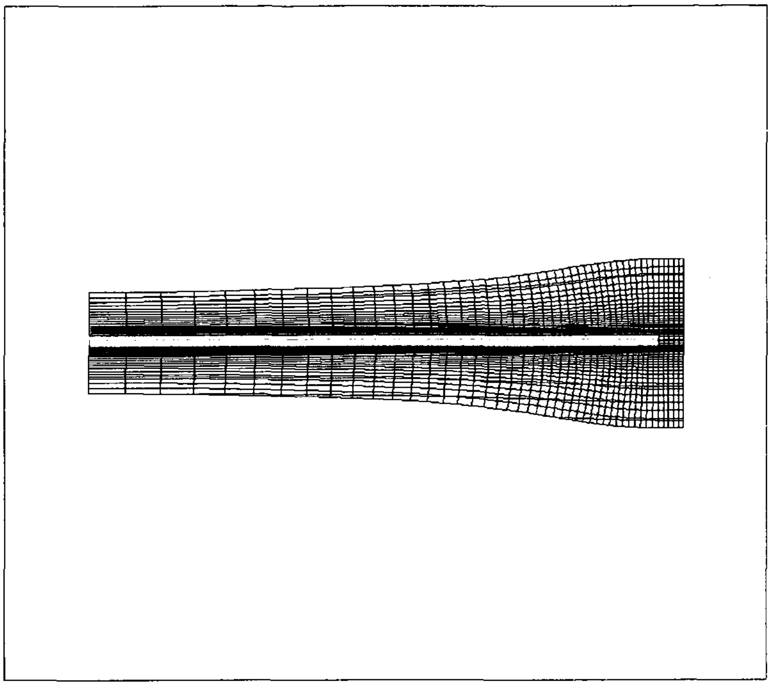

Figure 5.9: Cross section of structured block in stream wise direction.

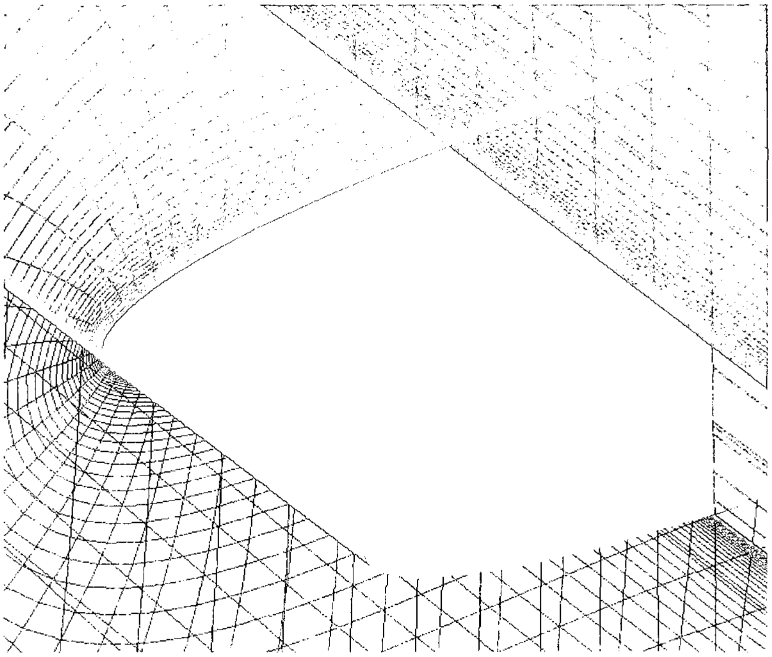

Figure 5.10: Mesh topology near tip region.

5.3 NUMERICAL METHOD OF SOLUTION

The present investigation incorporated in its toolkit is a commercially available solver, FLUENT. This code solves numerically the compressible, mass-weighted, Reynolds-averaged Navier-Stokes (RANS) equations with several turbulence models. The results have been obtained by running the code on the UNIX clusters (Wilbur and Zorka) located at Old Dominion University. In order to reduce the computational efforts, parallel processing has been utilized, where the data communication has been achieved via MPI (Message Passage Interface) libraries.

The present simulations have been performed by employing unsteady, density-based solver with implicit dual-time-stepping scheme (2nd order of accuracy). The third order MUSCL (Monotone Upstream-Centered Schemes for Conservation Laws) scheme has been applied for spatial discretization. This third-order convection scheme was conceived from the original by blending a central differencing scheme and second-order upwind scheme. Compared to the second-order upwind scheme, the third-order MUSCL has a potential to improve spatial accuracy for all types of meshes by reducing numerical diffusion, most significantly for complex three-dimensional flows, and it is available for all transport equations. Courant number has been ramped up to five. The solver provides an efficient Moving Mesh technique. The mesh has been rotated with an angular velocity which corresponds to the tip Mach number, M_{tip}, encountered for a given case. A uniform computational time step of $\delta t=1x10^{-5}$ (e.g., 473 steps for 1 revolution, $\Omega=132.9$ rad/s) has been used in the validation simulations.

5.4 NON–LIFTING CASE

For the non–lifting cases, computations have been performed by setting the angular velocity to 132.9 rad/s, which corresponds to a tip Mach number, M_{tip}=0.52 and a rotor tip velocity, U_{tip} =176.8 m/s.

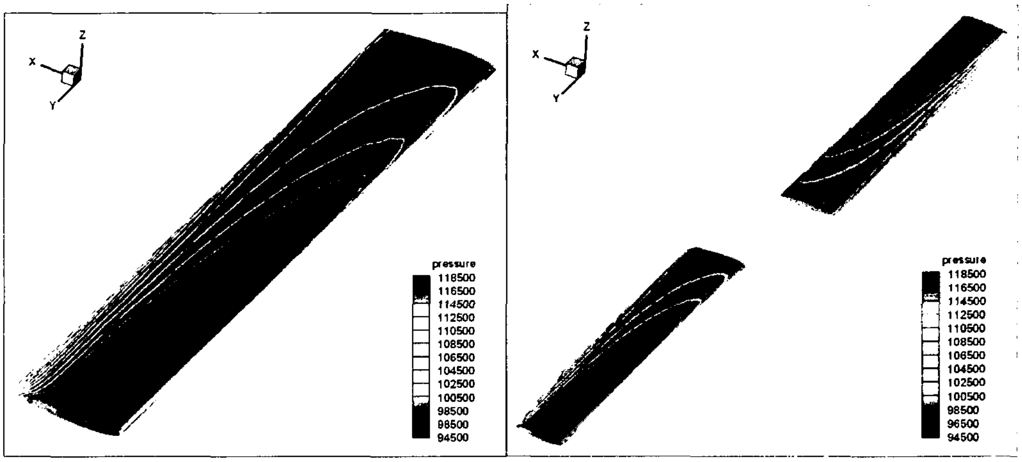

Figure 5.11: Pressure contours on the blade and the rotor surfaces, inviscid, hover, M_{tip}=0.52, Ω=132.9 rad/s, α=0°,Re=2.47x10^6

The collective pitch angle has been set to 0°. The inviscid and laminar solutions have been obtained in order to compare with the experimental data.

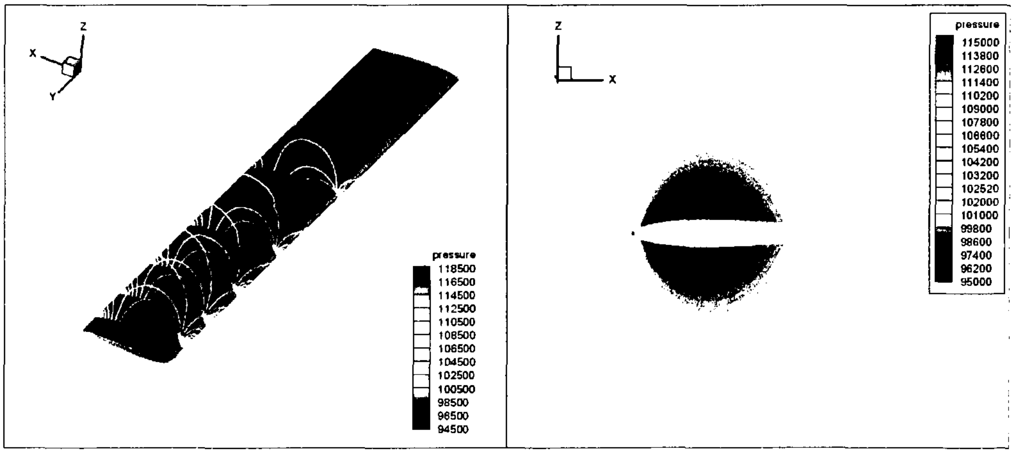

(a) **(b)**

Figure 5.12: (a) Pressure contours at five stations (r/R=0.5, 0.68, 0.80, 0.89 and 0.96) span wise stations, (b) Pressure contours at r/R=0.89, inviscid, hover, Ω=132.9 rad/s, M_{tip}=0.52, α=0°, Re=2.47×10^6

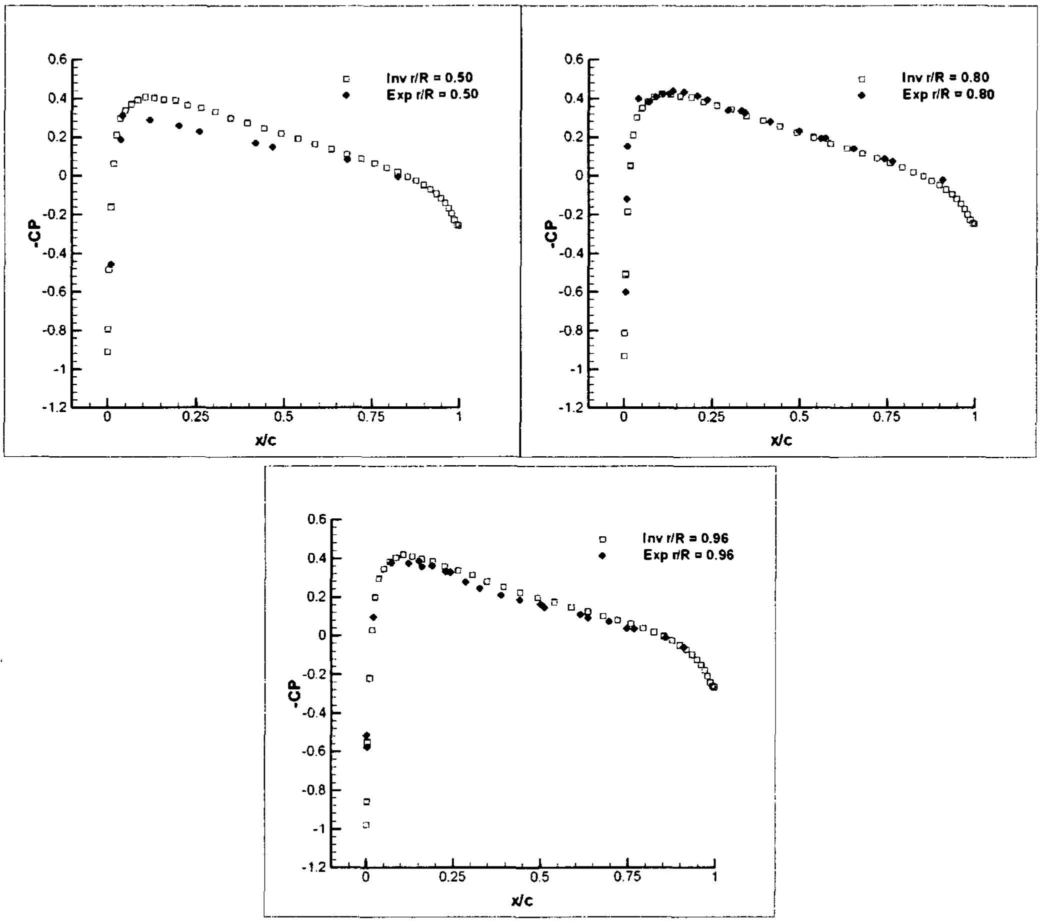

Figure 5.13: C_p distributions at three span wise locations (r/R=0.5, 0.80 and 0.96), inviscid, hover, α=0°, M_{tip}=0.52, Ω=132.9 rad/s, Re=2.47×10^6

A detailed insight into the flow behavior may be obtained by comparing the pressure coefficient, C_p distribution with the experimental data at three cross-sections along the span of the blade (r/R=0.5, 0.80 and 0.96), Figure 5.11. The overall agreement with experimental data is satisfactory. At r/R=0.50, numerical C_p values seem to be slightly lower than the corresponding experimental values. This difference may be result from using inviscid solver. The flow velocity is relatively low at this station. So, viscous effects are dominant with respect to the region where the flow velocity is high (e.g., tip region). At r/R = 0.80 and 0.96, experimental and numerical results are almost identical.

The next case is the laminar simulation of the hovering Caradonna–Tung rotor with an angular velocity Ω=132.9 rad/s which corresponds to a tip Mach number M_{tip}=0.52 and V_{tip}=176 m/s. Figure 5.14 displays the C_p values at different spanwise (r/R=0.5, 0.80 and 0.96) stations.

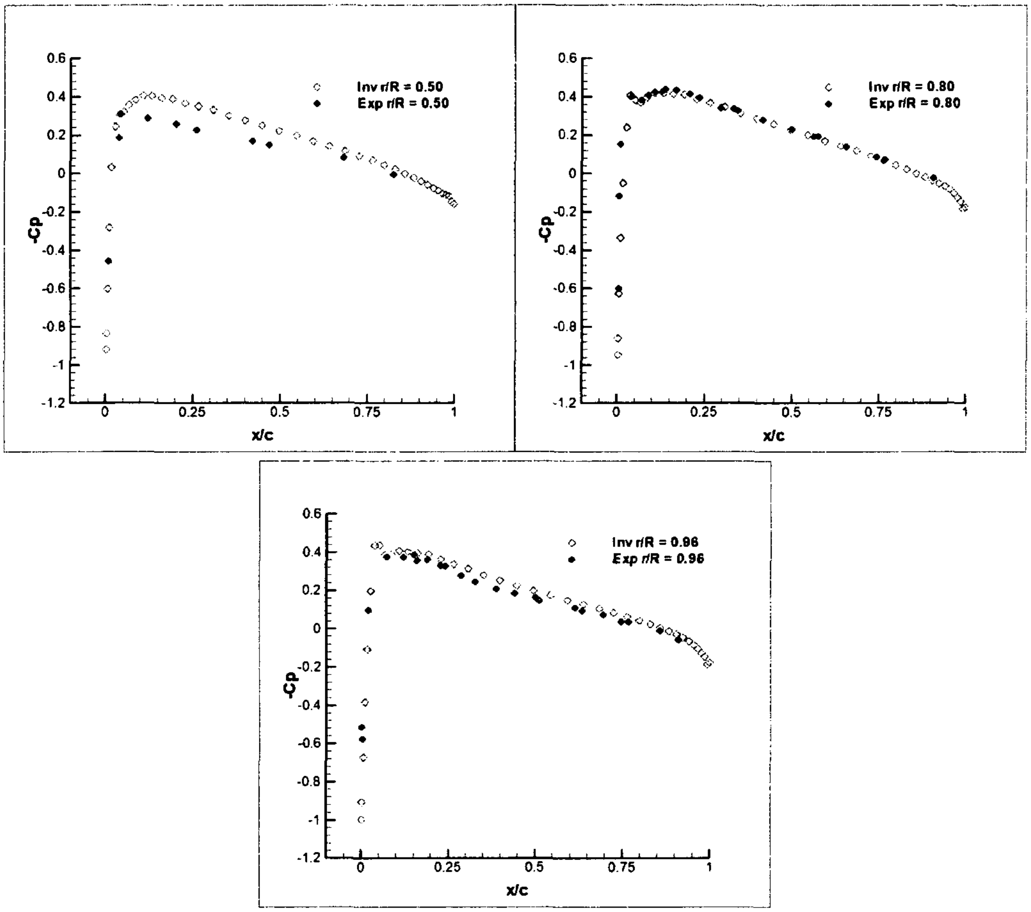

Figure 5.14: C_p distributions at three span wise locations (r/R=0.5, 0.80 and 0.96), laminar, hover, $\alpha=0^{\circ}$, $M_{tip}=0.52$, $\Omega=132.9$ rad/s, Re=2.47×10^{6}

The agreement between the experiments and the simulations remains excellent for the non–lifting inviscid and laminar simulations. There is no significant difference between the computed values and experimental data.

5.5 LIFTING CASES

For the lifting cases, collective pitch angle has been set to 8°. The simulations have been performed for a subsonic tip Mach number, M_{tip}=0.439 (Ω=112.2 rad/s, U_{tip}=149.26 m/s) and a transonic tip Mach number, M_{tip}=0.877 (Ω=224.2 rad/s, U_{tip}=298.2 m/s)

5.5.1 M_{tip}=0.439 CASE

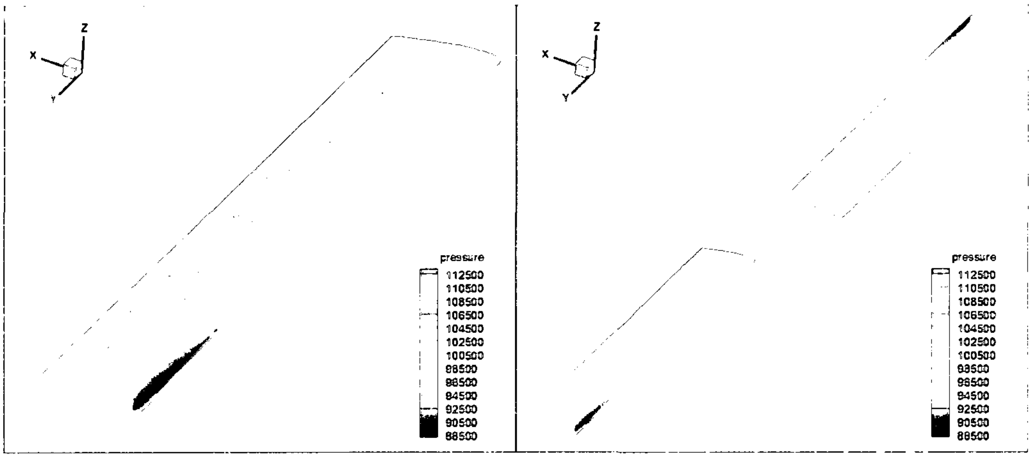

Figure 5.15: Pressure contours on the blade and the rotor surfaces, inviscid, lifting, M_{tip}=0.439, Ω=112.2 rad/s, α=8°, Re=2.11x10^6

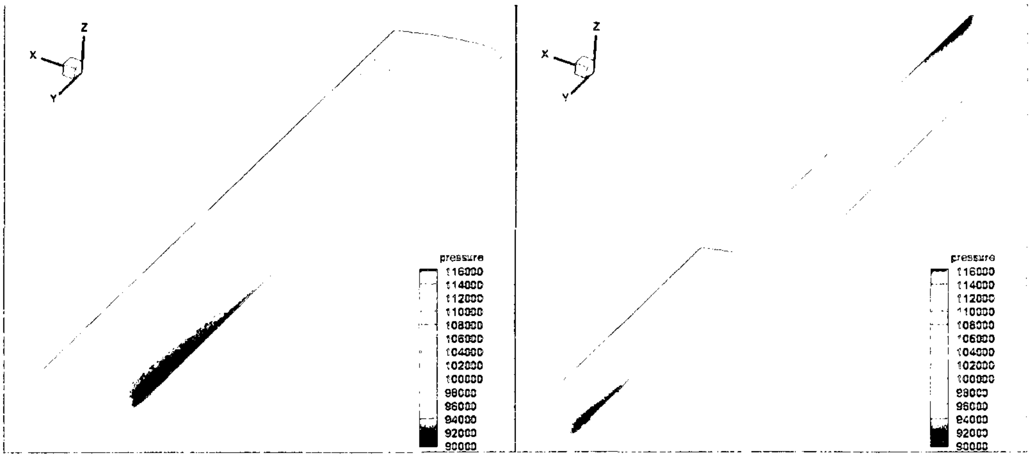

Figure 5.16: Pressure contours on the blade and the rotor surfaces, laminar, lifting, M_{tip}=0.439, Ω=112.2 rad/s, α=8°, Re=2.11x10^6

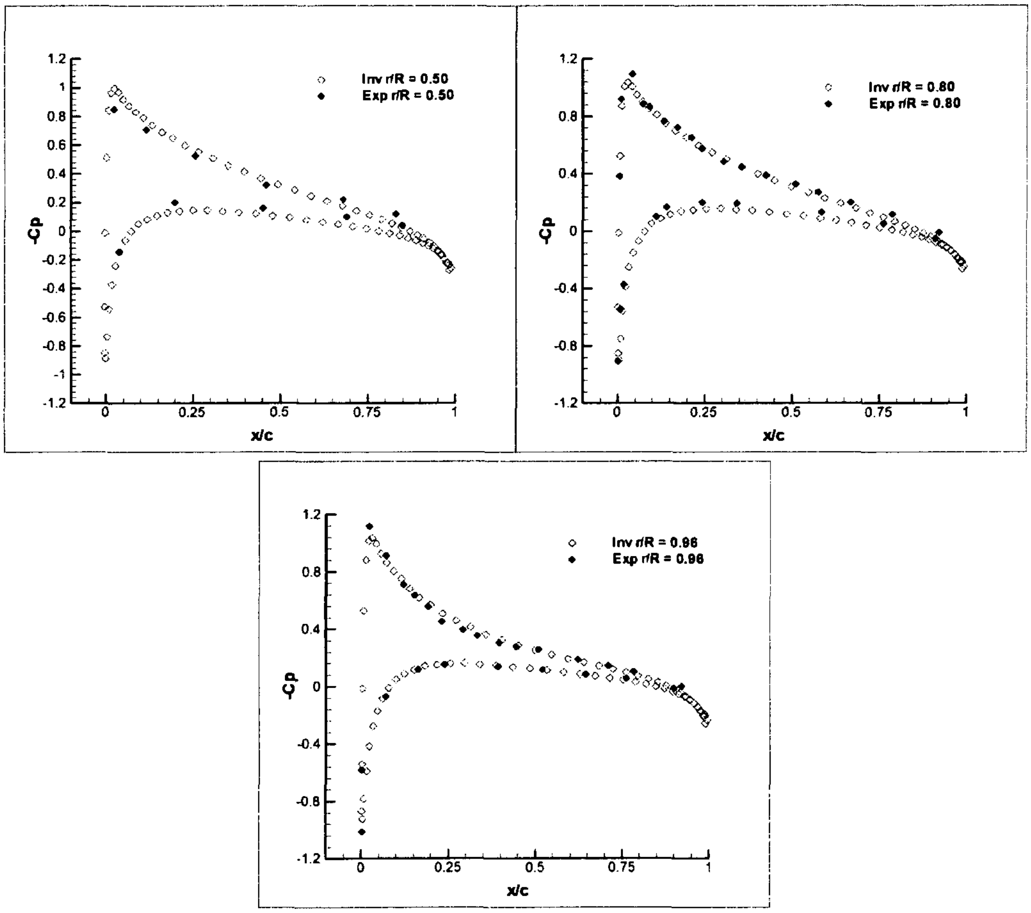

Figure 5.17: C_p distributions at three span wise locations (r/R=0.5, 0.80 and 0.96), inviscid, hover, α=0°, M_{tip}=0.439, Ω=112.2 rad/s, Re=2.11x10^6

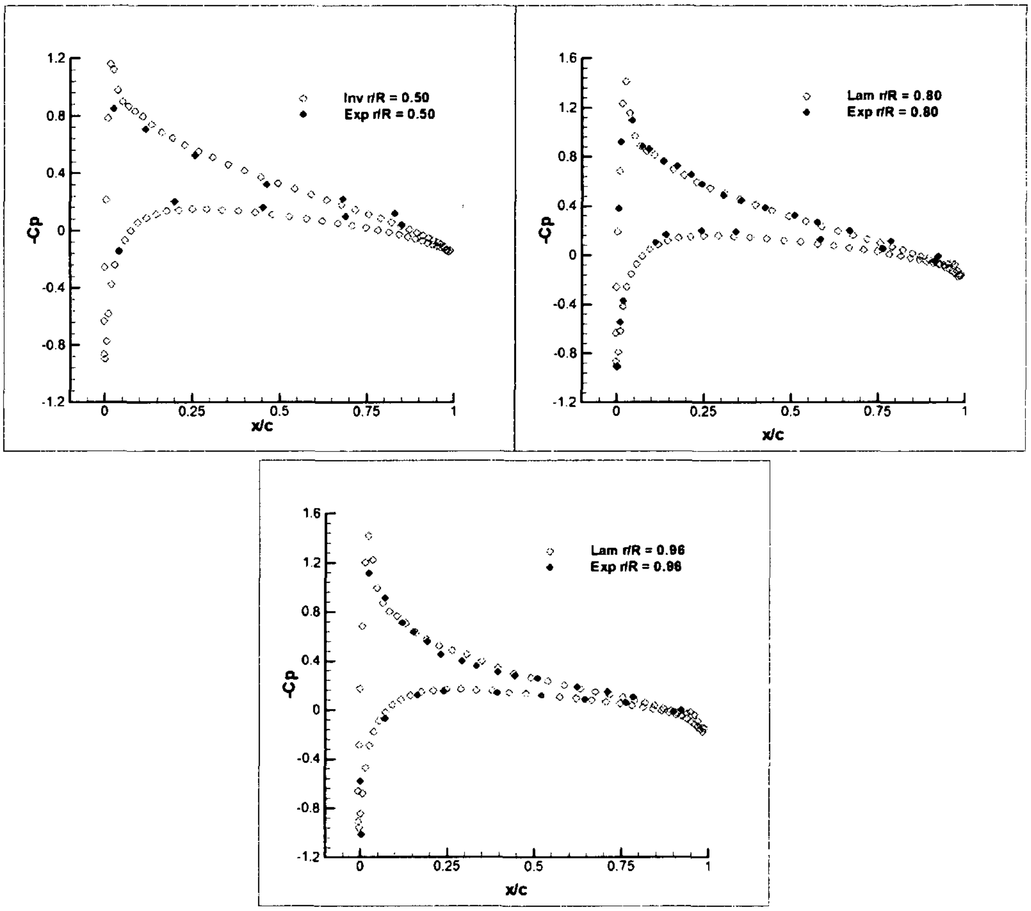

Figure 5.18: C_p distributions at three span wise locations (r/R=0.5, 0.80 and 0.96), laminar, hover, $\alpha=0^\circ$, $M_{tip}=0.439$, $\Omega=112.2$ rad/s, $Re=2.11\times10^6$

5.5.2 M_{tip}=0.877 CASE

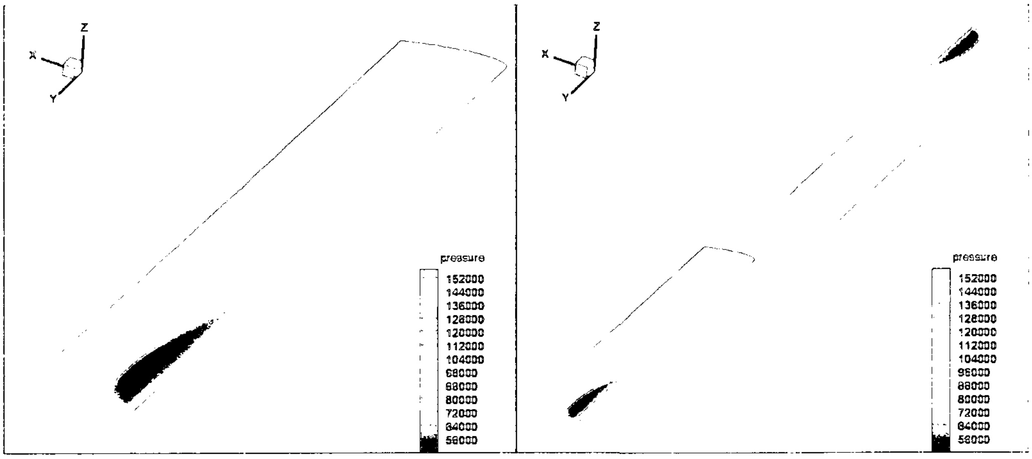

Figure 5.19: Pressure contours on the blade and the rotor surfaces, inviscid, lifting, M_{tip}=0.877, Ω=224.2 rad/s, α=8°, Re=4.22x10^6

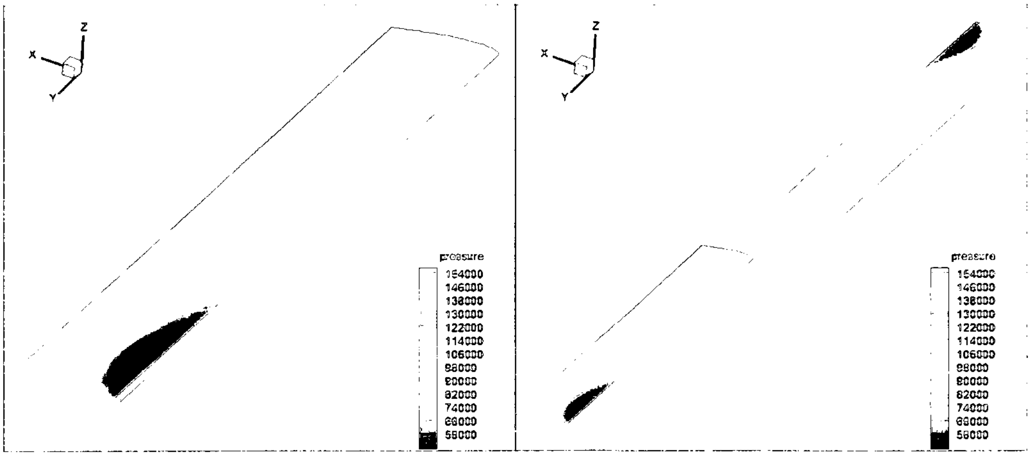

Figure 5.20: Pressure contours on the blade and the rotor surfaces, laminar, lifting, M_{tip}=0.877, Ω=224.2 rad/s, α=8°, Re=4.22x10^6

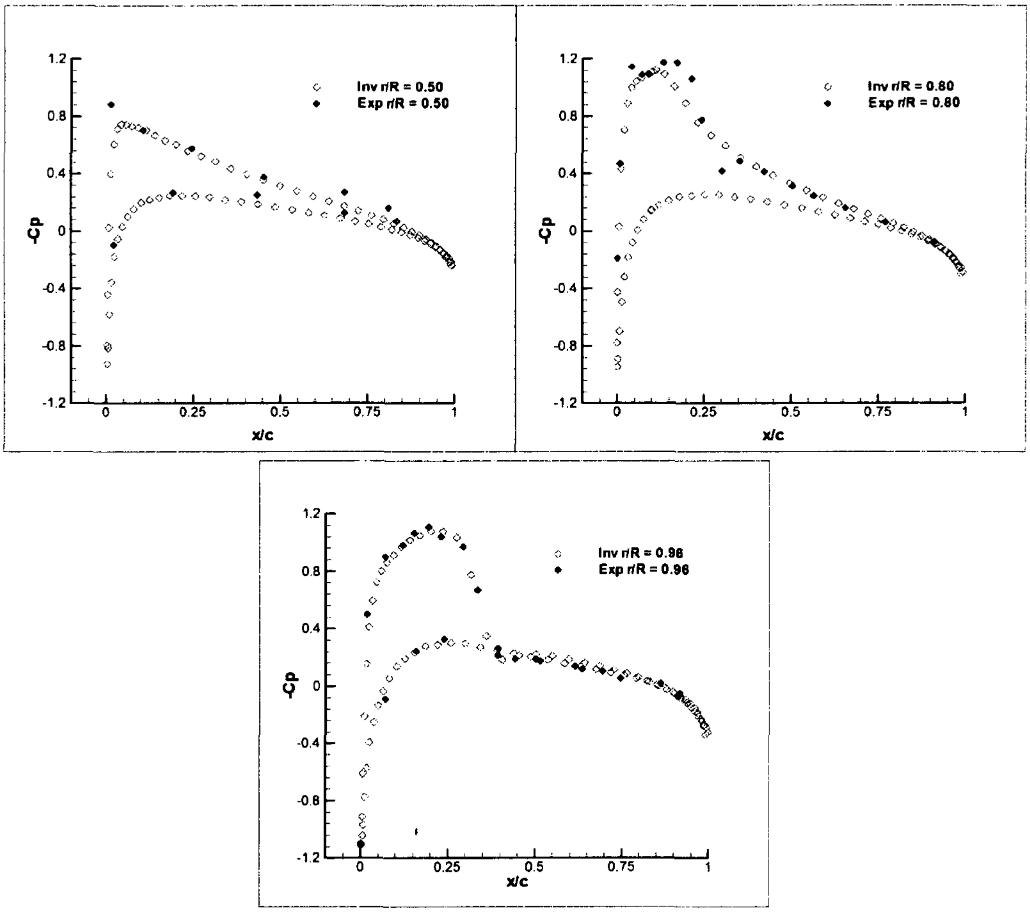

Figure 5.21: C_p distributions at 3 span wise locations (r/R=0.5, 0.80 and 0.96), inviscid, hover, α=8°, M_{tip}=0.877, Ω=224.2 rad/s, Re=4.22x10^6

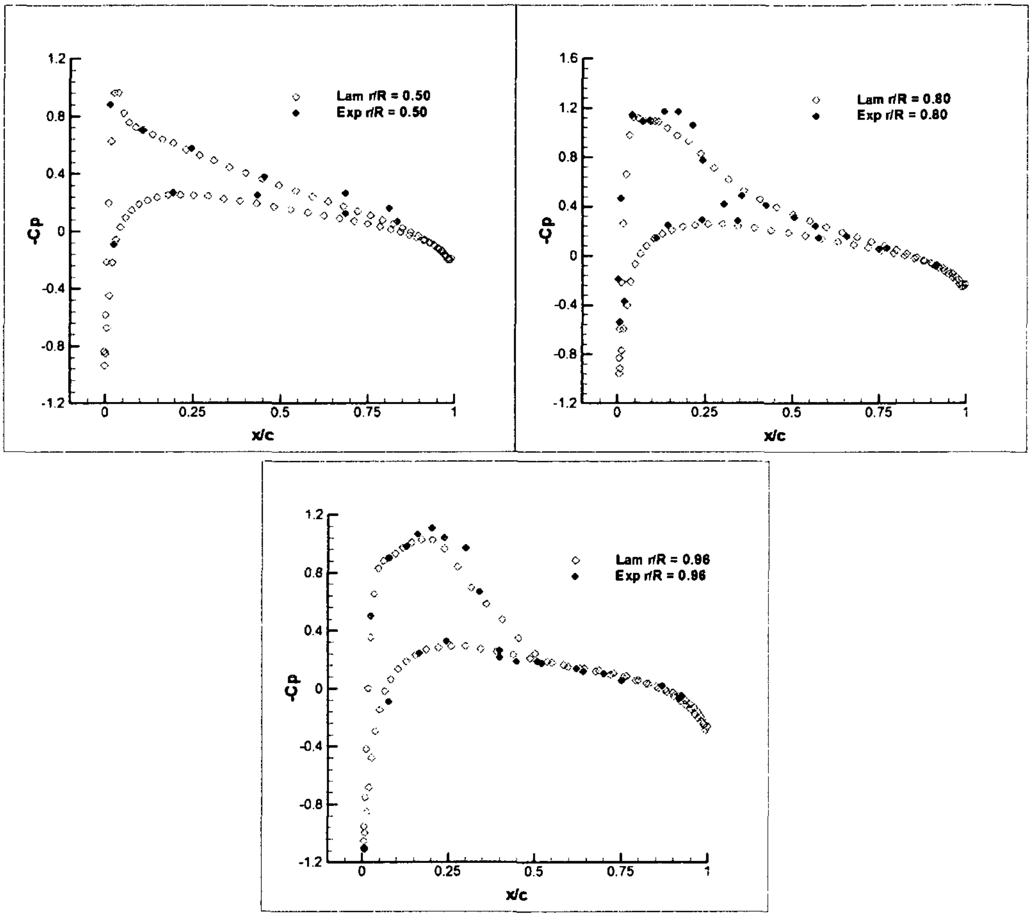

Figure 5.22: C_p distributions at 3 span wise locations (r/R=0.5, 0.80 and 0.96), laminar, hover, $\alpha=8^\circ$, $M_{tip}=0.877$, $\Omega=224.2$ rad/s, $Re=4.22\times10^6$

The figures demonstrate the good agreement obtained between the computed and measured surface pressure distributions. It is noteworthy that the shock location is predicted correctly in accordance with the measurements for all transonic cases. The overall agreement with the experimental data is satisfactory. Therefore, the methodology has been deemed as validated successfully and can now be used for more complex computations. In the next chapter, the results of a comparative study for several turbulence models, simulations for several NACA airfoil types ($\alpha=0^{\circ}$ and $\alpha=8^{\circ}$), a forward flight analysis for a single rotor configuration, forward flight analysis for a coaxial rotor configuration and an investigation of effect of Rotor Separation Distance on lift produced by coaxial rotors will be presented.

CHAPTER VI

RESULTS AND DISCUSSION

This chapter is broadly divided into three parts. In the first part, the output of a comparative study for several turbulence models provided by the solver is presented. Secondly, the results of the simulations for single (conventional) rotor configurations are presented. The last part addresses the methodology and the results for the unsteady, moving-mesh CFD simulations for coaxial helicopter rotors.

6.1 COMPARISON OF TURBULENCE MODELS

It is an unfortunate fact that no single turbulence model is universally accepted as being superior for all classes of problems. The choice of turbulence model will depend on considerations such as the physics encompassed in the flow, the established practice for a specific class of problem, the level of accuracy required, the available computational resources, and the amount of time available for the simulation. To make the most appropriate choice of model for a given application, one needs to understand the capabilities and limitations of the various options.

Therefore, several turbulence models have been utilized and tested for the simulation of a case where $\alpha=8^{\circ}$, $M_{tip}=0.877$. Results have been compared with experimental data. The aim is to investigate which turbulence model works best for the present helicopter simulations.

6.1.1 THE SPALART–ALLMARAS MODEL

The Spalart–Allmaras model is a relatively simple, one-equation model that solves a modeled transport equation for the kinematic eddy (turbulent) viscosity. This embodies a relatively new class of one-equation models in which it is not necessary to calculate a length scale related to the local shear layer thickness. The Spalart–Allmaras model was designed specifically for aerospace applications involving wall-bounded flows and has been shown to give good results for boundary layers subjected to adverse pressure gradients. It is also gaining popularity for turbo machinery applications.

In its original form, the Spalart–Allmaras model is effectively a low-Reynolds-number model, requiring the viscous-affected region of the boundary layer to be properly resolved. In the calculations, however, the Spalart–Allmaras model has been implemented to use wall functions when the mesh resolution is not sufficiently fine. This might make it the best choice for relatively crude simulations on coarse meshes where accurate turbulent flow computations are not critical. Furthermore, the near-wall gradients of the transported variable in the model are much smaller than the gradients of the transported variables in the k-ε or k-ω models. This might make the model less sensitive to numerical error when non–layered meshes are used near walls.

On a cautionary note, however, The Spalart–Allmaras model has no claim regarding its suitability to all types of complex engineering flows. For instance, it cannot be relied on to predict the decay of homogeneous, isotropic turbulence. Furthermore, one-equation models are often criticized for their inability to rapidly accommodate changes in length scale, as might be necessary when the flow changes abruptly from a wall-bounded to a free shear flow.

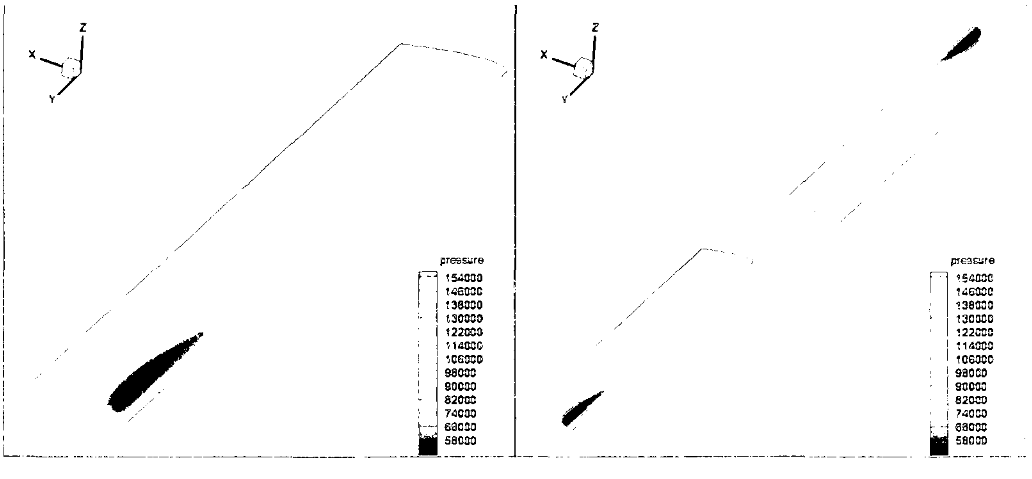

Figure 6.1: Pressure contours on the blade and the rotor surfaces, Spalart–Allmaras, lifting, M_{tip}=0.877, Ω=224.2 rad/s, α=8°, Re=4.22×10^6

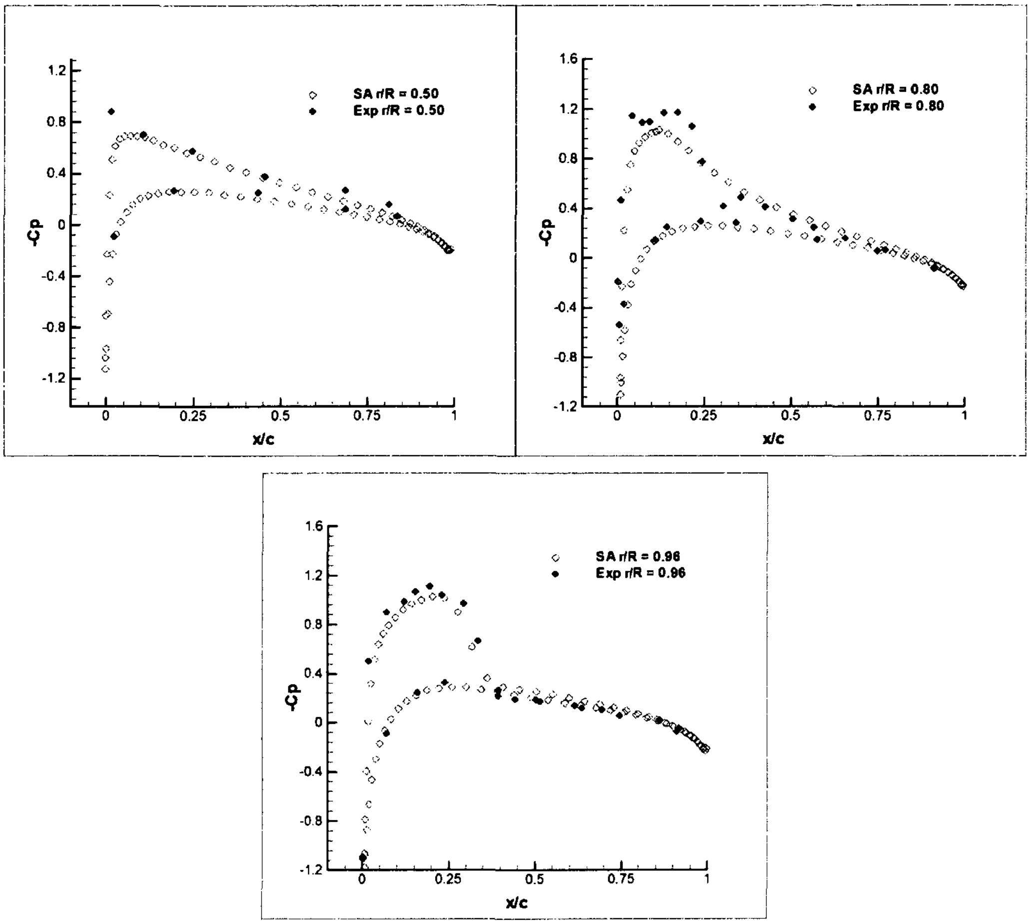

Figure 6.2: C_p distributions at three span wise locations (r/R=0.5, 0.80 and 0.96), Spalart–Allmaras, hover, α=8°, M_{tip}=0.877, Ω=224.2 rad/s, Re=4.22×10^6

6.1.2 THE STANDARD *k*–*ε* MODEL

The simplest "complete models" of turbulence are two-equation models in which the solution of two separate transport equations allows the turbulent velocity and length scales to be independently determined. The standard *k*–*ε* model falls within this class of turbulence model and has become the workhorse of practical engineering flow calculations in the time since it was proposed by Launder and Spalding. Robustness, economy, and reasonable accuracy for a wide range of turbulent flows explain its popularity in industrial flow and heat transfer simulations. It is a semi-empirical model, and the derivation of the model equations relies on phenomenological considerations and empiricism. As the strengths and weaknesses of the standard *k*–*ε* model have become known, improvements have been made to the model to improve its performance. The standard *k*–*ε* model is a semi-empirical model based on model transport equations for the turbulence kinetic energy (*k*) and its dissipation rate (*ε*). In the derivation of the *k*–*ε* model, the assumption is that the flow is fully turbulent, and the effects of molecular viscosity are negligible. The standard *k*–*ε* model is therefore valid only for fully turbulent flows.

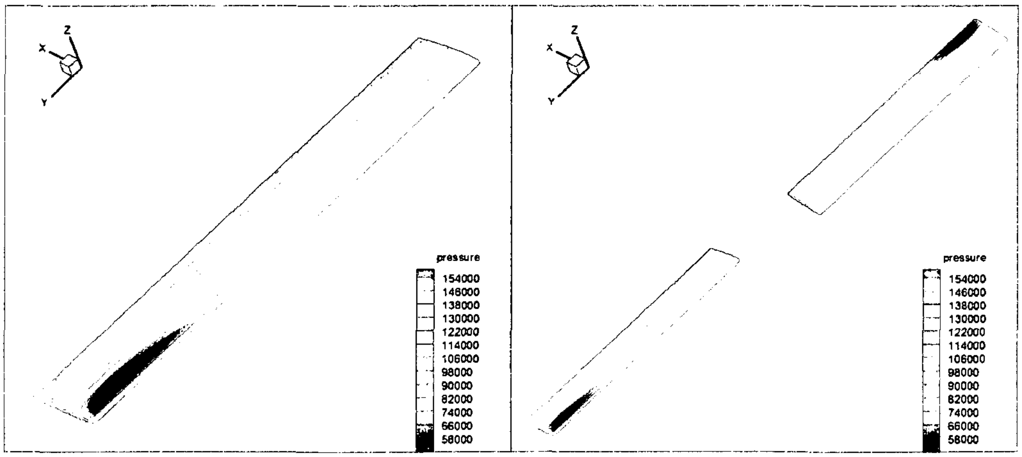

Figure 6.3: Pressure contours on the blade and the rotor surfaces. Standard *k*–*ε*, lifting, M_{tip}=0.877, Ω=224.2 rad/s, α=8°, Re=4.22x10^6

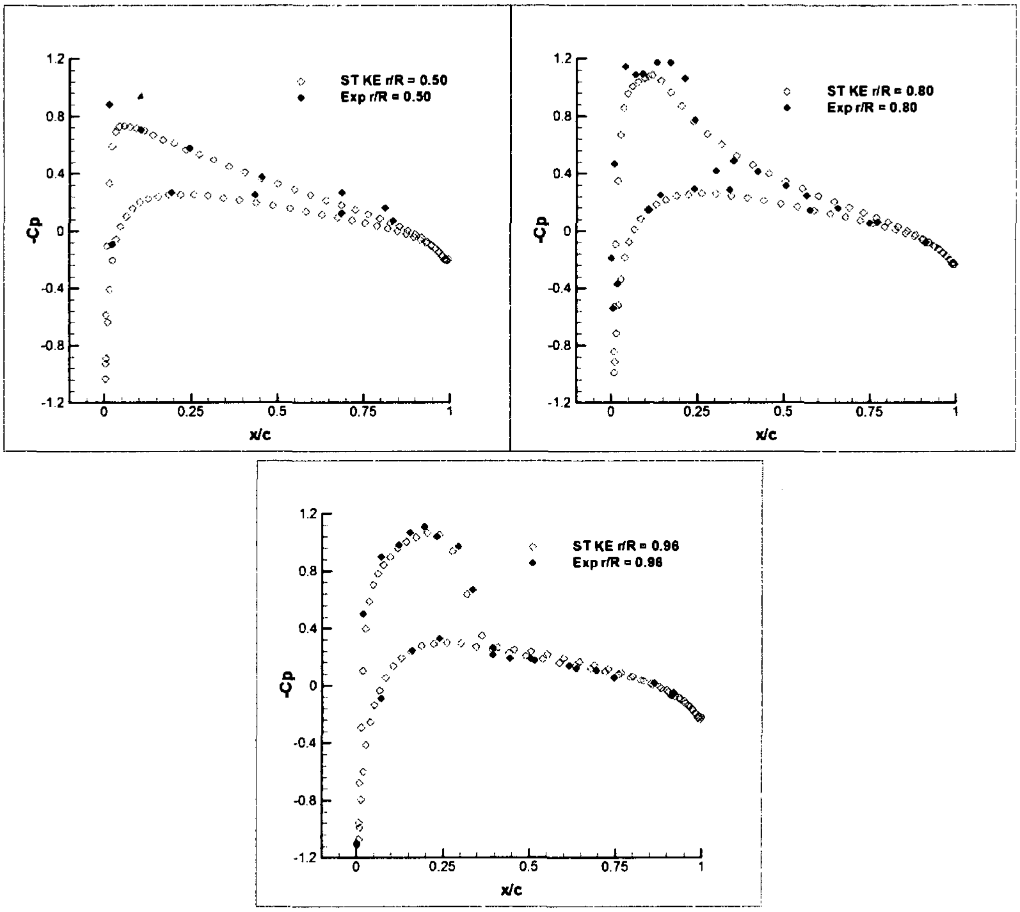

Figure 6.4: C_p distributions at three span wise locations (r/R=0.5, 0.80 and 0.96), Standard *k*–*ε*, hover, α=8°, M_{tip}=0.877, Ω=224.2 rad/s, Re=4.22x10^6

6.1.3 THE RNG *k–ε* MODEL

The RNG *k–ε* model was derived using a rigorous statistical technique (called renormalization group theory). It is similar in form to the standard *k–ε* model, but includes some refinements. The RNG model has an additional term in its *ε* equation that significantly improves the accuracy for rapidly strained flows. The effect of swirl on turbulence is included in the RNG model, enhancing accuracy for swirling flows. The RNG theory provides an analytical formula for turbulent Prandtl numbers, while the standard *k–ε* model uses user-specified, constant values. While the standard *k–ε* model is a high-Reynolds–number model, the RNG theory provides an analytically-derived differential formula for effective viscosity that accounts for low-Reynolds-number effects. Effective use of this feature does, however, depend on an appropriate treatment of the near-wall region. These features make the RNG *k–ε* model more accurate and reliable for a wider class of flows than the standard *k–ε* model. The RNG-based *k–ε* turbulence model is derived from the instantaneous Navier–Stokes equations, using a mathematical technique called "renormalization group" (RNG) methods. The analytical derivation results in a model with constants different from those in the standard *k–ε* model, and additional terms and functions in the transport equations for *k* and *ε*.

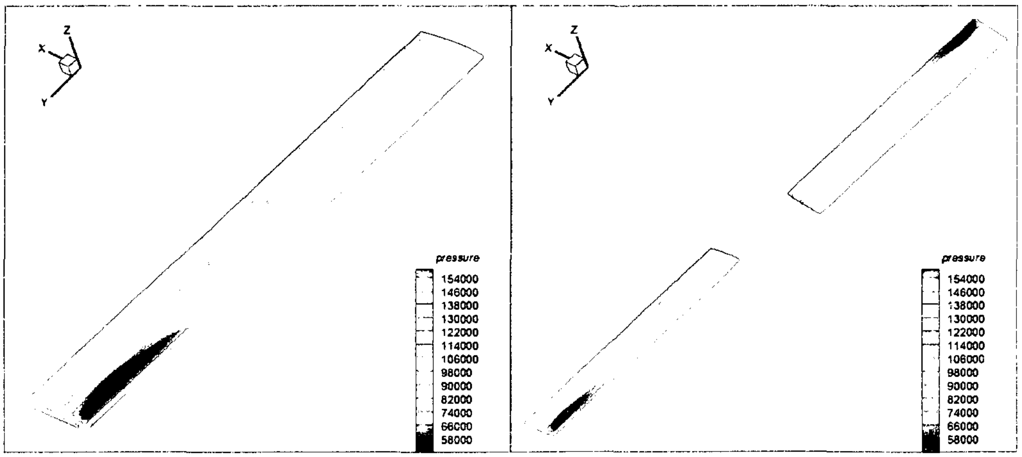

Figure 6.5: Pressure contours on the blade and the rotor surfaces, RNG k–ε, lifting, M_{tip}=0.877, Ω=224.2 rad/s, α=8°, Re=4.22x10^6

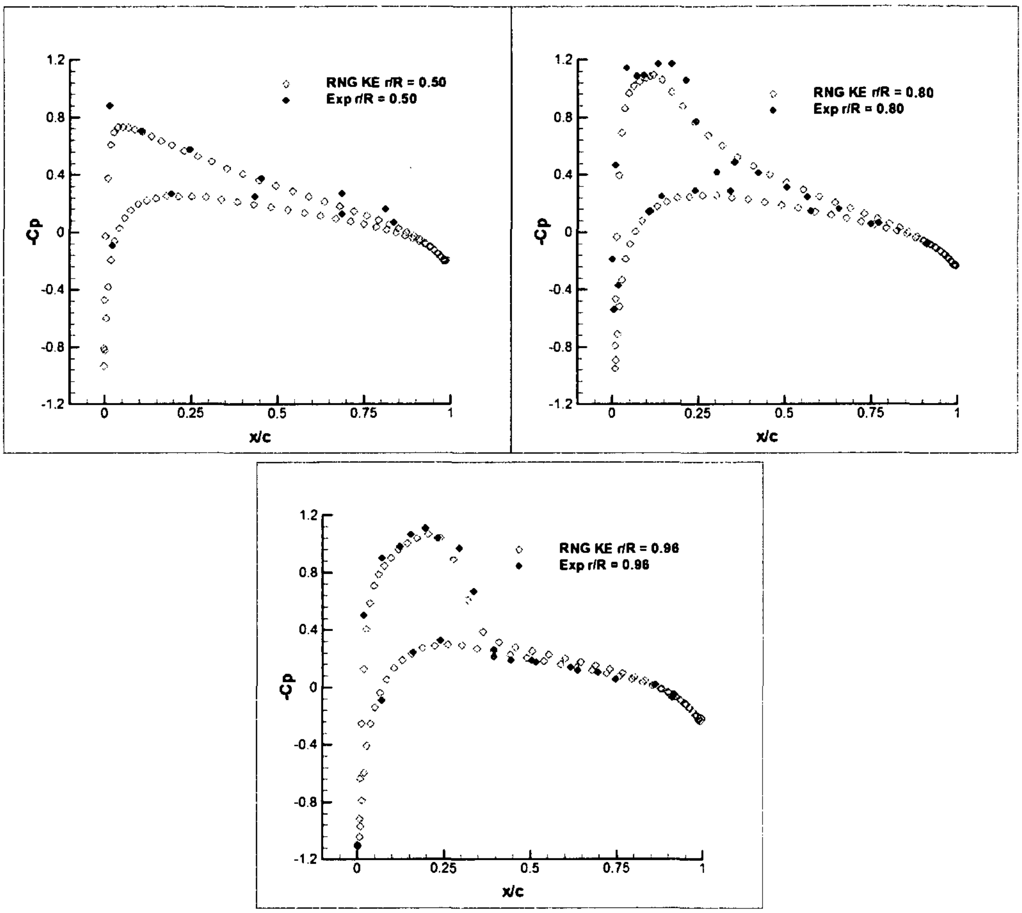

Figure 6.6: C_p distributions at three span wise locations (r/R=0.5, 0.80 and 0.96), RNG k–ε, hover, α=8°, M_{tip}=0.877, Ω=224.2 rad/s, Re=4.22x10^6

6.1.4 THE REALIZABLE *k–ε* MODEL

The realizable *k–ε* model is a relatively recent development and differs from the standard *k–ε* model in two important ways: the realizable *k–ε* model contains a new formulation for the turbulent viscosity. Furthermore, a new transport equation for the dissipation rate, *ε*, has been derived from an exact equation for the transport of the mean-square vorticity fluctuation. The term "realizable" means that the model satisfies certain mathematical constraints on the Reynolds stresses, consistent with the physics of turbulent flows. Neither the standard *k–ε* model nor the RNG *k–ε* model is realizable. An immediate benefit of the realizable *k–ε* model is that it more accurately predicts the spreading rate of both planar and round jets. It is also likely to provide superior performance for flows involving rotation, boundary layers under strong adverse pressure gradients, separation, and recirculation.

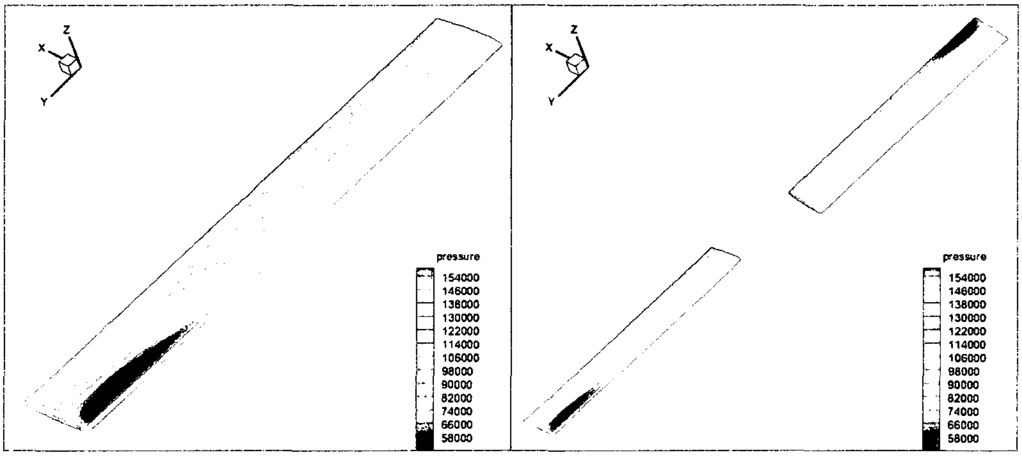

Figure 6.7: Pressure contours on the blade and the rotor surfaces, Realizable *k–ε*, lifting, M_{tip}=0.877, Ω=224.2 rad/s, α=8°, Re=4.22x10^6

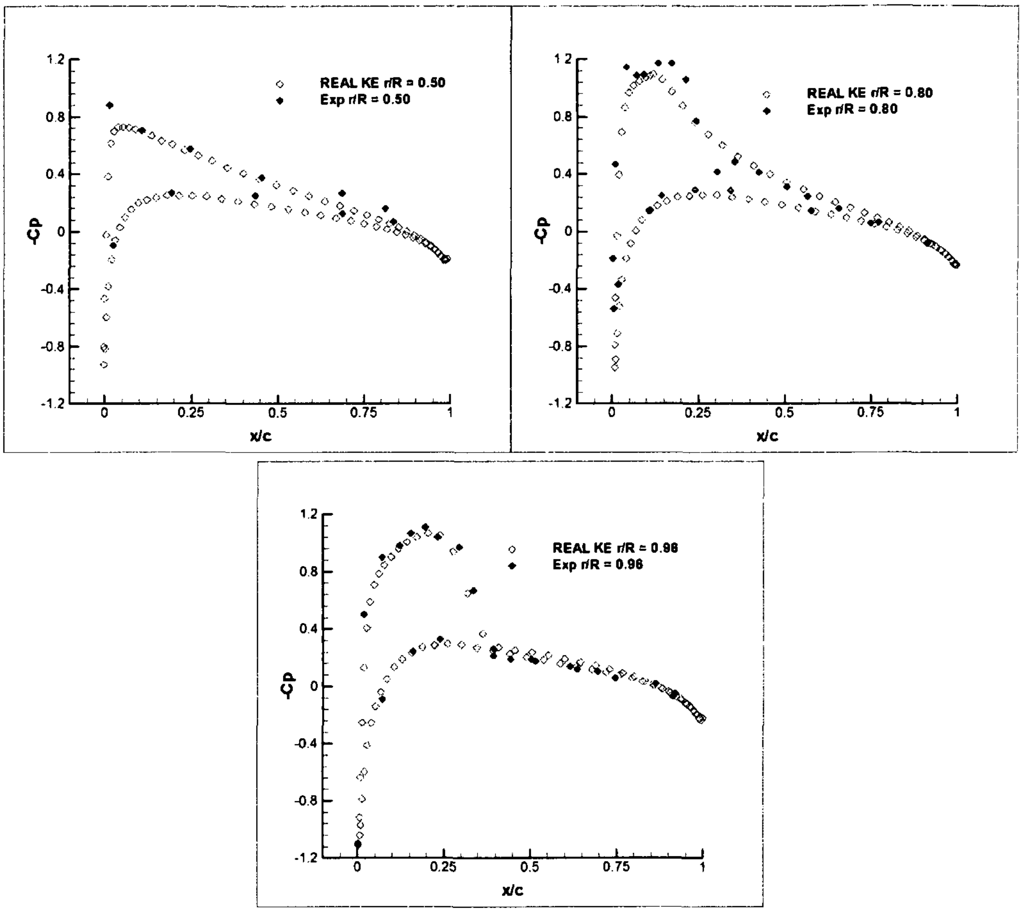

Figure 6.8: C_p distributions at three span wise locations (r/R=0.5, 0.80 and 0.96), Realizable k–ε, hover, $\alpha=8^\circ$, $M_{tip}=0.877$, $\Omega=224.2$ rad/s, $Re=4.22\times10^6$

6.1.5 THE STANDARD *k-ω* MODEL

The standard *k-ω* model is based on the Wilcox *k-ω* model, which incorporates modifications for low-Reynolds-number effects, compressibility, and shear flow spreading. The Wilcox model predicts free shear flow spreading rates that are in close agreement with measurements for far wakes, mixing layers, and plane, round, and radial jets, and is thus applicable to wall-bounded flows and free shear flows.

The standard *k-ω* model is an empirical model based on model transport equations for the turbulence kinetic energy (*k*) and the specific dissipation rate (*ω*), which can also be thought of as the ratio of *ω* to *k*. As the *k-ω* model has been modified over the years, production terms have been added to both the *k* and *ω* equations, which have improved the accuracy of the model for predicting free shear flows.

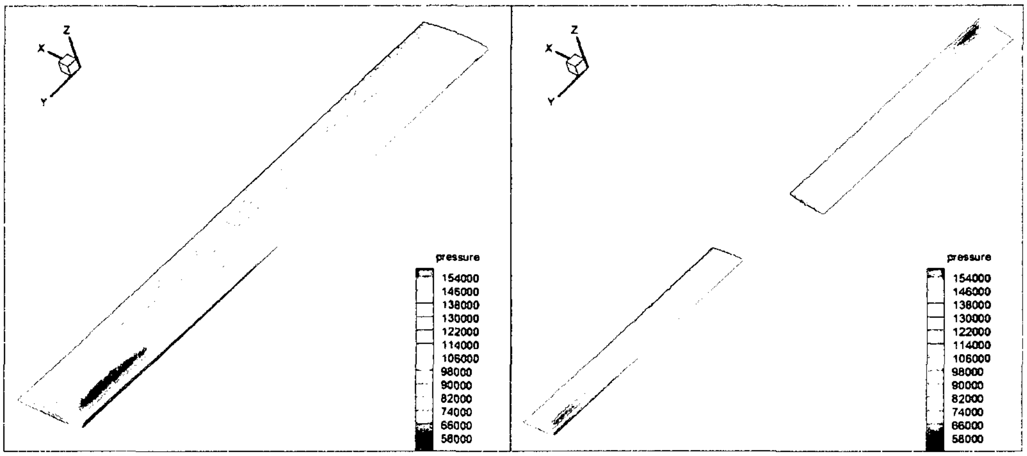

Figure 6.9: Pressure contours on the blade and the rotor surfaces, Standard *k-ω*, lifting, M_{tip}=0.877, Ω=224.2 rad/s, α=8°, Re=4.22x10^6

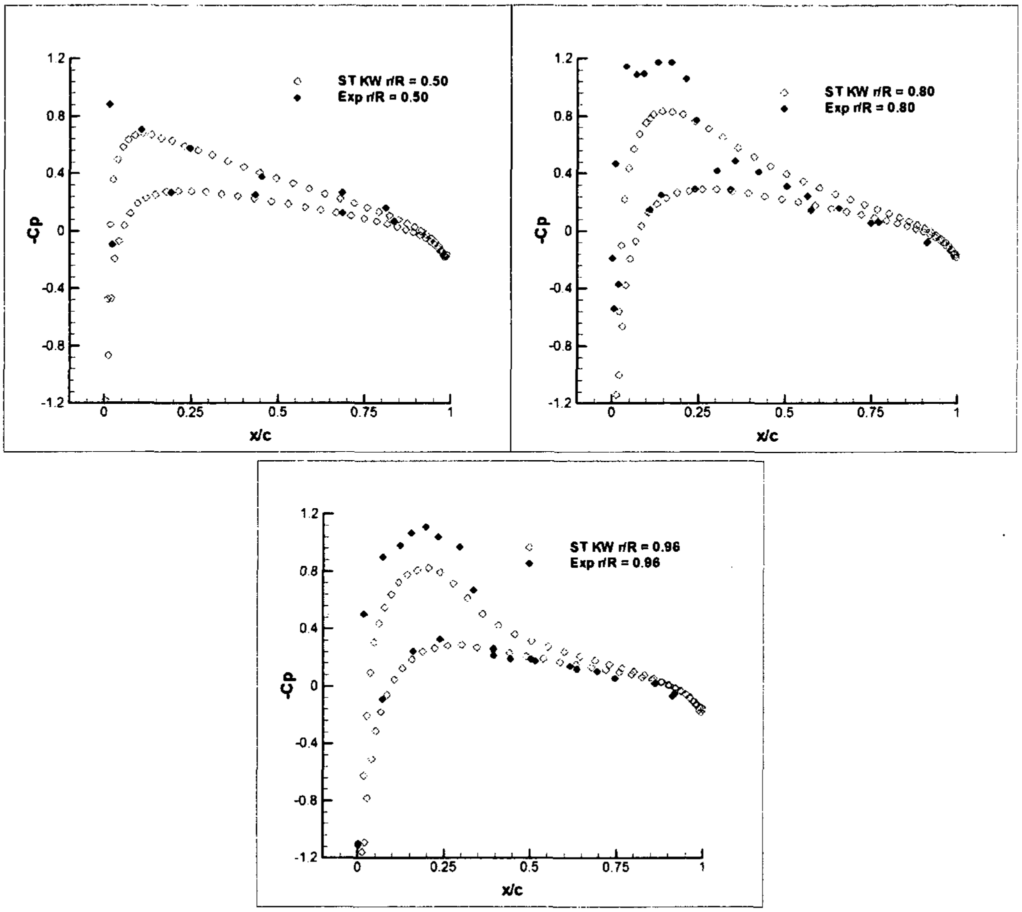

Figure 6.10: C_p distributions at three span wise locations (r/R=0.5, 0.80 and 0.96), Standart *k-ω*, hover, $\alpha=8^{\circ}$, $M_{tip}=0.877$, $\Omega=224.2$ rad/s, $Re=4.22\times10^{6}$

6.1.6 SHEAR-STRESS TRANSPORT (SST) k-ω MODEL

The shear-stress transport (SST) k–ω model was developed by Menter to effectively blend the robust and accurate formulation of the k–ω model in the near-wall region with the free-stream independence of the k–ω model in the far field. To achieve this, the k–ε model is converted into a k–ω formulation. The SST k–ω model is similar to the standard k–ω model, but includes the following refinements. The standard k–ω model and the transformed k–ε model are both multiplied by a blending function and both models are added together. The blending function is designed to be one in the near-wall region, which activates the standard k–ω model, and zero away from the surface, which activates the transformed k–ε model. The SST model incorporates a damped cross-diffusion derivative term in the k–ω equation. The definition of the turbulent viscosity is modified to account for the transport of the turbulent shear stress. The modeling constants are different. These features make the SST k–ω model more accurate and reliable for a wider class of flows (e.g., adverse pressure gradient flows, airfoils, transonic shock waves) than the standard k–ω model. Other modifications include the addition of a cross-diffusion term in the ω equation and a blending function to ensure that the model equations behave appropriately in both the near-wall and far-field zones.

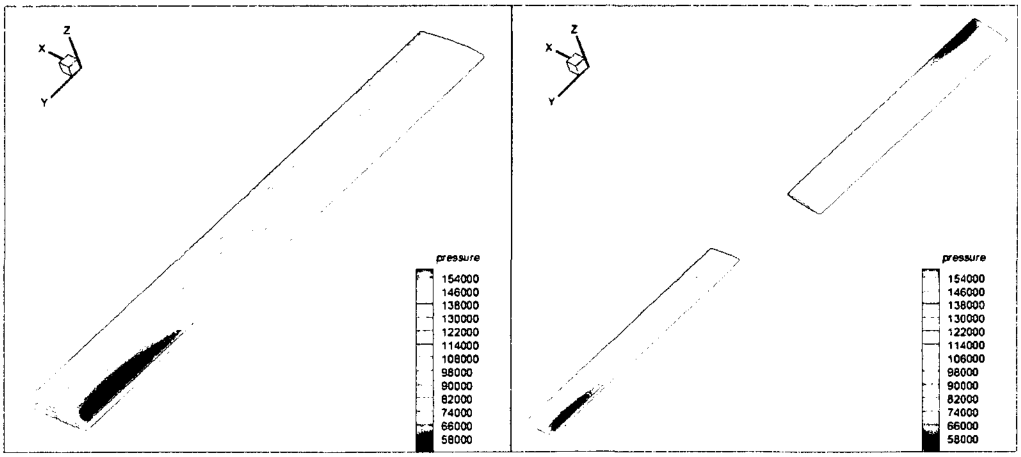

Figure 6.11: Pressure contours on the blade and the rotor surfaces, SST *k-ω*, lifting, M_{tip}=0.877, Ω=224.2 rad/s, α=8°, Re=4.22x10^6

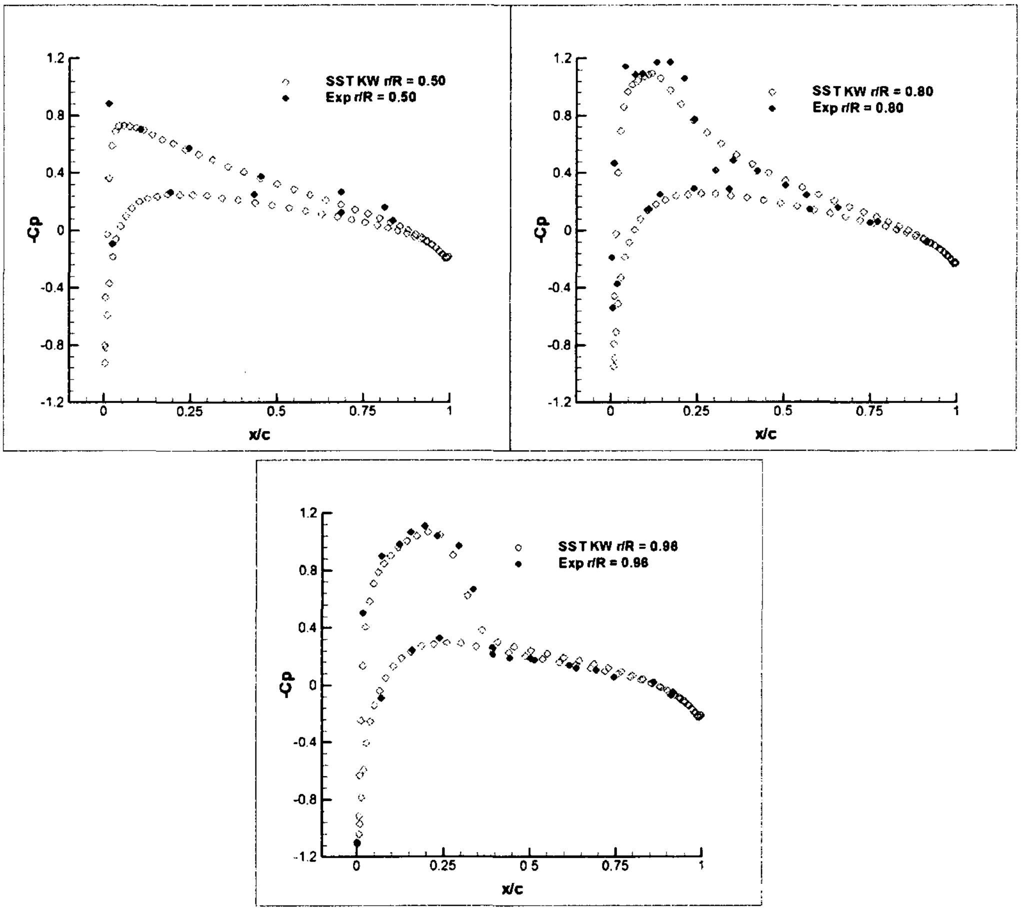

Figure 6.12: C_p distributions at three span wise locations (r/R=0.5, 0.80 and 0.96), SST *k-ω*, hover, α=8°, M_{tip}=0.877, Ω=224.2 rad/s, Re=4.22x10^6

6.1.7 THE LARGE EDDY SIMULATION (LES) MODEL

Turbulent flows are characterized by eddies with a wide range of length and time scales. The largest eddies are typically comparable in size to the characteristic length of the mean flow. The smallest scales are responsible for the dissipation of turbulence kinetic energy. It is possible, in theory, to directly resolve the whole spectrum of turbulent scales using an approach known as direct numerical simulation (DNS). No modeling is required in DNS. However, DNS is not feasible for practical engineering problems involving high Reynolds number flows. The cost required for DNS to resolve the entire range of scales is proportional to Re_t^3, where Re_t is the turbulent Reynolds number. Clearly, for high Reynolds numbers, the cost becomes prohibitive. In LES, large eddies are resolved directly, while small eddies are modeled. Large eddy simulation (LES) thus falls between DNS and RANS in terms of the fraction of the resolved scales.

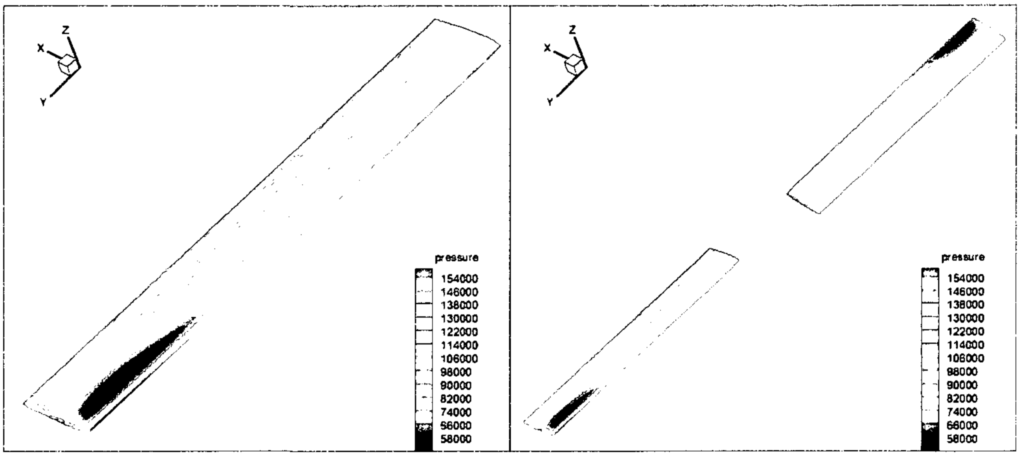

Figure 6.13: Pressure contours on the blade and the rotor surfaces, LES, lifting, M_{tip}=0.877, Ω=224.2 rad/s, α=8°, Re=4.22x10^6

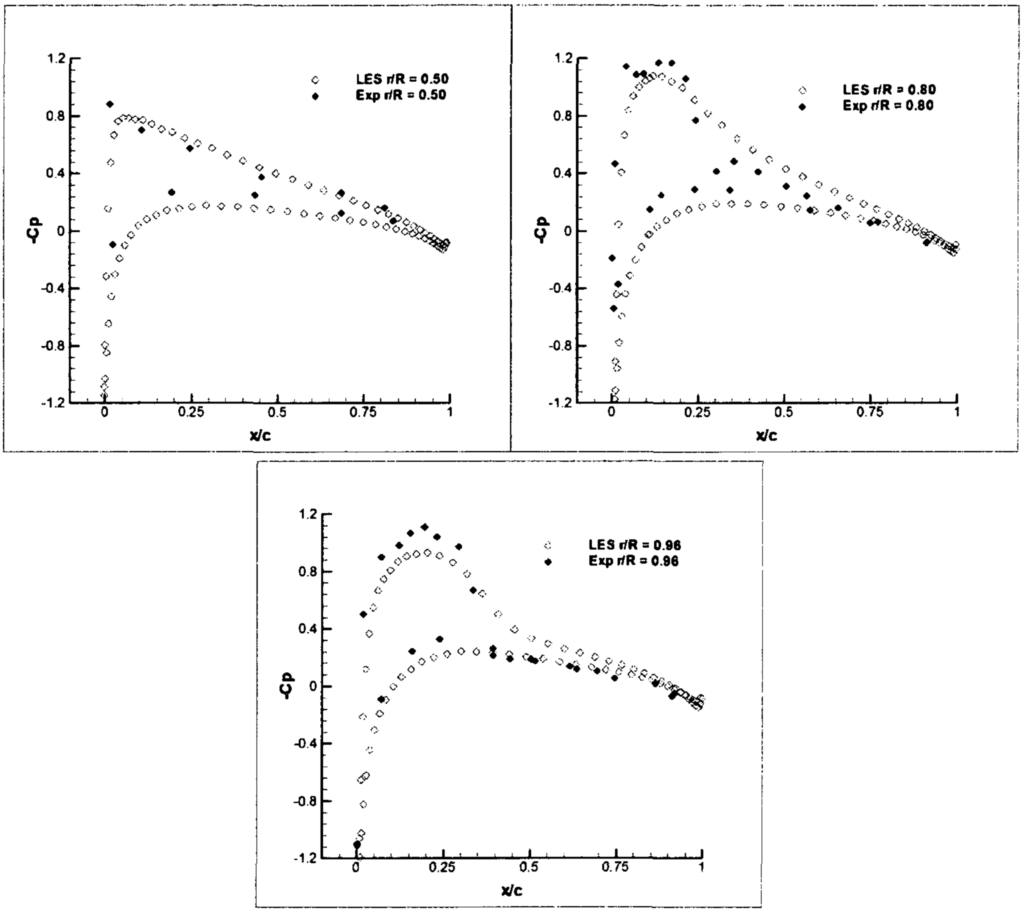

Figure 6.14: C_p distributions at three span wise locations (r/R=0.5, 0.80 and 0.96), LES, hover, $\alpha=8^{\circ}$, $M_{tip}=0.877$, $\Omega=224.2$ rad/s, $Re=4.22\times10^{6}$

It has been observed that the overall CFD results show good agreement with experimental data. However, while the pressure values computed by employing Spalart–Allmaras, The Standart $k-\varepsilon$, RNG $k-\varepsilon$, *Realizable* $k-\varepsilon$ and SST $k-\omega$ turbulence models seem to be identical to the experimental data, The predictions of The Standart $k-\omega$ and LES models are not as accurate as the other models. In CFD computations, the level of accuracy required and the available computational resources are quite important and have to be considered carefully. As the number of equations to be solved increases, the computational cost will also increase. Among the models tested, Spalart-Allmaras is the only one-equation model. Therefore, it is the cheapest model by means of computational cost. Hence, Spalart-Allmaras turbulence model has been chosen and utilized in the entire simulations.

6.2 SINGLE ROTOR SIMULATIONS

This part addresses the simulations of the flow around rigid, isolated model helicopter rotors in hover and forward flight without pitching and flapping motion. Several types of 4 digit NACA airfoils have been handled for the blade geometry. One-equation Spalart–Allmaras turbulence model has been utilized for all single rotor cases. The details of the blade geometries are presented in the following part.

A helicopter flies for the same basic reason that any conventional aircraft flies, because aerodynamic forces necessary to keep it aloft are produced when air passes about the rotor blades. The rotor blade, or airfoil, is the structure that makes flight possible. Its shape produces lift when it passes through the air. Helicopter blades have airfoil sections designed for a specific set of flight characteristics. Usually the designer must compromise to obtain an airfoil section that has the best flight characteristics for the mission the aircraft will perform.

Airfoil sections are of two basic types: symmetrical or non-symmetrical. Symmetrical airfoils have identical upper and lower surfaces. They are suited to rotary-wing applications because they have almost no center of pressure travel. Travel remains relatively constant under varying angles of attack, affording the best lift-drag ratios for the full range of velocities from rotor blade root to tip. However, the symmetrical airfoil produces less lift than a nonsymmetrical airfoil and also has relatively undesirable stall characteristics. The helicopter blade must adapt to a wide range of airspeeds and angles of attack during each revolution of the rotor. The symmetrical airfoil delivers acceptable performance under those alternating conditions. Other benefits are lower cost and ease of construction as compared to the nonsymmetrical airfoil.

Non-symmetrical (cambered) airfoils may have a wide variety of upper and lower surface designs. They are currently used on some CH-47 and all OH-58 Army helicopters, and are increasingly being used on newly designed aircraft. Advantages of the nonsymmetrical airfoil are increased lift-drag ratios and more desirable stall characteristics. Non-symmetrical airfoils were not used in earlier helicopters because the center of pressure location moved too much when the angle of attack was changed. When the center of pressure moves, a twisting force is exerted on the rotor blades. Rotor system components had to be designed that would withstand the twisting force. Recent design processes and new materials used to manufacture rotor systems have partially overcome the problems associated with use of non-symmetrical airfoils.

6.2.1 MESH GENERATION FOR SINGLE ROTOR CASES

In validation cases, satisfactory results have been obtained by using hybrid mesh technique to generate the adequate computational domain. The same technique has been applied for generating the grids for single rotor analyses. The structured block around the blade is an H-H-O topology with 41x41x51 grid points in stream wise, span wise and normal directions, respectively. Hybrid mesh is composed of 288,000 hexahedral and 1,148,209 mixed cells (total 1,436,209). NACA airfoils used in the computations are shown in Figure 6.15. The modeled geometry of the rotor (Aspect Ratio AR=13.7, chord length c=0.216 m and diameter $2r$=5.92 m) is displayed in Figure 3.a. Details of the computational domain are presented in Figures 6.16-6.18.

(a) NACA 0012 (b) NACA 2112

(c) NACA 2712 (d) NACA 4112

(e) NACA 4412 (f) NACA 4712

(g) NACA 6212 (h) NACA 6612

Figure 6.15: NACA airfoils used in single rotor simulations.

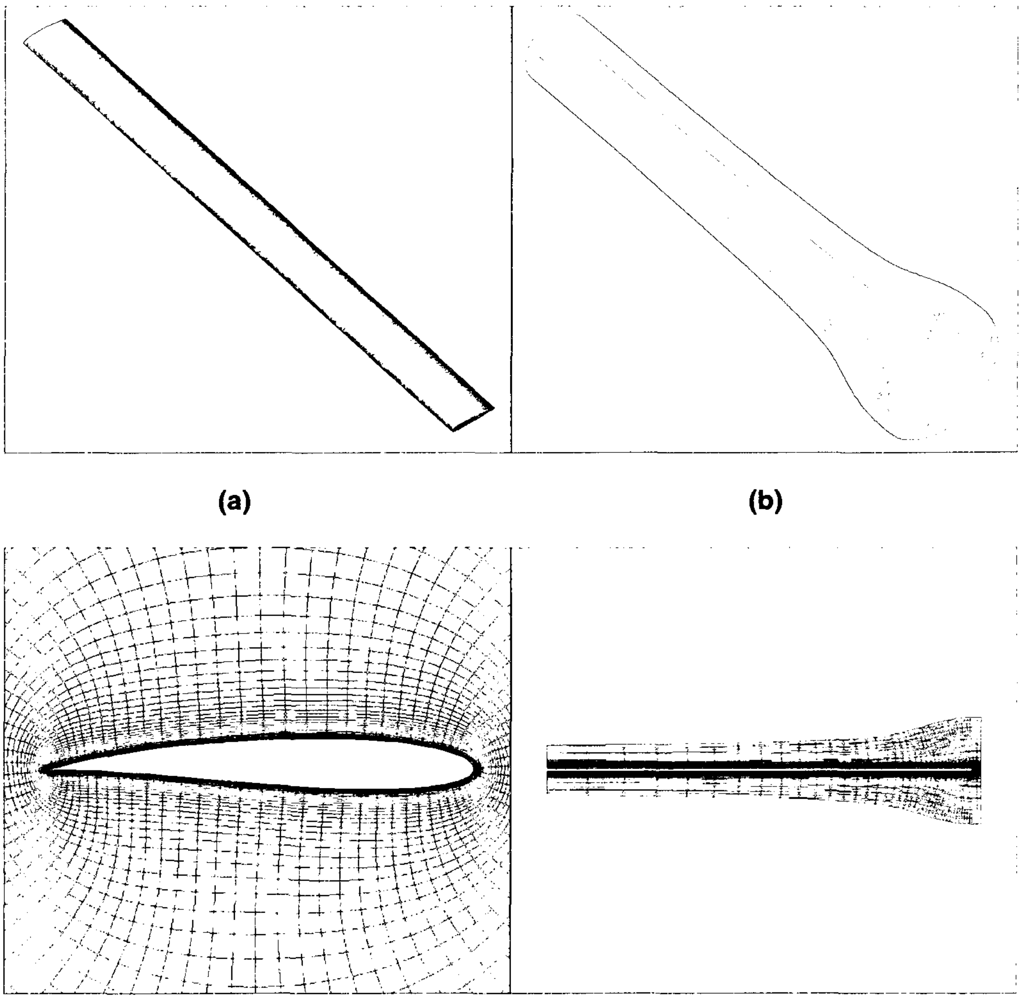

(a) (b)

(c) (d)

Figure 6.16: (a) Blade surface grid, (b) Structured block around blade, (c) Cross-section in span wise direction, (d) Cross-section in stream wise direction.

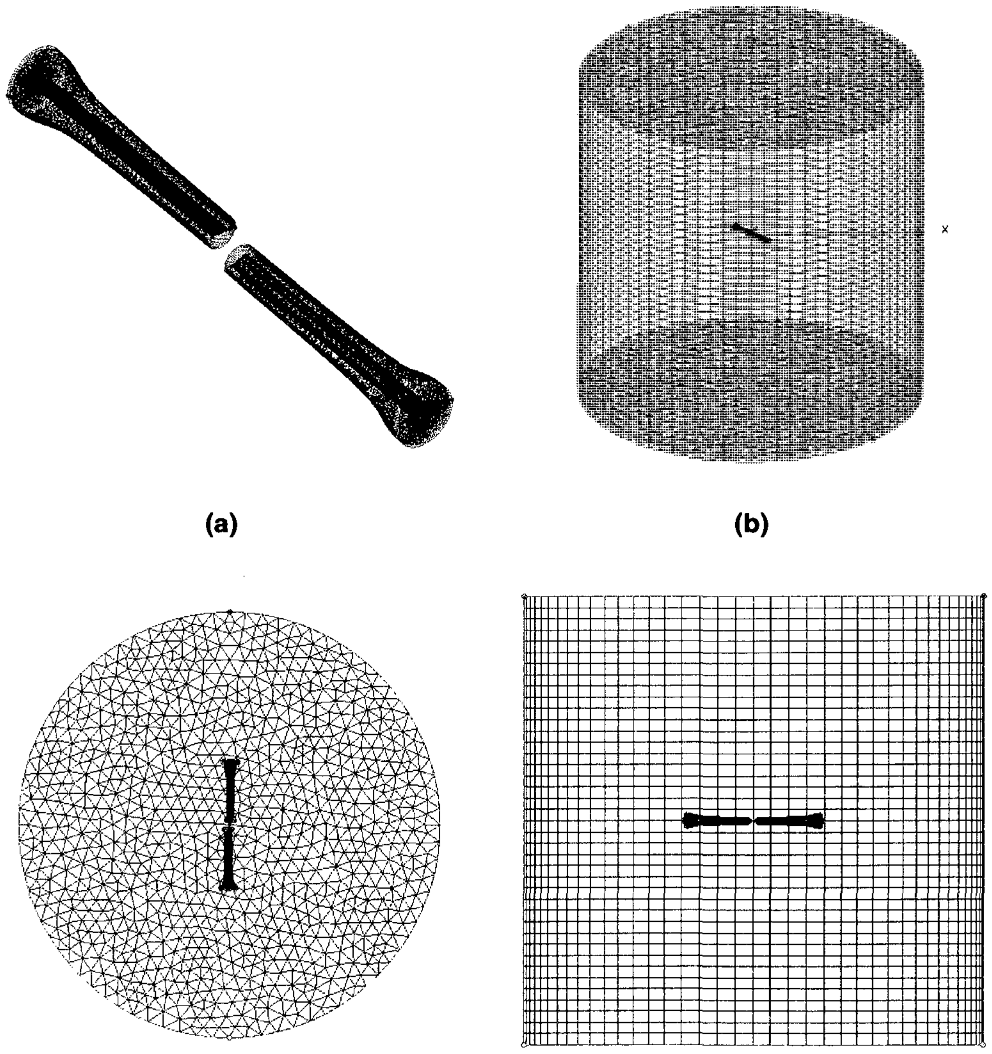

(a) (b)

(c) (d)

Figure 6.17: (a) Structured block around rotor, (b) Hybrid block around rotor, (c) Hybrid block, upper view, (d) Hybrid block, lateral view.

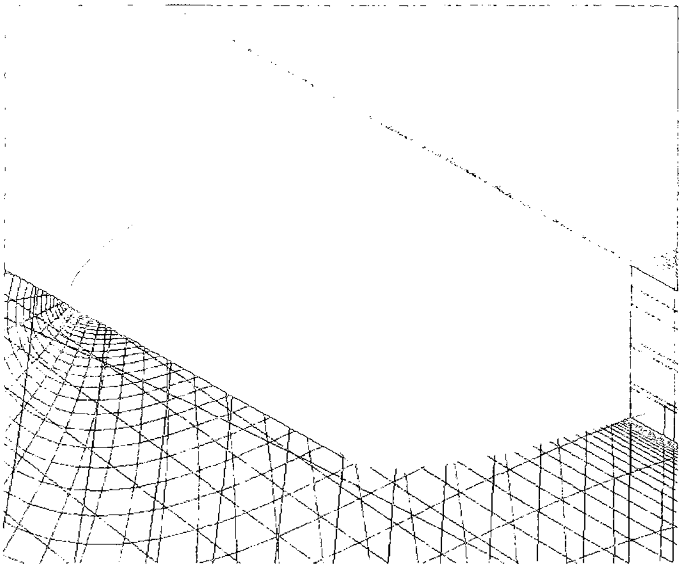

Figure 6.18: Mesh topology near tip region.

<table>
<tr><th colspan="7">Hover</th></tr>
<tr><th>Case</th><th>Ω</th><th>M_{tip}</th><th>α</th><th>Re</th><th>P_{inf}</th><th>ρ_{inf}</th></tr>
<tr><td>Non – Lifting</td><td>60 rad/s</td><td>0.52</td><td>0°</td><td>$2.67\text{x}10^6$</td><td>1 Atm</td><td>1.225 kg/m^3</td></tr>
<tr><td>Lifting</td><td>60 rad/s</td><td>0.52</td><td>8°</td><td>$2.67\text{x}10^6$</td><td>1 Atm</td><td>1.225 kg/m^3</td></tr>
<tr><th colspan="7">Forward Flight</th></tr>
<tr><td>Lifting</td><td>60 rad/s</td><td>0.52</td><td>8°</td><td>$2.67\text{x}10^6$</td><td>1 Atm</td><td>1.225 kg/m^3</td></tr>
<tr><th colspan="7">Advance Ratio</th></tr>
<tr><td>η</td><td>0.1</td><td>0.2</td><td>0.3</td><td>0.4</td><td>0.5</td><td>0.6</td></tr>
<tr><td>V_{inf} (m/s)</td><td>17</td><td>34</td><td>51</td><td>68</td><td>85</td><td>102</td></tr>
</table>

Figure 6.19: Summary of settings for single rotor simulations.

6.2.2 SINGLE ROTOR IN HOVER

Hovering is one of the most important features of a helicopter. It is where all the velocities in the lateral and vertical direction are zero and only the rotor generates just enough thrust to offset the helicopter's weight. It is this unique feature that makes helicopters different from other aircraft with the consequence that hovering is one of the two most important flight regimes for helicopters. Thus, it is important to be able to predict these flows accurately in order to improve the performance of the rotor design. In this section of the present study, several non–symmetric NACA airfoil sections have been utilized for lifting and non–lifting rotors. It has been intended to investigate and compare the lift force generated by these airfoil sections in rotational flows.

6.2.2.1 $\alpha=0^{\circ}$ CASE

For $\alpha=0^{\circ}$ cases, computations have been performed by setting the angular velocity to 60 rad/s which corresponds to a tip Mach number, $M_{tip}=0.52$ and a rotor tip velocity, $U_{tip}=176.8$ m/s. The collective pitch angle is 0°. In Figure 6.22, pressure contours at five span wise stations (r/R=0.50, 0.68, 0.80, 0.89 and 0.96) and pressure contours at r/R=0.89 on same blade have been displayed. Consequently, as an indication of the lift produced by the airfoil sections, pressure coefficient distributions at three different span wise stations (r/R=0.50, 0.80 and 0.96) are presented in Figure 6.23.

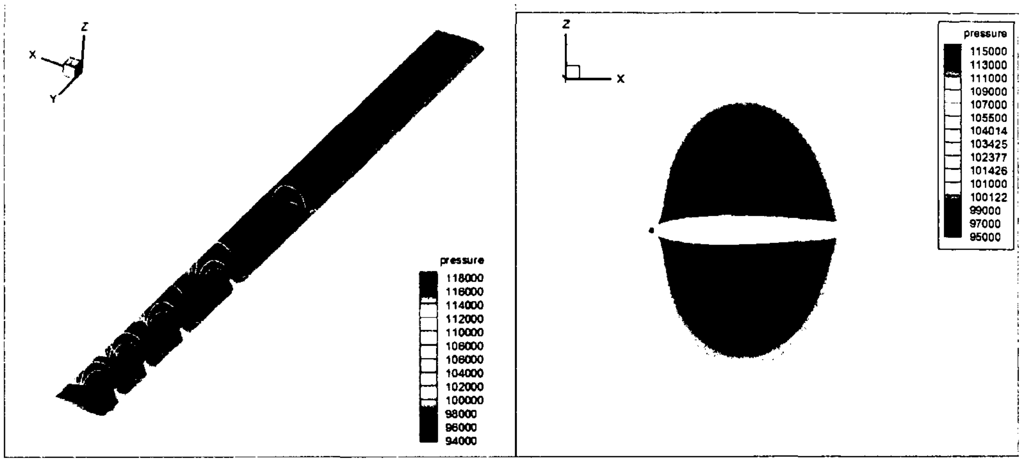

NACA 0012

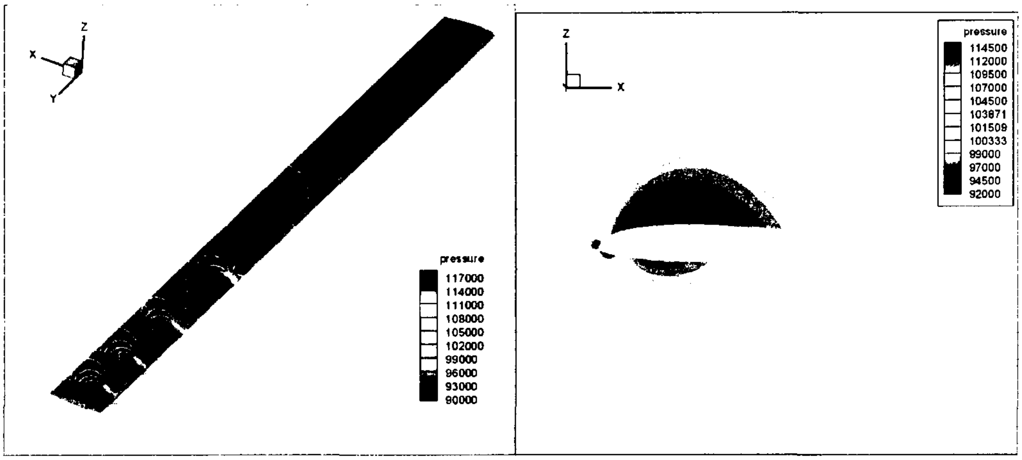

NACA 2112

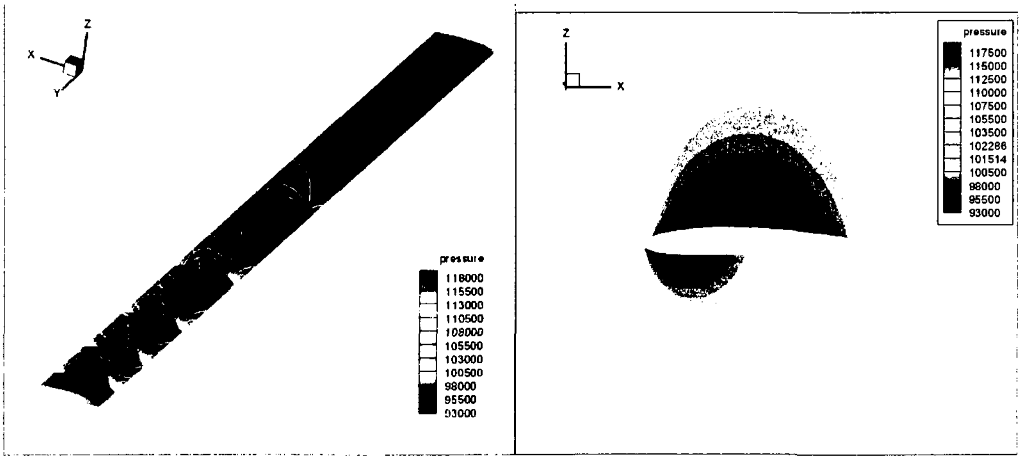

NACA 2712

Figure 6.20: Left; pressure contours at five span wise stations (r/R=0.50, 0.68, 0.80, 0.89 and 0.96), right; pressure contours at r/R=0.89, Spalart-Allmaras, $\alpha=0^\circ$, Re=2.35×10^6, hover, M_{tip}=0.52.

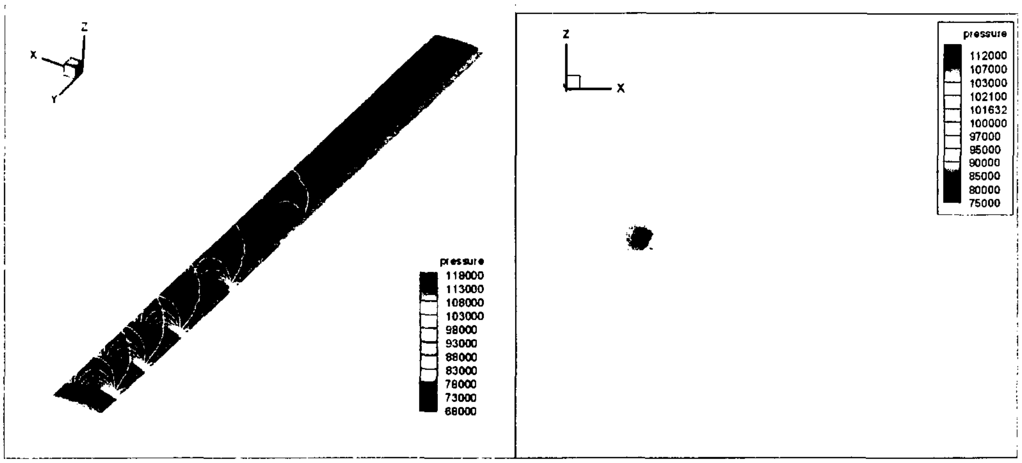

NACA 4112

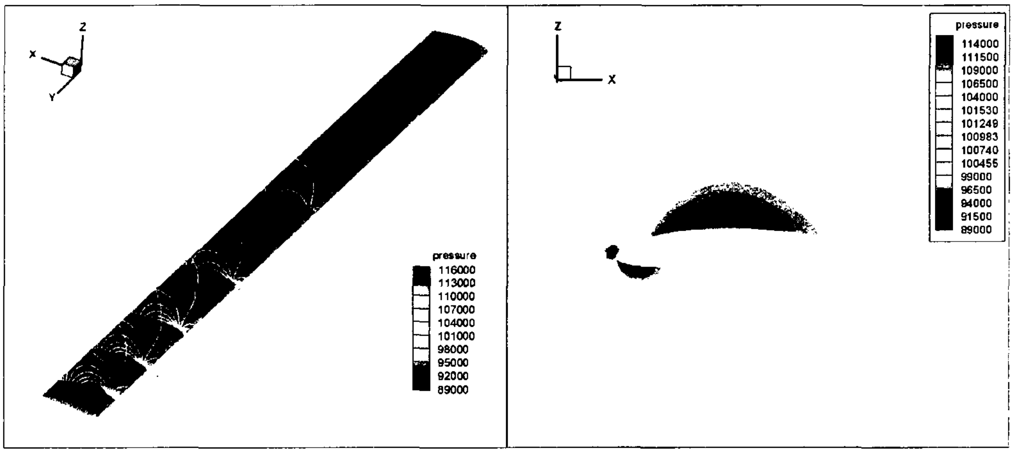

NACA 4412

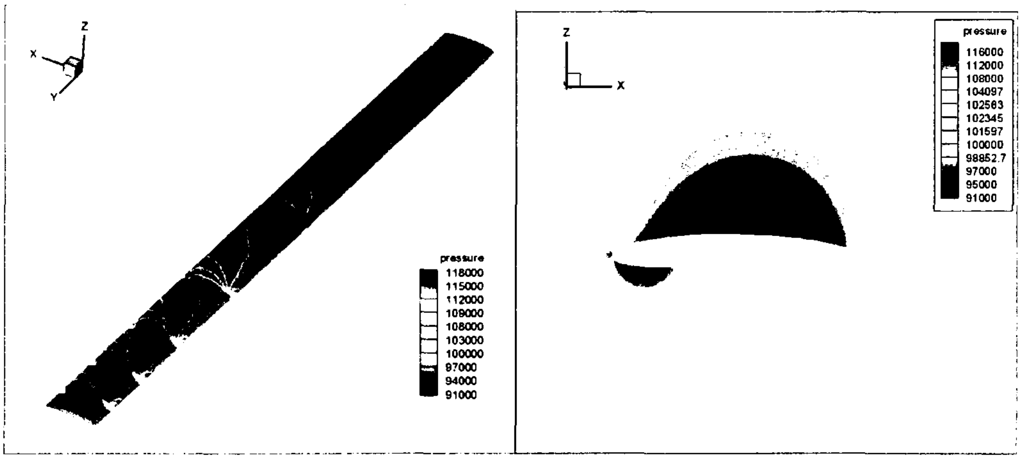

NACA 4712

Figure 6.20: Left; pressure contours at five span wise stations (r/R=0.50, 0.68, 0.80, 0.89 and 0.96), right; pressure contours at r/R=0.89, Spalart-Allmaras, α=0°, Re=2.35x10^6, hover, M$_{tip}$=0.52 (Continued)

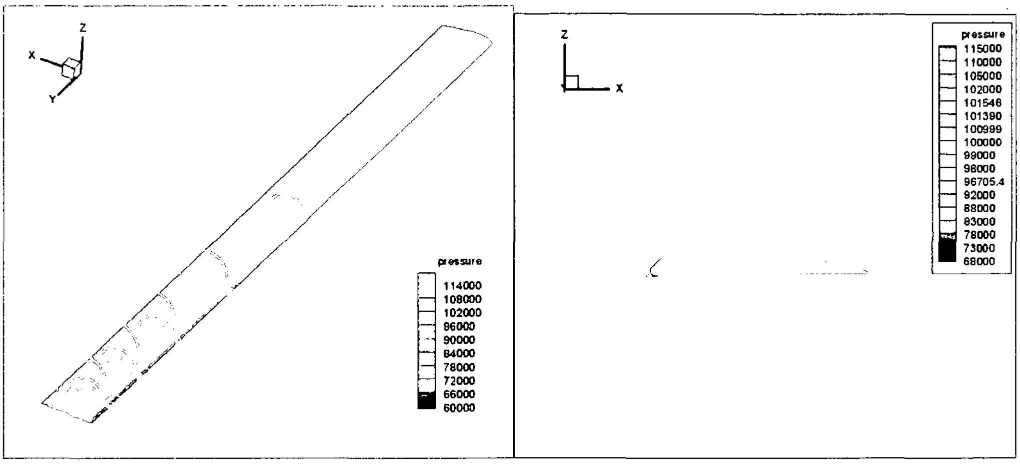

NACA 6212

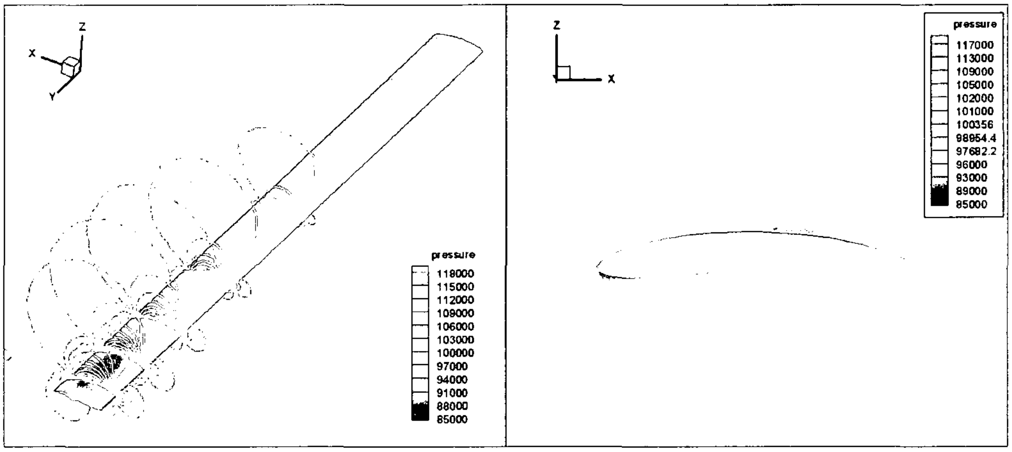

NACA 6612

Figure 6.20: Left; pressure contours at five span wise stations (r/R =0.50, 0.68, 0.80, 0.89 and 0.96), right; pressure contours at r/R = 0.89, Spalart-Allmaras, α=0°, Re=2.35x10^{6}, hover, M$_{tip}$=0.52 (Continued)

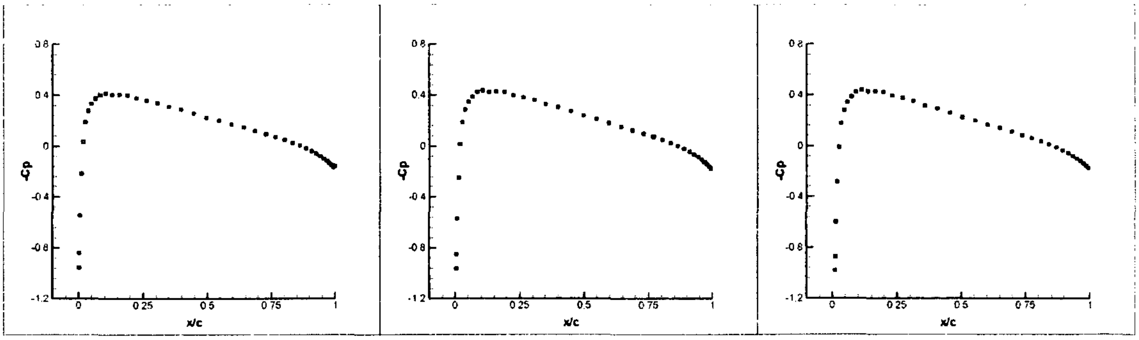

NACA 0012

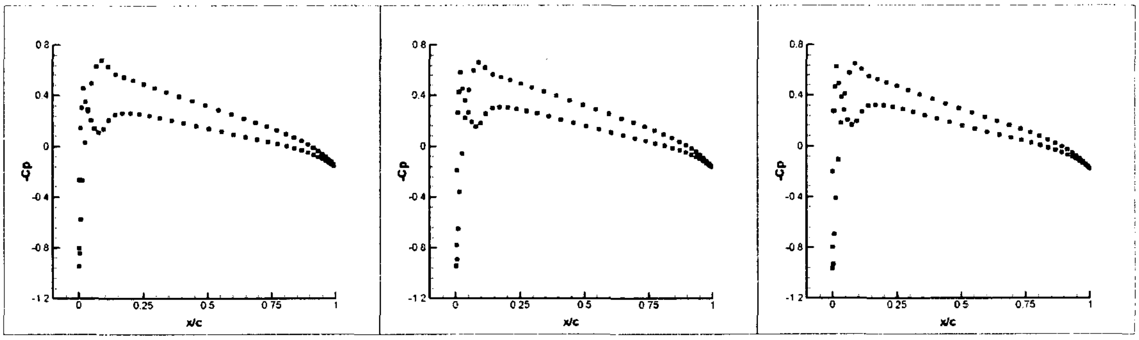

NACA 2112

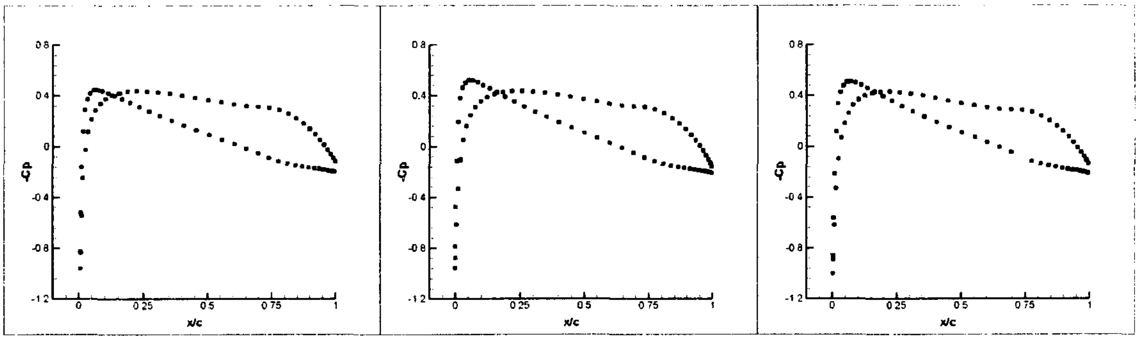

NACA 2712

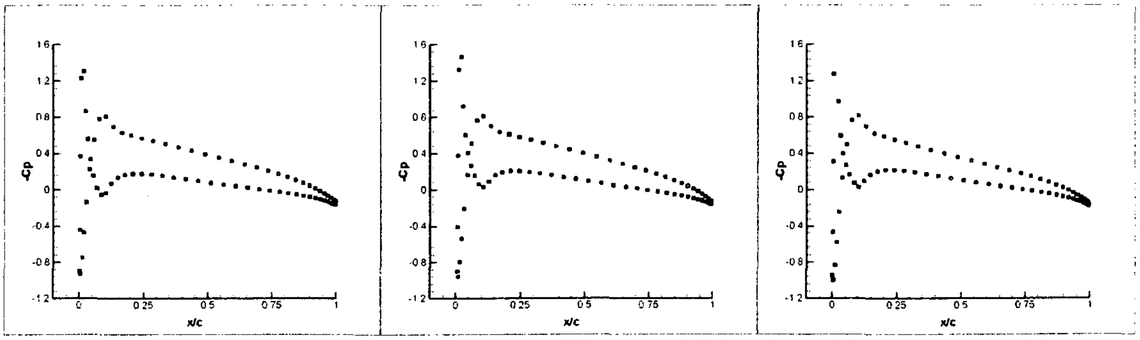

NACA 4112

Figure 6.21: C_p distributions for several NACA airfoils at three span wise stations (r/R=0.50, 0.80 and 0.96), Spalart-Allmaras, hover, M_{tip}=0.52, α=0°

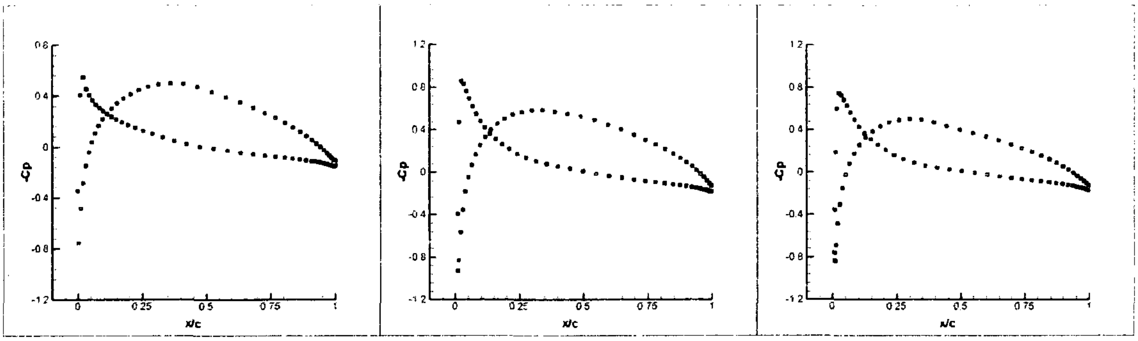

NACA 4412

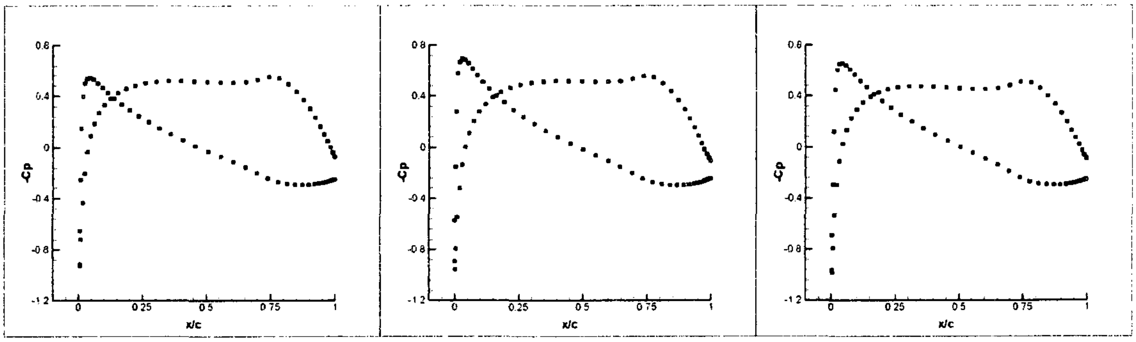

NACA 4712

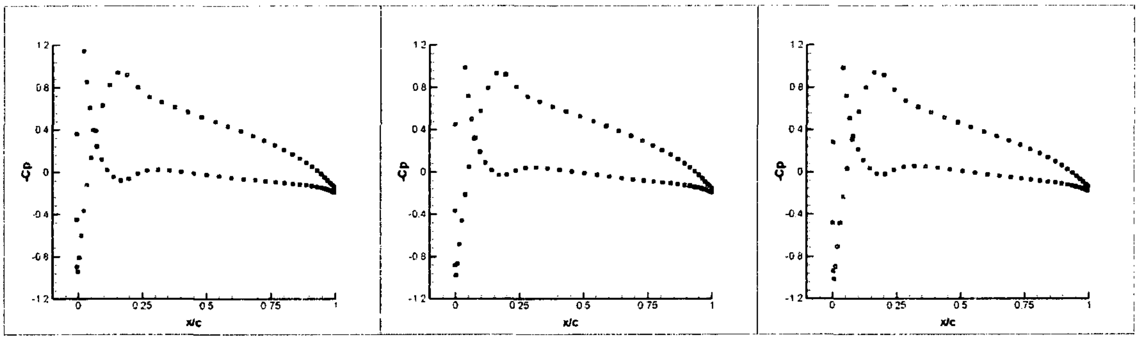

NACA 6212

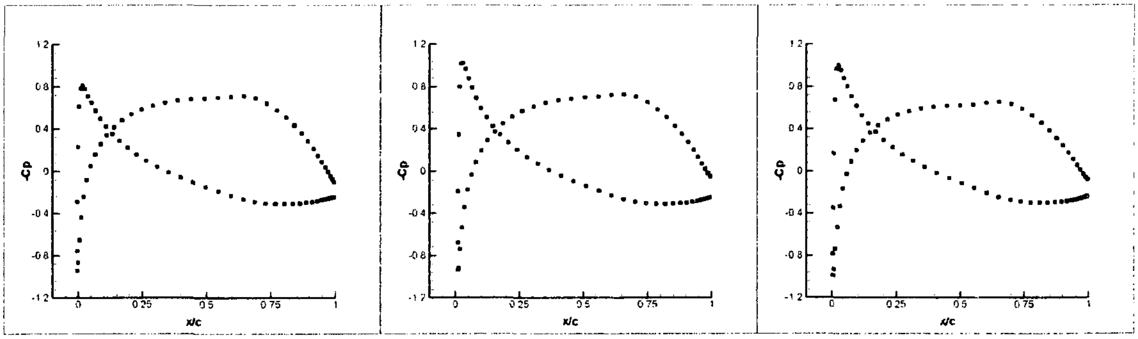

NACA 6612

Figure 6.21: C_p distributions for several NACA airfoils at three span wise stations (r/R=0.50, 0.80 and 0.96), Spalart-Allmaras, hover, M_{tip}=0.52, α=0° (Continued)

6.2.2.2 α=8° CASES

For α=8° cases, the angular velocity has been set to 60 rad/s (M_{tip}=0.52 and a rotor tip velocity, U_{tip}=176.8 m/s). Collective pitch angle has been set to 8°. In Figure 6.22, pressure contours at five span wise stations (r/R=0.50, 0.68, 0.80, 0.89 and 0.96) and pressure contours at r/R=0.89 on the same blade have been displayed. Pressure coefficient distributions at three span wise stations (r/R=0.50, 0.80, 0.96) are presented in Figure 6.23.

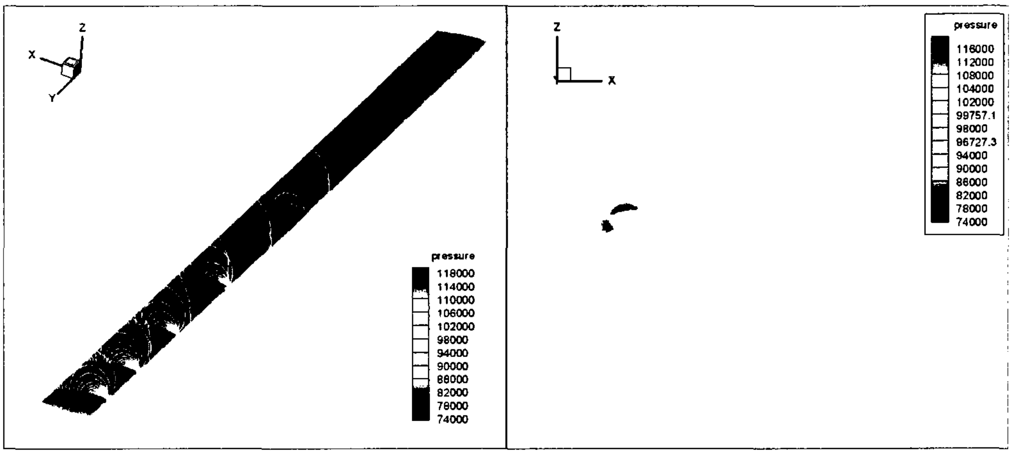

NACA 0012

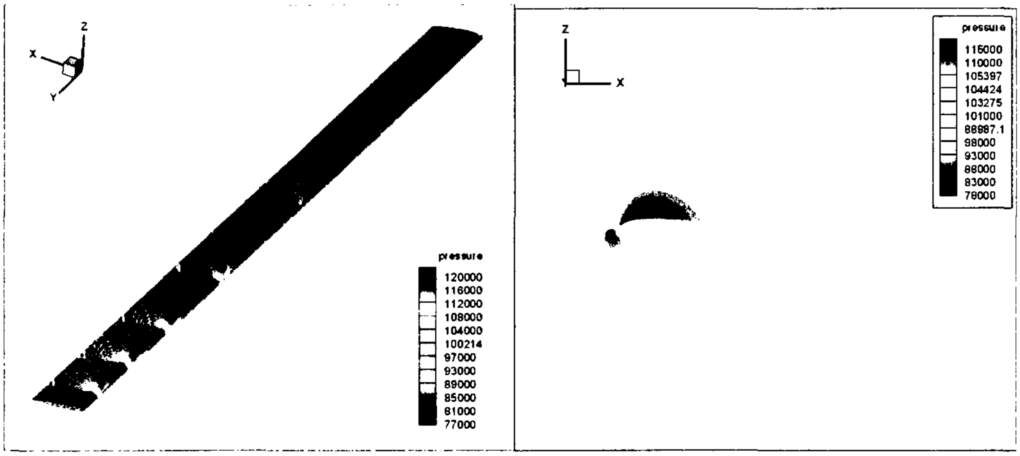

NACA 2112

Figure 6.22: Left; pressure contours at five span wise stations (r/R=0.50, 0.68, 0.80, 0.89 and 0.96), right; pressure contours at r/R=0.89, Spalart-Allmaras, α=8°, Re=2.35x10^6, hover, M_{tip}=0.52

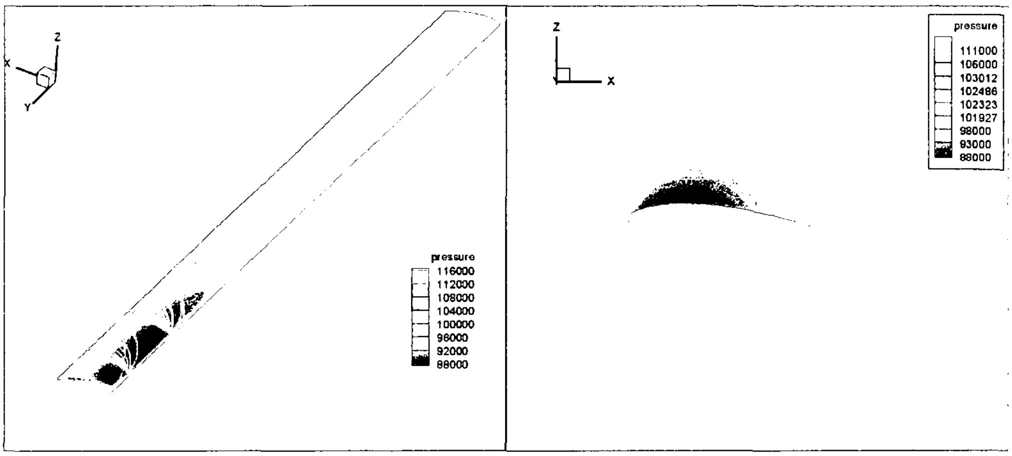

NACA 2712

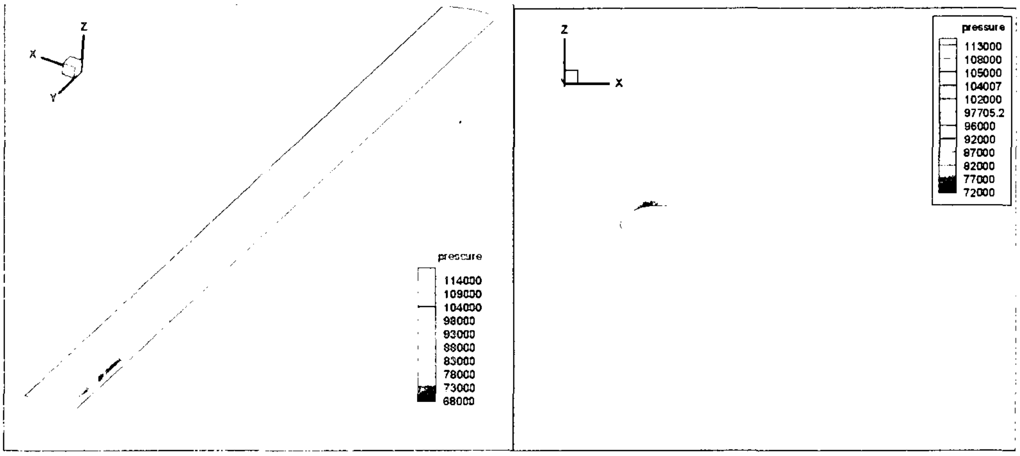

NACA 4112

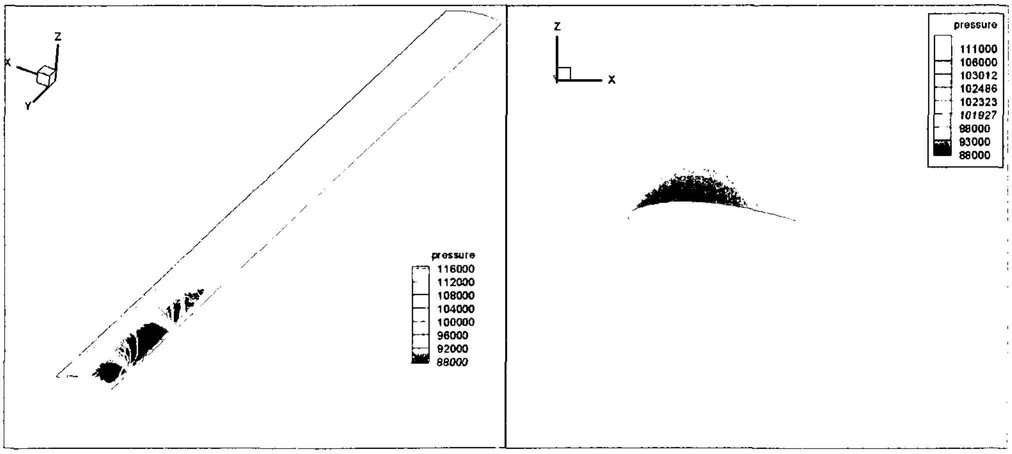

NACA 4412

Figure 6.22: Left; pressure contours at five span wise stations (r/R=0.50, 0.68, 0.80, 0.89 and 0.96), right; pressure contours at r/R=0.89, Spalart-Allmaras, $\alpha=8^{\circ}$, $Re=2.35\times10^{6}$, hover, $M_{tip}=0.52$ (Continued)

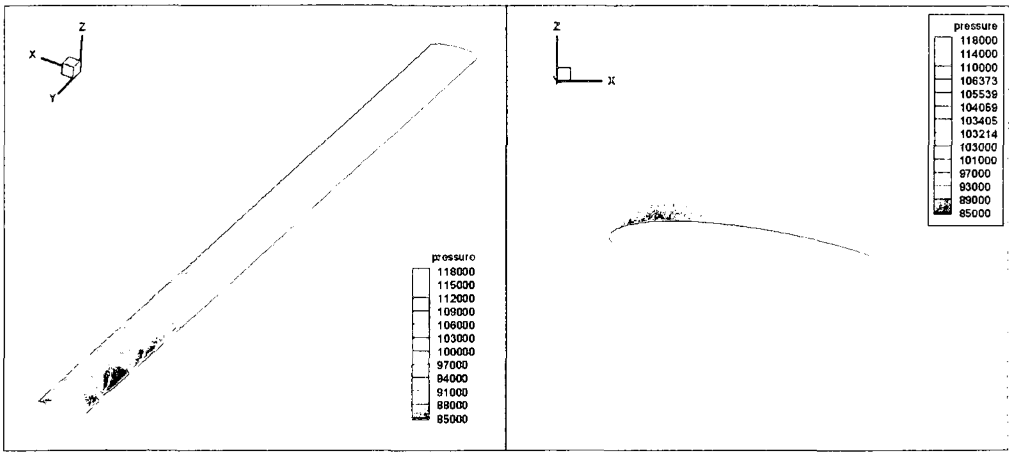

NACA 4712

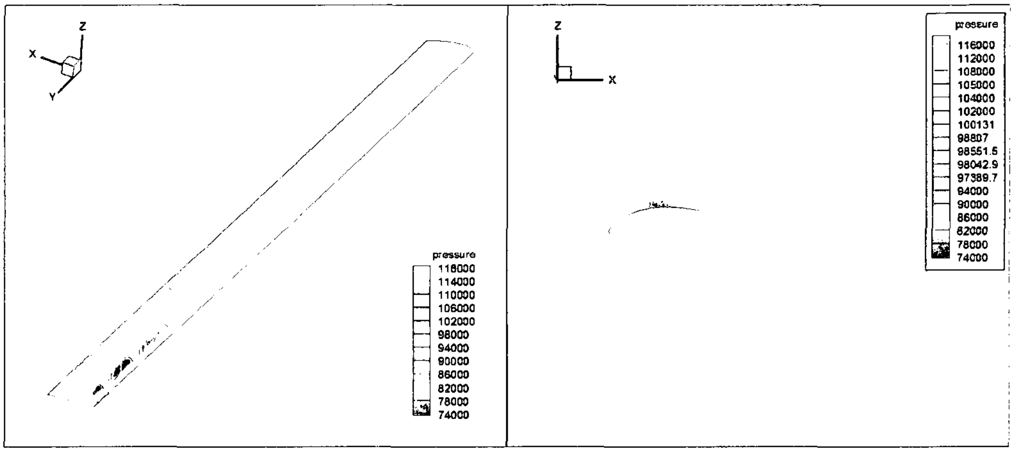

NACA 6212

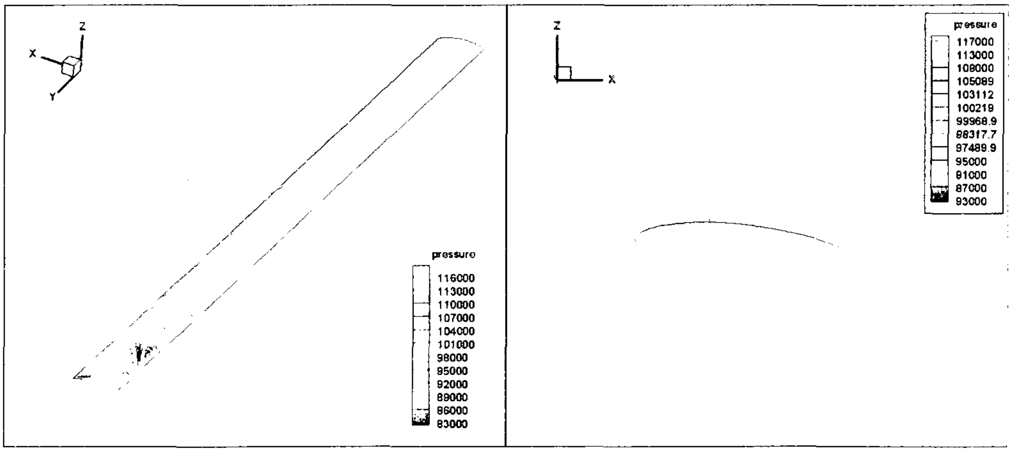

NACA 6612

Figure 6.22: Left; pressure contours at five span wise stations (r/R=0.50, 0.68, 0.80, 0.89 and 0.96), right; pressure contours at r/R=0.89, Spalart-Allmaras, $\alpha=8^{\circ}$, $Re=2.35\times10^{6}$, hover, $M_{tip}=0.52$ (Continued)

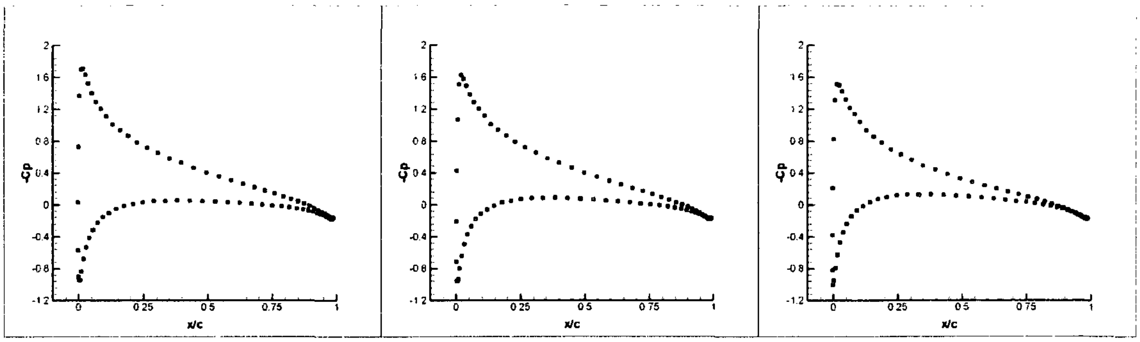

NACA 0012

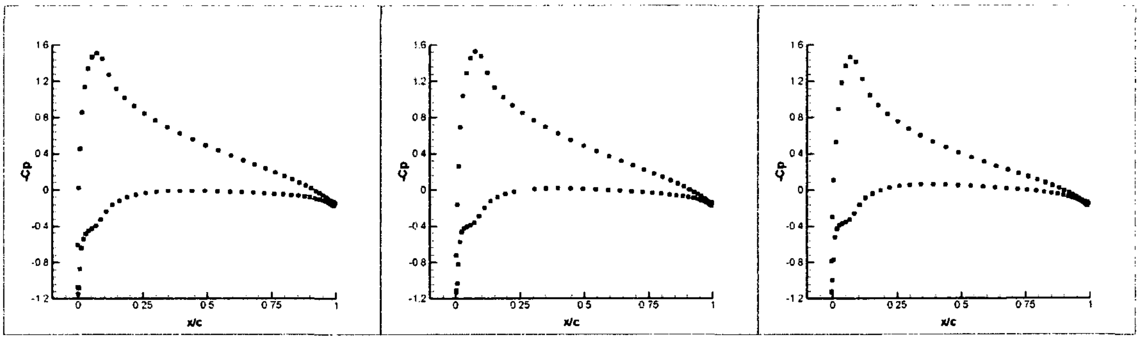

NACA 2112

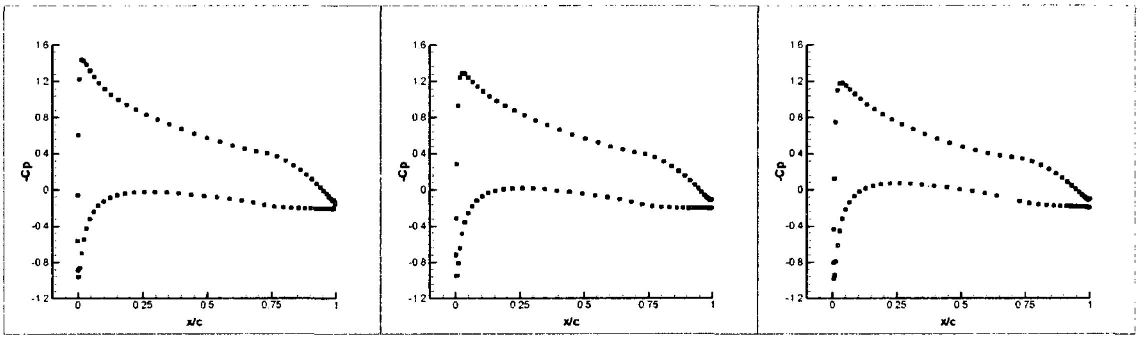

NACA 2712

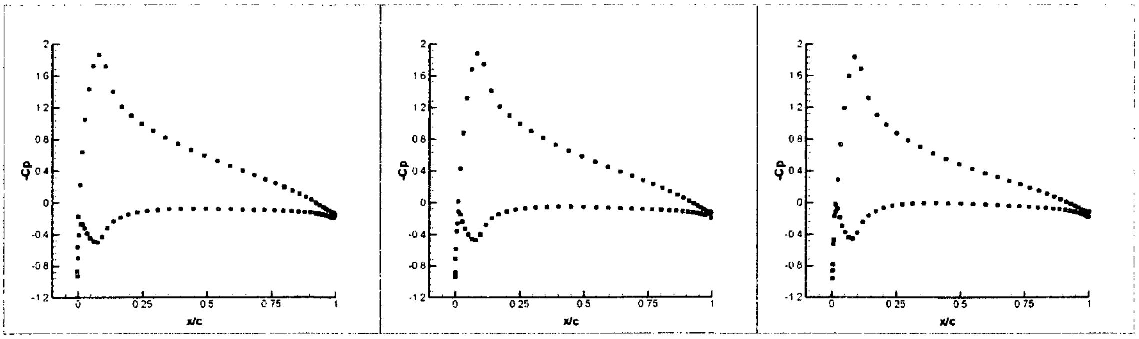

NACA 4112

Figure 6.23: C_p distributions for several NACA airfoils at three span wise stations (r/R=0.50, 0.80 and 0.96), Spalart-Allmaras, hover, M_{tip}=0.52, α=8°

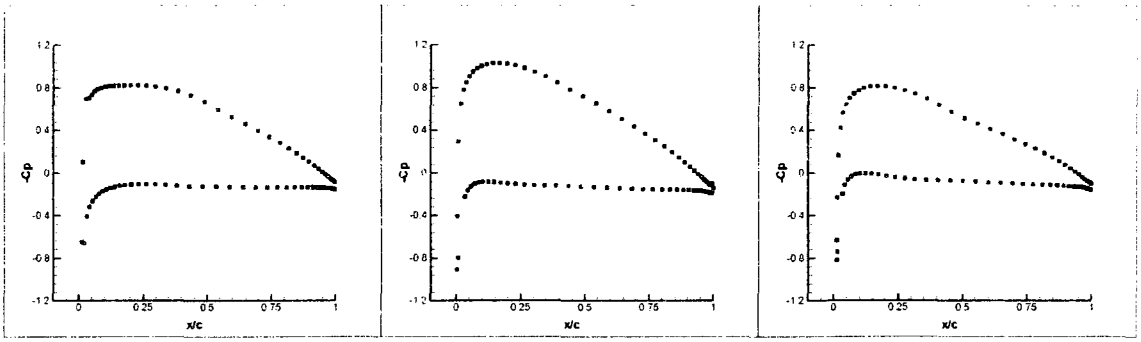

NACA 4412

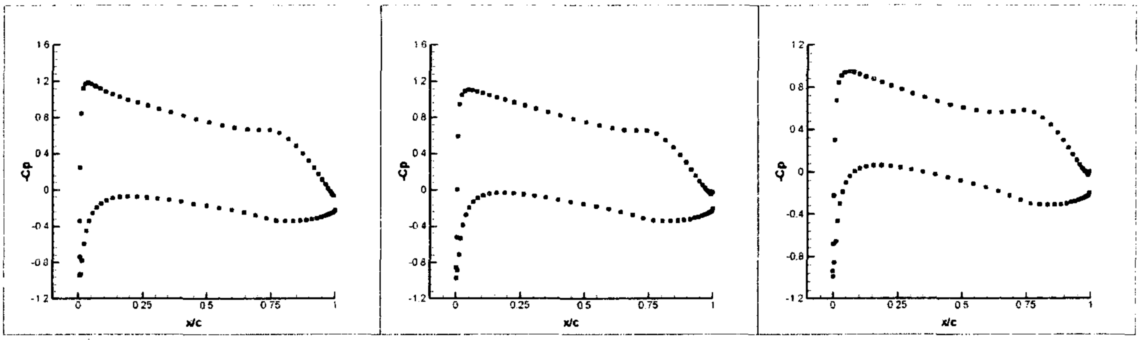

NACA 4712

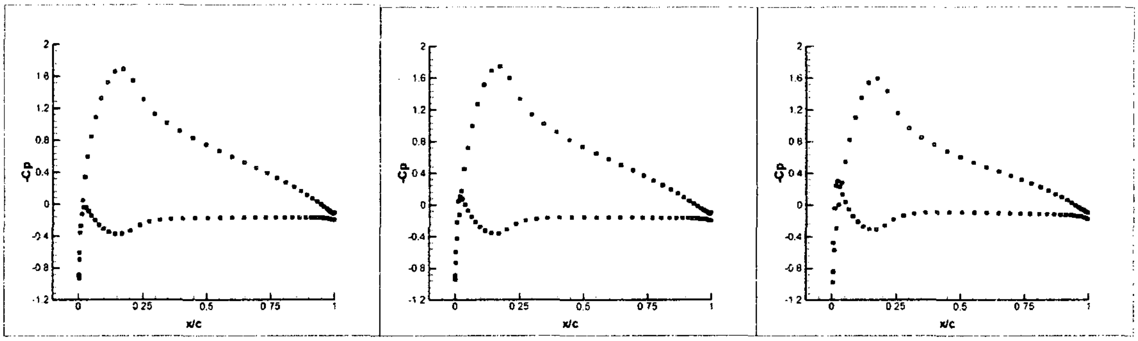

NACA 6212

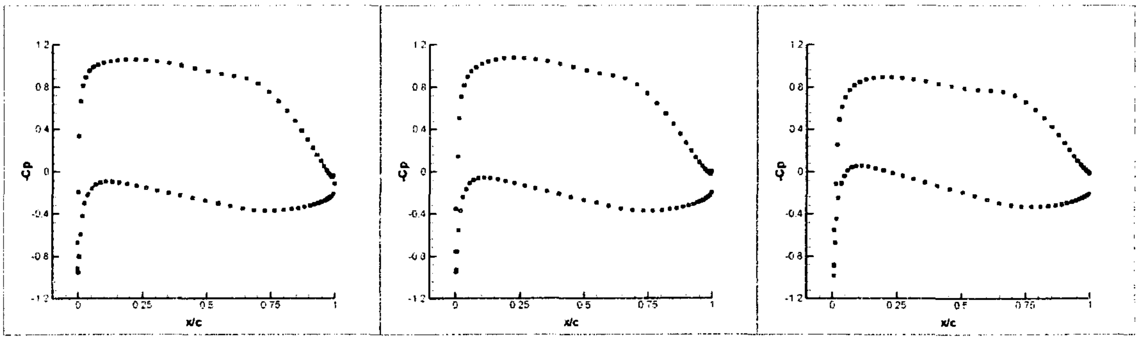

NACA 6612

Figure 6.23: C_p distributions for several NACA airfoils at three span wise stations (r/R=0.50, 0.80 and 0.96), Spalart-Allmaras, hover, M_{tip}=0.52, α=8° (Continued)

As expected, the symmetric NACA 0012 airfoil does not generate lift force at zero angle of attack. It requires a non-zero angle of attack to generate a lift force. However, non–symmetrical airfoil sections are capable of producing lift even if angle of attack is zero. For zero angle of attack cases, it seems that airfoil chamber is quite an important factor. It has been observed that as the chamber increases, the lift (pressure difference between upper and lower surfaces) increases. The airfoil section, which has the highest chamber, NACA 6612, seems to be the most effective one since it creates the highest amount of lift.

6.2.3 SINGLE ROTOR IN FORWARD FLIGHT

The flow past a rotor in forward flight is extremely challenging for the current numerical simulation codes. The advancing side of the rotor can experience transonic flow conditions leading to the formation of shocks and shock-boundary layer interactions. The flow in the root region is very low speed, and can contain regions of reverse flow on the retreating side. The retreating side of the rotor undergoes a rapid change in blade pitch angle that can cause dynamic stall. A dynamic stall is characterized by a delay in the onset of flow separation to a higher angle of attack than what would happen statically. This delay in stall onset is initially advantageous as far as the performance and operational flight envelope of a helicopter rotor are concerned. When dynamic flow separation does occur, it is found to be characterized by the shedding of a concentrated vortical disturbance from the leading edge region of the airfoil. This vortex disturbance passes over the upper surface of the airfoil and it enhances the lift being produced. However, this vortex is quickly swept over the chord of the blade by the oncoming flow and it produces a rapid aft movement of the center of pressure, which results in large nose-down pitching moments on the blade section and an increase in the torsional load on the blades. There is also a loss of lift.

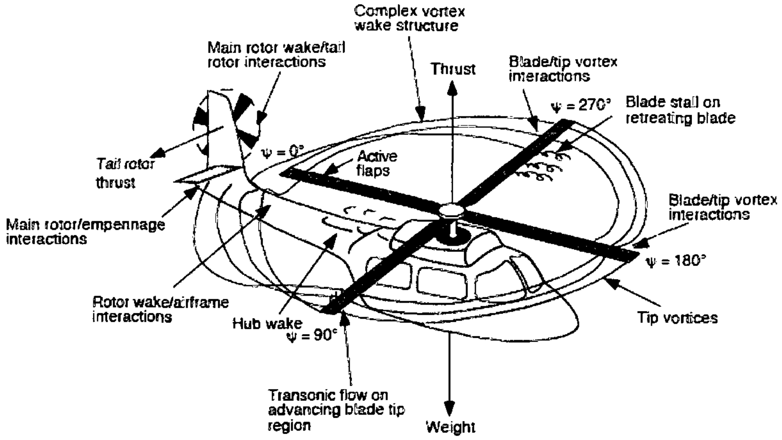

Figure 6.24: Typical flow phenomena found on a helicopter in forward flight.

The flow around each blade is also strongly influenced by the wake from previous blades, and so the capture of this wake is important. However, numerical diffusion/dispersion inherent in the current CFD codes severely compromises the resolution of the flow vorticity, and so this is a serious problem for a rotor flow simulation. Hover simulation requires the capture of several turns of the tip vortices to compute accurate blade loads, resulting in the requirement for fine meshes away from the surface, and a long numerical integration time for this wake to develop. Forward flight simulation also requires accurate capture of the vortical wake, but, depending on the advance ratio, fewer turns need to be captured as the wake is swept downstream. However, not only does the entire domain need to be solved, rather than the single blade for hover, but the wake is now unsteady, and so an unsteady solver must be used, which is not only more expensive than the steady solver used for hover, but can easily result in even higher numerical diffusion of the wake. Hence, it is extremely expensive to simulate these flows.

In the present study, the vortical wake has not been considered. Observations and analyses have been focused on the effects of forward flight speed on both advancing and retreating blades. One of the objectives of the present study is to verify that a coaxial rotor configuration may be a robust solution to mitigate the dynamic stall problem at high advance ratios. Before going through the coaxial rotor forward flight analysis, observing and analyzing the aerodynamic dissymmetry on the forward flying single rotors will prove to be a useful preparation.

The forward flight cases are the simulations of the flows around isolated model helicopter rotors in forward flight without a pitching or flapping motion. The blades are considered to have NACA 0012 sections with an angle of attack, α = 8^0. Spalart–Allmaras turbulence model has been utilized for all forward flight cases. The advance ratio has been set to six different values, η=0.1, 0.2, 0.3, 0.4, 0.5 and 0.6. For these six advance ratios, solutions have been obtained and C_p distributions at r/R = 0.80 on advancing and retreating blades have been compared and displayed (Fig. 6.25).

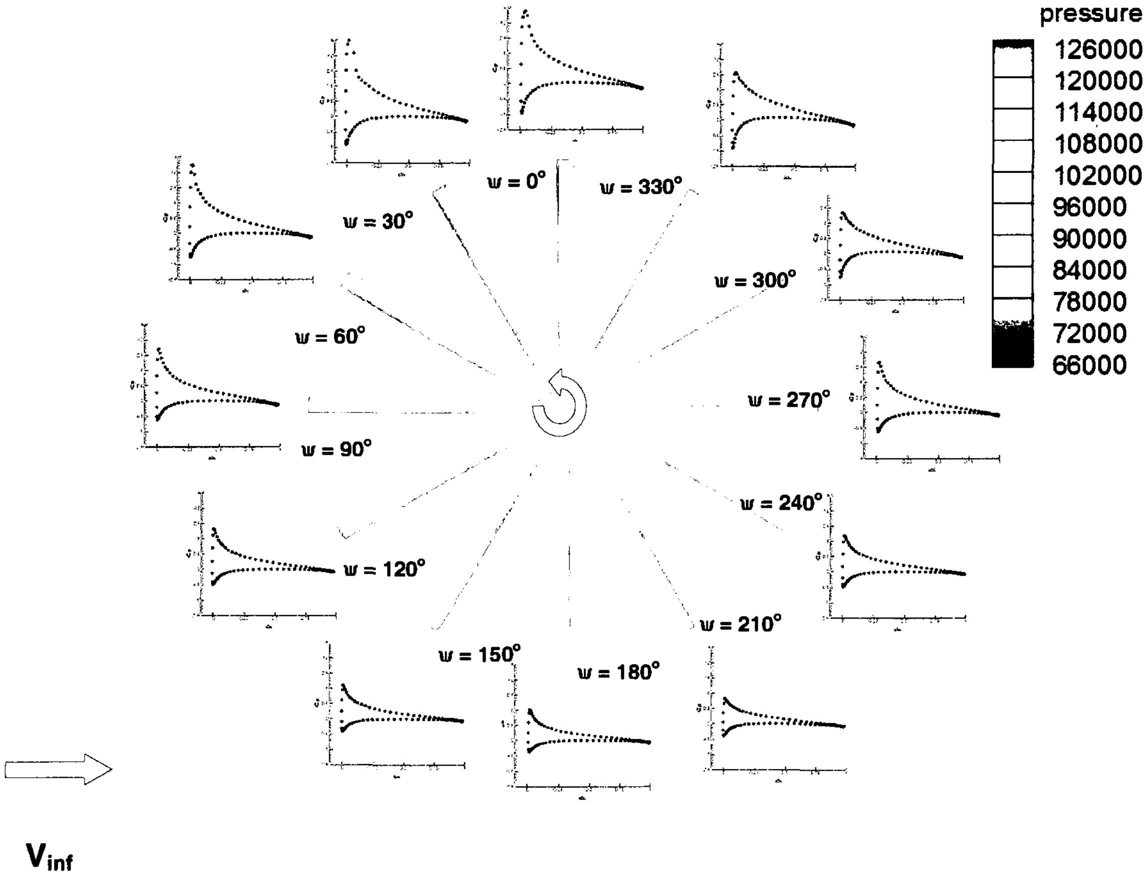

Figure 6.25: Surface pressure contours and C_p distributions (r/R=0.89) at different azimuth angles, Spalart–Allmaras, forward flight, η=0.2, M_{tip}=0.52, α=8°

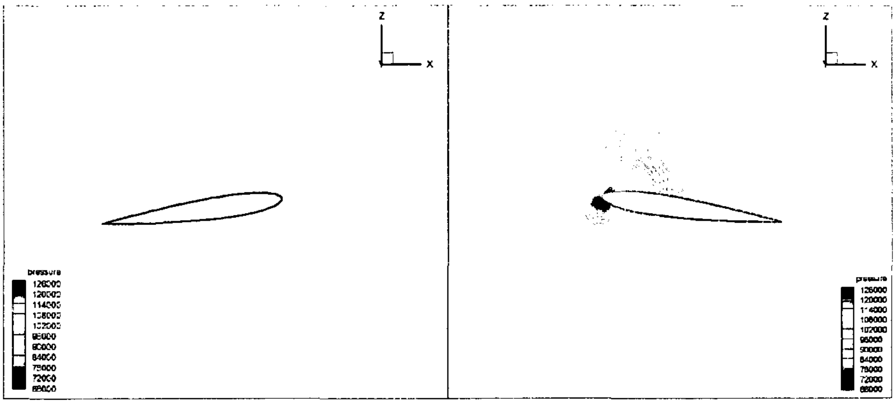

Figure 6.26: Pressure contours at r/R=0.89, left; retreating blade, right; advancing blade, Spalart–Allmaras, forward flight, η=0.2, M_{tip}=0.52, α=8°

As expected, pressure differences displayed in figure 6.27, produce the lift on the advancing blade as it reaches the maximum level at $\Psi = 0^\circ$ (advancing blade). The effect of forward flight speed can be easily observed. Pressure difference on the blade reaches the minimum level at $\Psi = 180^\circ$. The change in the pressure difference is observed in the pressure distributions at different azimuth angles.

In Figure 6.26, pressure contours at r/R=0.89 on retreating and advancing blades have been presented. In Figures 6.27-6.30, pressure contours at different advance ratios have been presented. As the forward flight speed increases, the change in the pressure on the advancing blade (leading edge) can easily be observed.

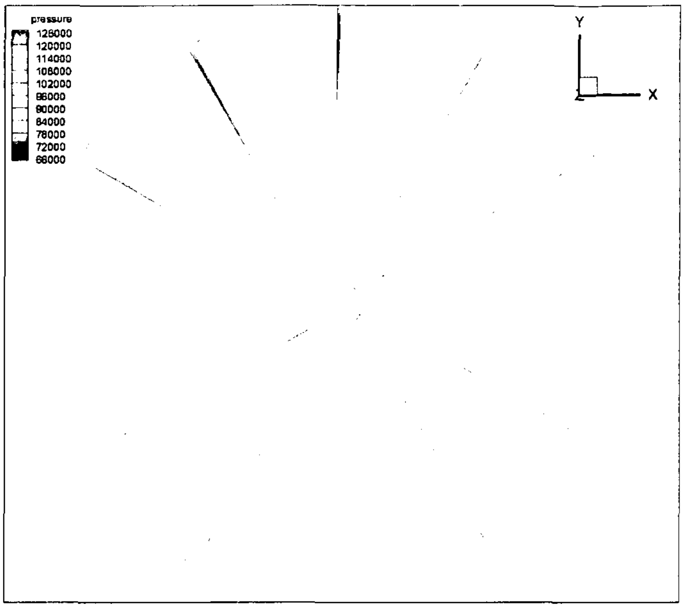

Figure 6.27: Pressure contours on the rotor, Spalart–Allmaras, Forward Flight, $\eta=0.3$, $M_{tip}=0.52$, $\alpha=8^\circ$

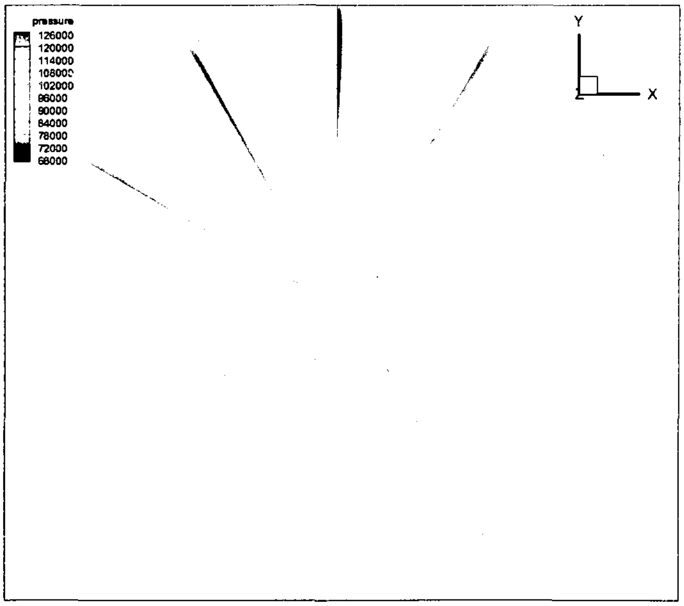

Figure 6.28: Pressure contours on the rotor, Spalart–Allmaras, forward flight, $\eta=0.4$, $M_{tip}=0.52$, $\alpha=8^\circ$

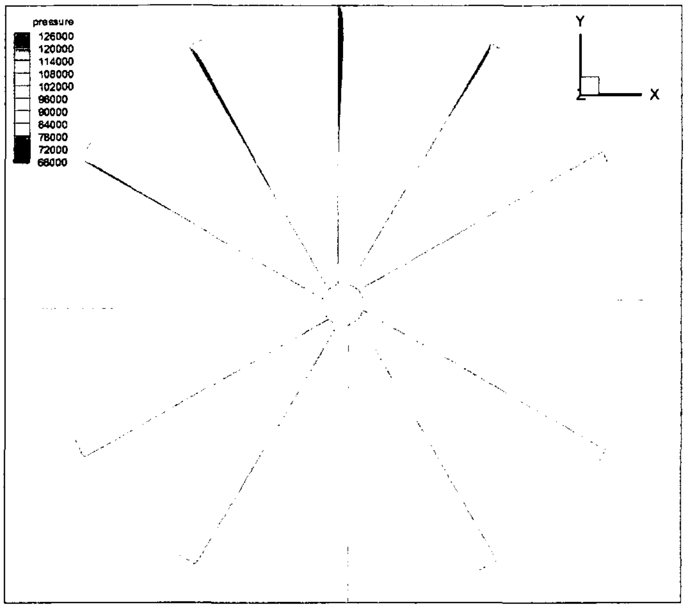

Figure 6.29: Pressure contours on the rotor, Spalart–Allmaras, forward flight, $\eta=0.5$, $M_{tip}=0.52$, $\alpha=8^\circ$

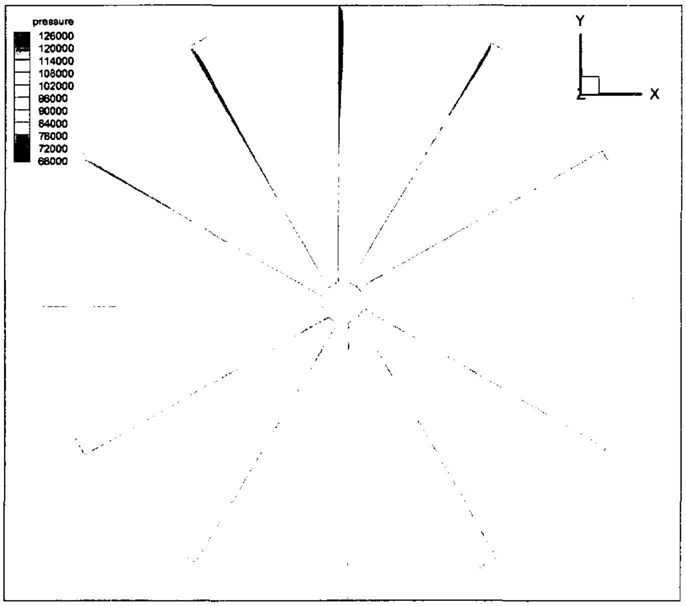

Figure 6.30: Pressure contours on the rotor, Spalart–Allmaras, forward flight, $\eta=0.6$, $M_{tip}=0.52$, $\alpha=8^\circ$

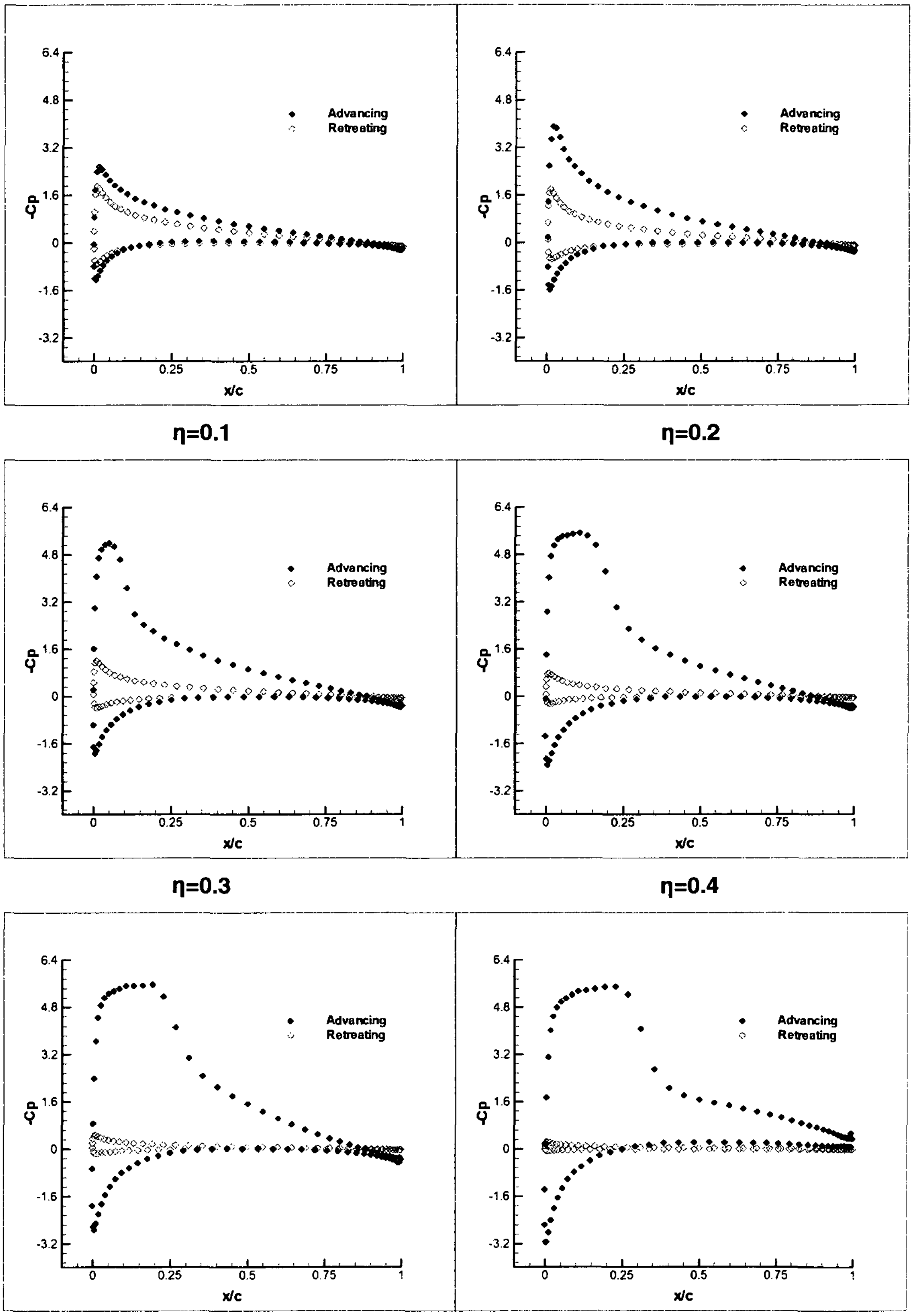

η=0.1

η=0.2

η=0.3

η=0.4

η=0.5

η=0.6

Figure 6.31: Pressure coefficient distributions on advancing and retreating blades.

In Figure 6.31, pressure coefficient distributions at r/R=0.80 on both advancing and retreating blades have been presented in order to compare lift produced by the blades. As one can easily observe, in the first case where η=0.1, the difference in the lift produced by the advancing and retreating blades is not so much. There is still an aerodynamic symmetry. However, as the advance ratio (forward flight speed) increases, the difference in the lift becomes higher and aerodynamic dissymmetry develops. This is the reason why the conventional helicopters cannot reach higher forward flight speeds. Coaxial rotor configurations have been proposed to get rid of this problem. In the following section, results of the simulations for coaxial rotors will be presented.

6.3 COAXIAL ROTOR SIMULATIONS

The coaxial configuration helicopter is so special due to the fact that it embodies a principle of the reactive moment compensation fundamentally different from that of the single-rotor configuration. To compensate for the reactive moment of the single-rotor helicopter's main rotor, there should be developed the tail rotor's side force applied to the airframe, while the coaxial-rotor helicopter has its rotors' reactive moments compensating each other directly in their axis of rotation. This removes the need for any additional forces. Rotors' reactive moments are compensated automatically throughout the flight, thus requiring no interference on the part of the pilot. A peculiarity of the coaxial rotor featuring zero reactive moment in the balanced flight is the fact that the pilot's operating the pedals creates disparity between the upper and lower engines' reactive moments with the resulting summary reactive moment being used as the direction control capability.

The reactive moment compensation method employed in the single-rotor helicopter requires the pilot's constant attention to adjusting the tail rotor's side force to maintain the helicopter's balance throughout the flight, thus putting the helicopter at a certain disadvantage. As far as power is concerned, the coaxial helicopter has a considerable edge over its single-rotor counterpart, since all free power is transferred to the rotor drive, i.e. used for developing the lift, while the single-rotor helicopter's tail rotor power consumption accounts for 10-12% of total power.

Another important feature of the coaxial configuration is revealed when the helicopter is hovering. The upper rotor race grows considerably narrower in the lower rotor plane, which allows the lower rotor to suck in additional air thus increasing the rotor race cross-section and reduces the power used for developing the lift. The contra-rotation of coaxial rotors leads to significant reduction in power, which is required for swirling the jet. Flight-testing as well as other experimental data shows the coaxial rotors to be 6-10% more efficient as compared to the single-rotor helicopter. The coaxial configuration allows the helicopter, while being smaller and lighter than the single-rotor one, to feature important tactical advantage.

The coaxial-rotor helicopter's reduction in size and different weight distribution along the airframe results in considerable reduction in longitudinal and directional moments of inertia. This is fundamental for providing the required controllability of the helicopter. Aerodynamic symmetry is the most important feature of the coaxial helicopter. It enhances its controllability and stability substantially. With the progress in helicopters, designers have repeatedly turned to symmetric aerodynamic configurations, understanding well the importance of aerodynamic symmetry for achieving the ease of controlling the helicopter. Aerodynamic symmetry of the coaxial configuration is provided by the lack of reactive moment on the airframe, relatively close upper and lower rotors and their beneficial mutual effect, which results in little difference in their thrusts when balanced. Rotors' side forces in different directions balance each other with their lateral moment, which emerges due to their separation, being insignificant.

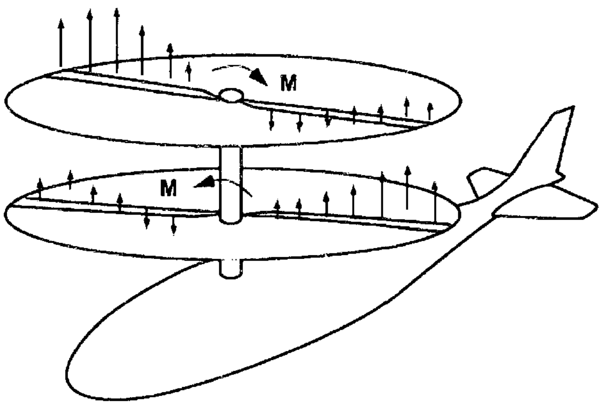

Figure 6.32: Schematic of the Advancing Blade Concept.

Owing to aerodynamic symmetry, the coaxial-rotor helicopter has literally no relation between the longitudinal and lateral movement. However, it has independent control, ease of flying it and is easy to master by any pilot irrespective of his flying skills. Aerodynamic symmetry changes the helicopter dramatically. The lack of flight mode variables, yaw moment and side force on the airframe, as well as the lack of a relation between the change in power (collective pitch) and directional and lateral control, improves the coaxial helicopter's stability and controllability. Due to this, flight safety enhances and flying in extreme condition gets easier, which is especially true as far as low-altitude flying, small landing pads, broken terrain, high barometric altitude and systems' failure are concerned. Controlling the coaxial-rotor helicopters is as simple as flying initial training aircraft. At the same time, as far as their stability, controllability and maneuverability are concerned, they could give their single-rotor rivals a run for their money.

The flat turn is a purely combat maneuver ensuring the directing of the static weapon towards the target in the shortest time possible. This makes the bulky ring mount unnecessary while gaining valuable time in turning at high angles to boot. The lack of the tail rotor enables the coaxial helicopter to use all the advantages of its directional control and develop high yawing rates with no restrictions while maneuvering. Though single-rotor helicopters boast greater available directional control moment, that moment cannot be employed in full, which is especially true for the sharp step control input. This is due to the restrictions on the yaw rate caused by tail rotor and transmission strength considerations, insufficient strength of the tail boom and the considerations given to maintaining controllability should the tail rotor get into the vortex ring. On the assumption of the above, the lack of the tail rotor allows the helicopter to be controlled in the horizontal plane by hitting the pedals fast, which results in faster turning at the required angle. Due to the invariability of the directional control margin coupled with variations in the hovering altitude up to the hover ceiling, this capability turns up to be a significant tactical advantage vital to winning the duel.

Boasting greater control efficiency and power, the coaxial-rotor helicopter enters the dive with better efficiency and greater safety. The point is when entering the dive, the controls are pushed forward with the resulting drop in vertical g-load, curving of the trajectory and increase in the airframe's angular speed in diving. When negating this angular speed by pulling the controls to go into the steady dive, the rotor blades' flapping motion increases faster than the air-frame angular speed changes. If this is accompanied by insufficient change of the angular speed due to inefficiency of the longitudinal control (like that of single-rotor helicopters), the collision of the tail boom and rotor blades is possible as a result of their conflicting movement. Thus, the efficiency and power of the coaxial helicopter's longitudinal control ensures more efficient and safe maneuvering accompanied by a decrease in vertical g-loading.

After considering all these advantages of coaxial rotor configurations, there seems to be a need to better understand the flowfield around coaxial rotors. In the present study, two features of coaxial rotor flows have been investigated. First, it is intended to verify the expected aerodynamic symmetry in forward flight at different forward flight speeds. This process has been conducted by comparing the lift (i.e., pressure difference between upper and lower surfaces) at equal symmetric span wise stations on lower (advancing, ψ=0) and upper (retreating, ψ=180) surfaces. Second, the effect of rotor separation difference, H/D (the ratio of distance between upper and lower rotors to the rotor diameter), on lift has been investigated.

6.3.1 NUMERICAL METHOD OF SOLUTION

The simulations have been performed by employing unsteady, density-based solver with implicit dual-time-stepping scheme (2nd order of accuracy). The third order MUSCL (Monotone Upstream-Centered Schemes for Conservation Laws) scheme has been applied for spatial discretization. Spalart–Allmaras turbulence model has been utilized for all coaxial rotor simulations. The mesh has been rotated with an angular velocity which corresponds to relevant case tip Mach number, M_{tip}=0.52. A uniform computational time step of $\delta t=1\times10^{-5}$ (e.g., 1046 steps for 1 revolution, Ω=60 rad/s) has been used in the simulations.

6.3.2 MESH GENERATION FOR COAXIAL ROTORS

As in the generation of grids for the single rotor simulations, the structured blocks consist of hexahedral cells around the rotors. The structured blocks are H-type in stream wise and span wise directions while it is O-type in normal direction. There are 41x41x41 grid points in stream wise, span wise and normal directions, respectively. For coaxial rotor simulations, three structured blocks have been generated for each rotor.

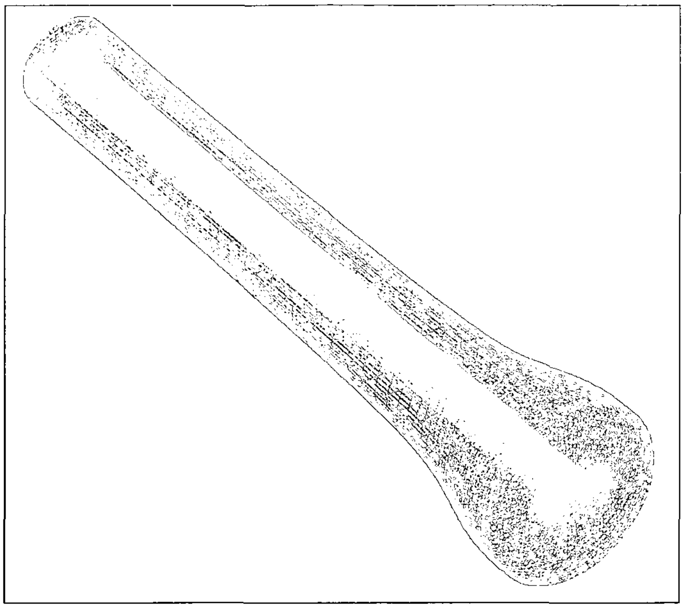

Figure 6.33: Structured block around blade.

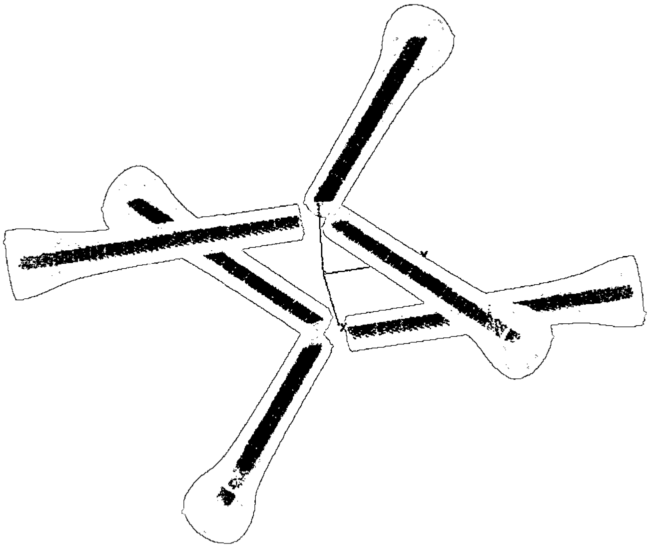

Figure 6.34: Structured blocks around lower and upper rotor blades.

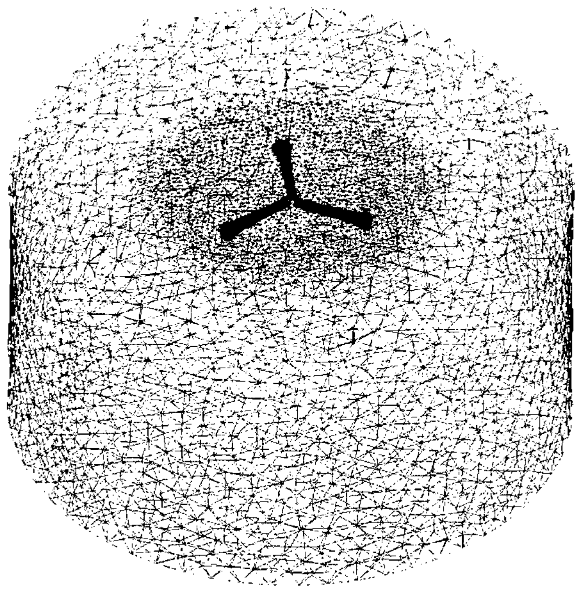

Figure 6.35: Hybrid block for lower rotor.

In the next step, the rotors have been placed in the lower and upper blocks. The rest of the block domain has been filled with tetrahedral, prismatic, and pyramid elements. Each hybrid block consists of 432,000 hexahedral and 864,000 mixed cells (total 1,045,109 cells).

The upper and lower rotors have been rotated in opposite directions. While the lower rotor (and its block) has been rotated in the counter clockwise direction with an angular velocity of Ω=60 rad/s, the angular velocity of upper rotor (block) has been set to -60 rad/s. This rotation has been achieved via moving and sliding mesh techniques.

In the sliding mesh technique two or more cell zones are used. (If one generates the mesh in each zone independently, one would need to merge the mesh files prior to starting the calculations). Each cell zone is bounded by at least one "interface zone" where it meets the opposing cell zone. The interface zones of adjacent cell zones are associated with one another to form a "grid interface." The two cell zones move relative to each other along the grid interface. During the calculations, the cell zones slide (i.e., rotate or translate) relative to one another along the grid interface in discrete steps. As the rotation or translation takes place, node alignment along the grid interface is not required. Since the flow is inherently unsteady, a time-dependent solution procedure is required.

To compute the interface flux, the intersection between the interface zones is determined at each time step. The resulting intersection produces one interior zone (a zone with fluid cells on both sides) and one or more periodic zones. If the problem is not periodic, the intersection produces one interior zone and a pair of wall zones, which is empty if the two interface zones intersect entirely. Therefore, these wall zones are changed to another appropriate boundary type. The resultant interior zone corresponds to where the two interface zones overlap and the resultant periodic zone corresponds to where they do not. The number of faces in these intersection zones varies as the interface zones move relative to one another. The fluxes across the grid interface are computed using the faces resulting from the intersection of the two interface zones, rather than from the interface zone faces themselves. The surface between lower and upper blocks has been defined as "interface" and divided into two parts. The interior part has more surface grid points since the crucial part of the data transfer is performed at this region.

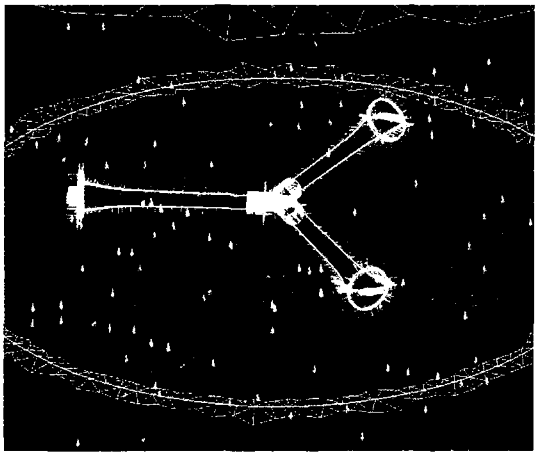

Figure 6.36: Lower and upper rotors and inner interface surface between rotor blocks.

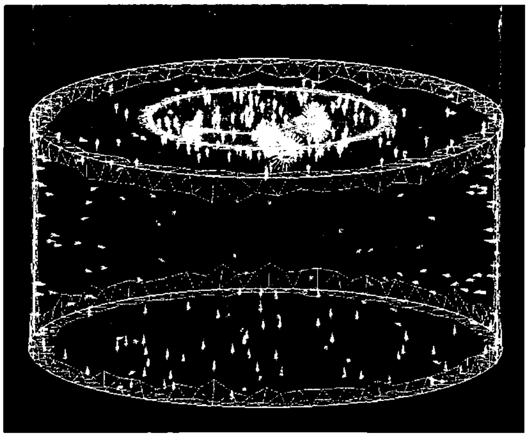

Figure 6.37: Inner and outer parts of interface surface.

6.3.3 COAXIAL ROTOR IN FORWARD FLIGHT

Once a single-rotor helicopter is in forward flight, a phenomenon manifests itself, called dissymmetry of lift, which possesses the potential to disrupt stable flight at speed. Dissymmetry of lift imposes an upper speed limit (known as the Never-Exceed Speed or V_{NE}) upon single-rotor helicopters, by virtue of the fact that during one rotation of the rotor disc, a rotor blade experiences, in extreme parts of the flight envelope, two widely contrasting unstable conditions. On one side (the advancing side) of the rotor disc, rotor blades travel through the air sufficiently quickly for the airflow over them to become transonic or even supersonic, which causes fundamental changes in the airflow over the rotor blades, while on the other (retreating) side of the rotor disc, the rotors travel through the air much more slowly, possibly slowly enough to enter the stall condition, thus failing to produce lift. Both aerodynamic régimes result in (frequently catastrophic) flight instability.

Coaxial rotors solve the problem of dissymmetry of lift because one set of rotors is cancelled by the corresponding increased lift on the same side of the other set of rotors, and vice versa, resulting in a helicopter that can fly, theoretically at least, faster than a single-rotor design, and more stably in extreme parts of the flight envelope.

As mentioned above, the most important superiority of coaxial rotor configuration against conventional (single rotor) rotor configuration is the high forward speed achieved via balanced lift by counter rotating lower and upper rotors. In this section, verification of aerodynamic symmetry proposed by coaxial rotor design has been intended.

For this purpose, the hybrid grid generated for L3 (H/D=0.2) case has been utilized. The angular velocity of lower and upper rotors have been set to $\Omega_{low}=60$ rad/s and $\Omega_{upp}=-60$ rad/s, respectively. Six forward flight cases have been performed by setting the advance ratio (η) to 0.1, 0.2, 0.3, 0.4, 0.5, 0.6 and 0.7. Figures 6.38–6.44 display the pressure contours at different time steps for 7 different advance ratios. In Figure 6.45, the comparison of the results for 6 different advance ratio cases is presented.

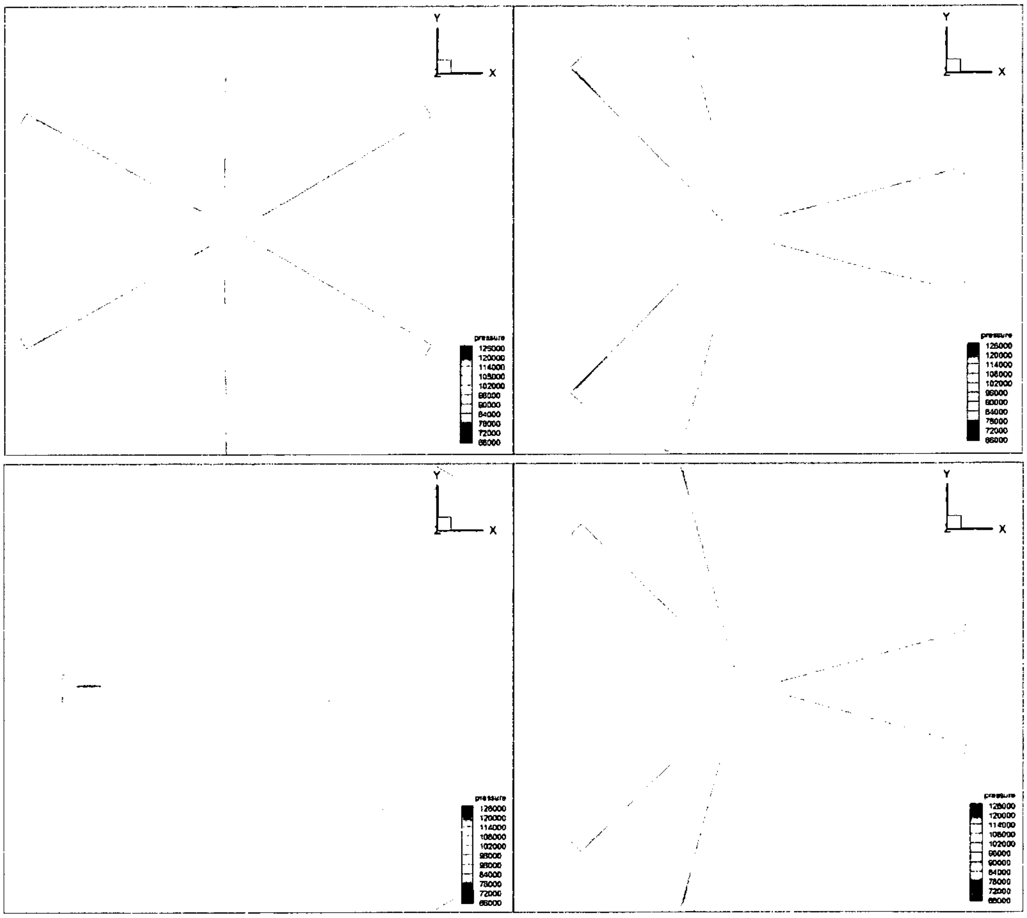

Figure 6.38: Pressure contours on the lower and upper rotors at different time steps, forward flight, η=0.1, M_{tip}=0.52, Spalart–Allmaras.

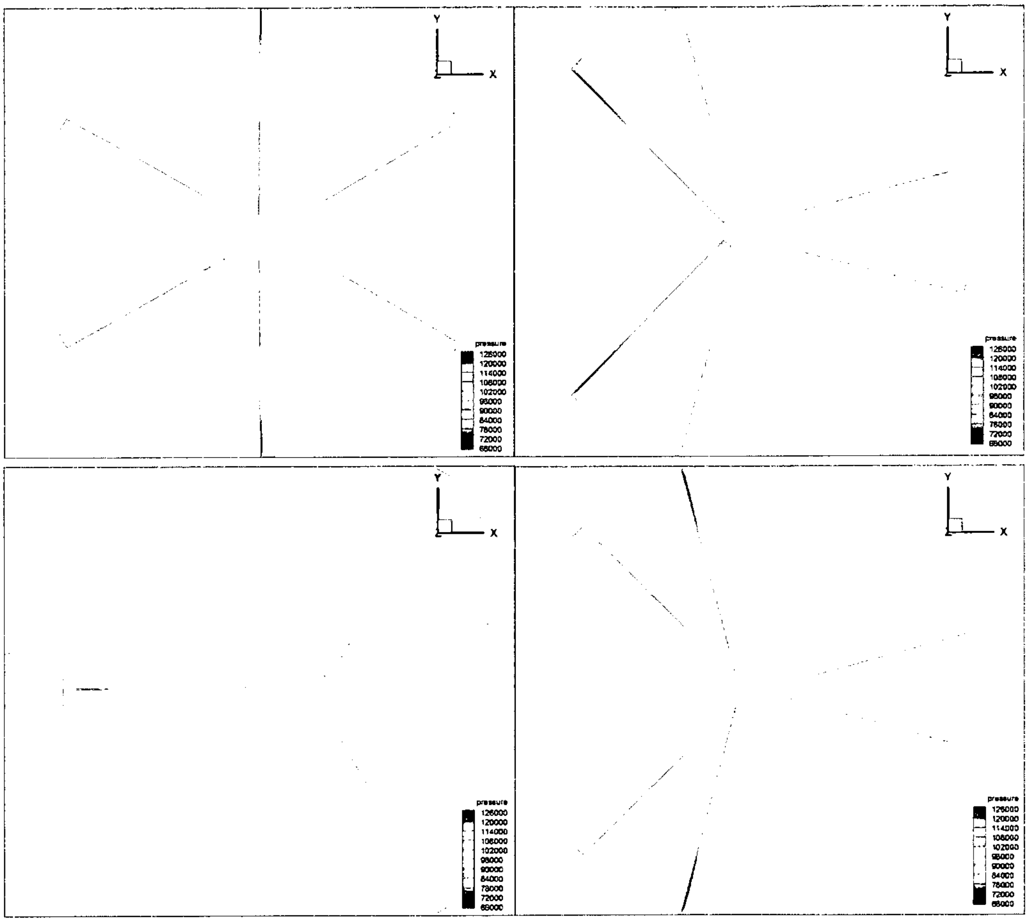

Figure 6.39: Pressure contours on the lower and upper rotors at different time steps, forward flight, η=0.2, M_{tip}=0.52, Spalart–Allmaras.

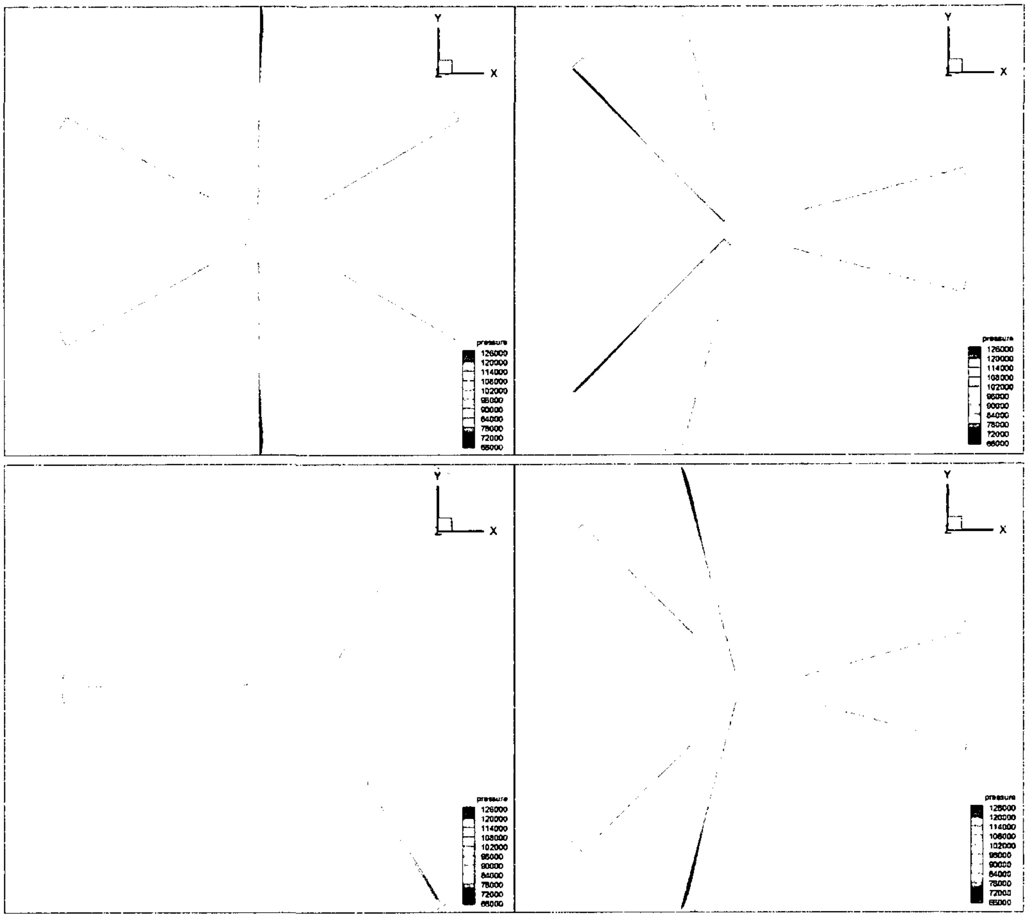

Figure 6.40: Pressure contours on the lower and upper rotors at different time steps, forward flight, η=0.3, M_{tip}=0.52, Spalart–Allmaras.

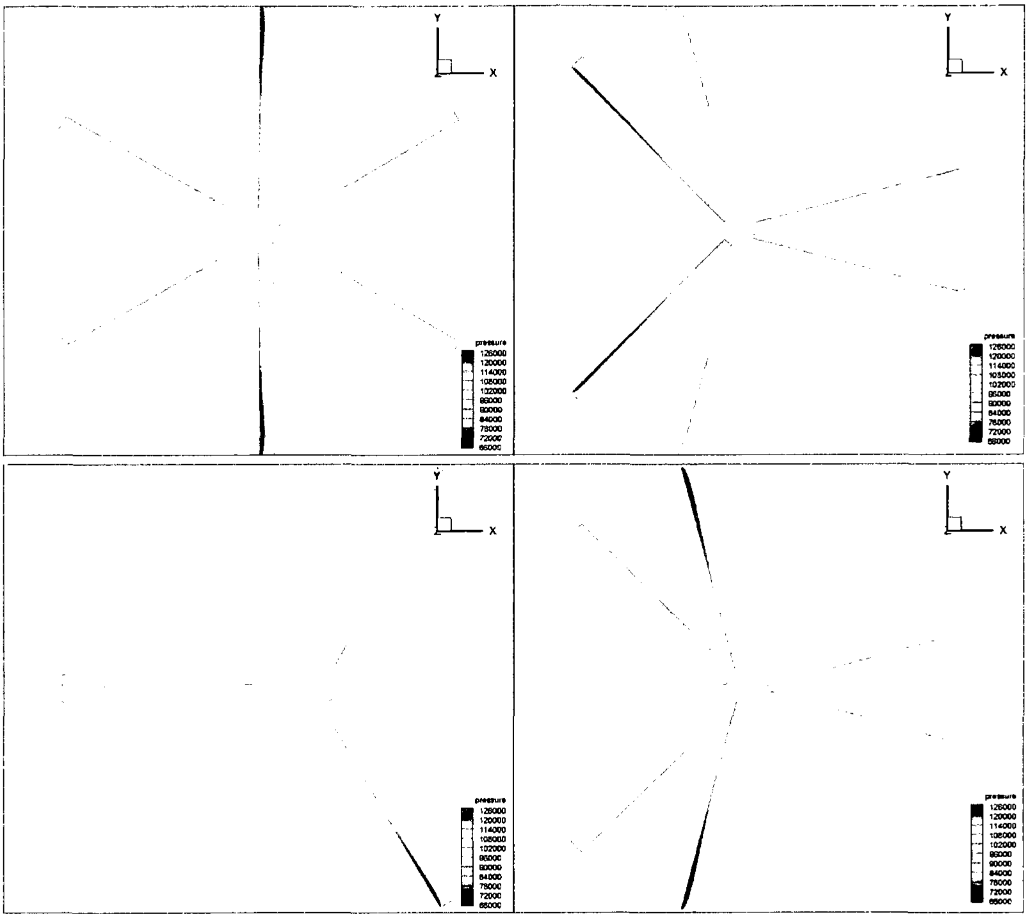

Figure 6.41: Pressure contours on the lower and upper rotors at different time steps, forward flight, η=0.4, M_{tip}=0.52, Spalart–Allmaras.

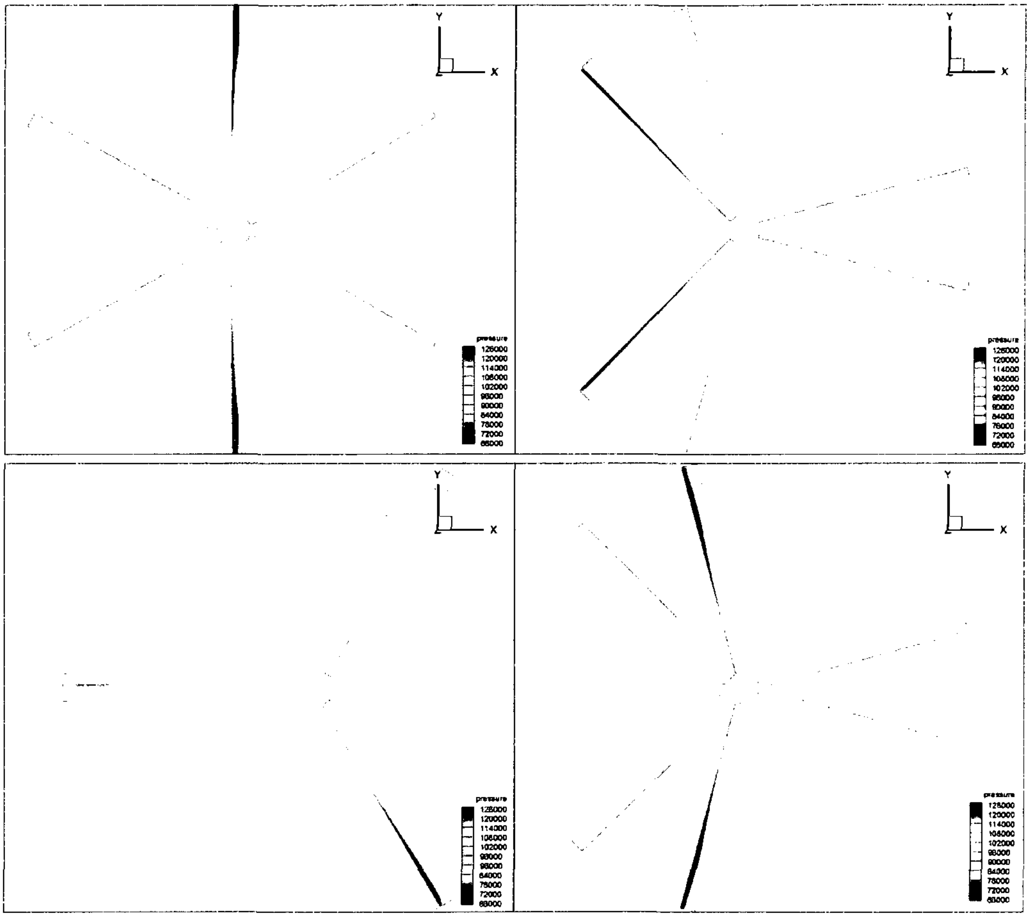

Figure 6.42 Pressure contours on the lower and upper rotors at different time steps, forward flight, η=0.5, M_{tip}=0.52, Spalart–Allmaras.

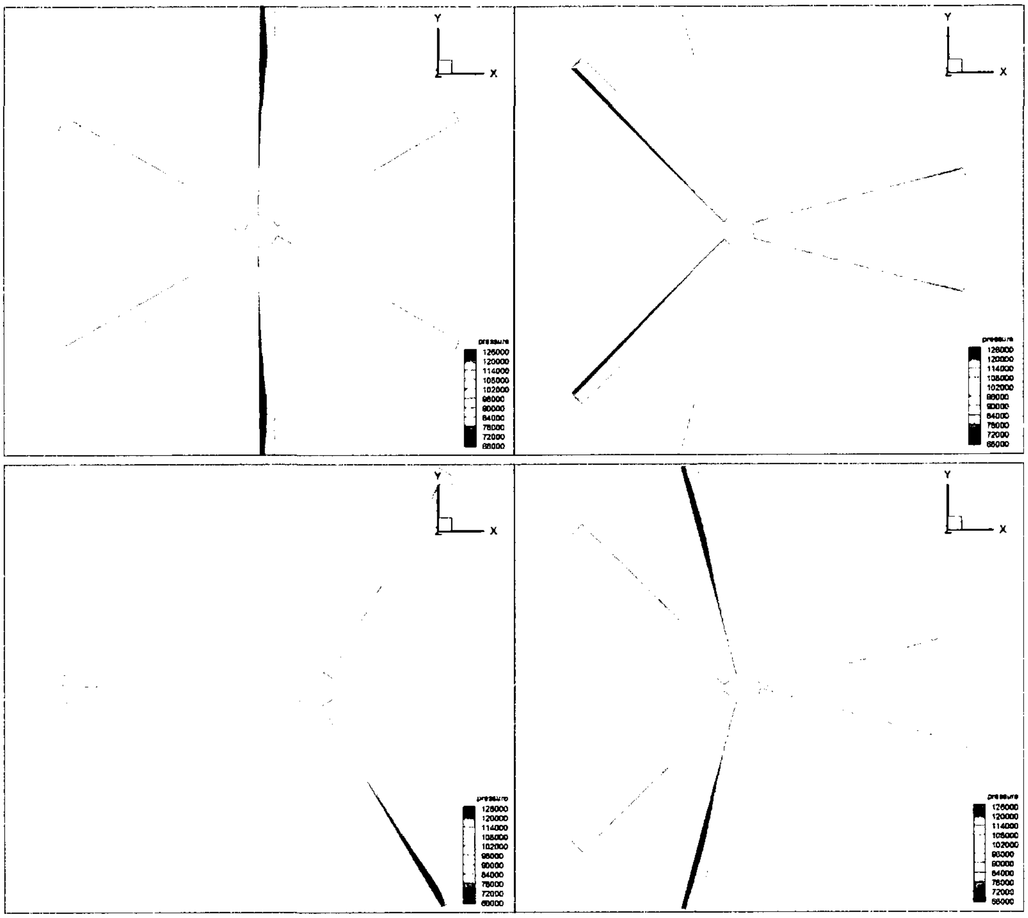

Figure 6.43: Pressure contours on the lower and upper rotors at different time steps, forward flight, η=0.6, M_{tip}=0.52, Spalart–Allmaras.

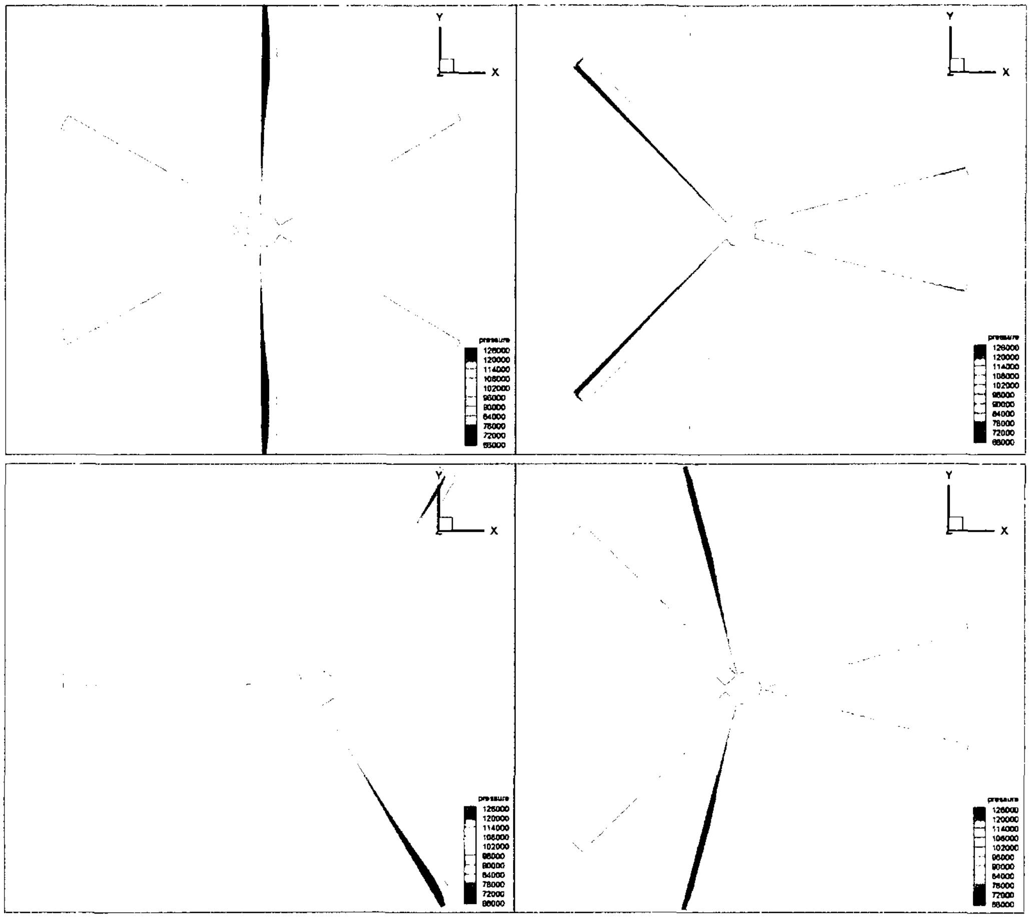

Figure 6.44 Pressure contours on the lower and upper rotors at different time steps, forward flight, $\eta=0.7$, $M_{tip}=0.52$, Spalart–Allmaras.

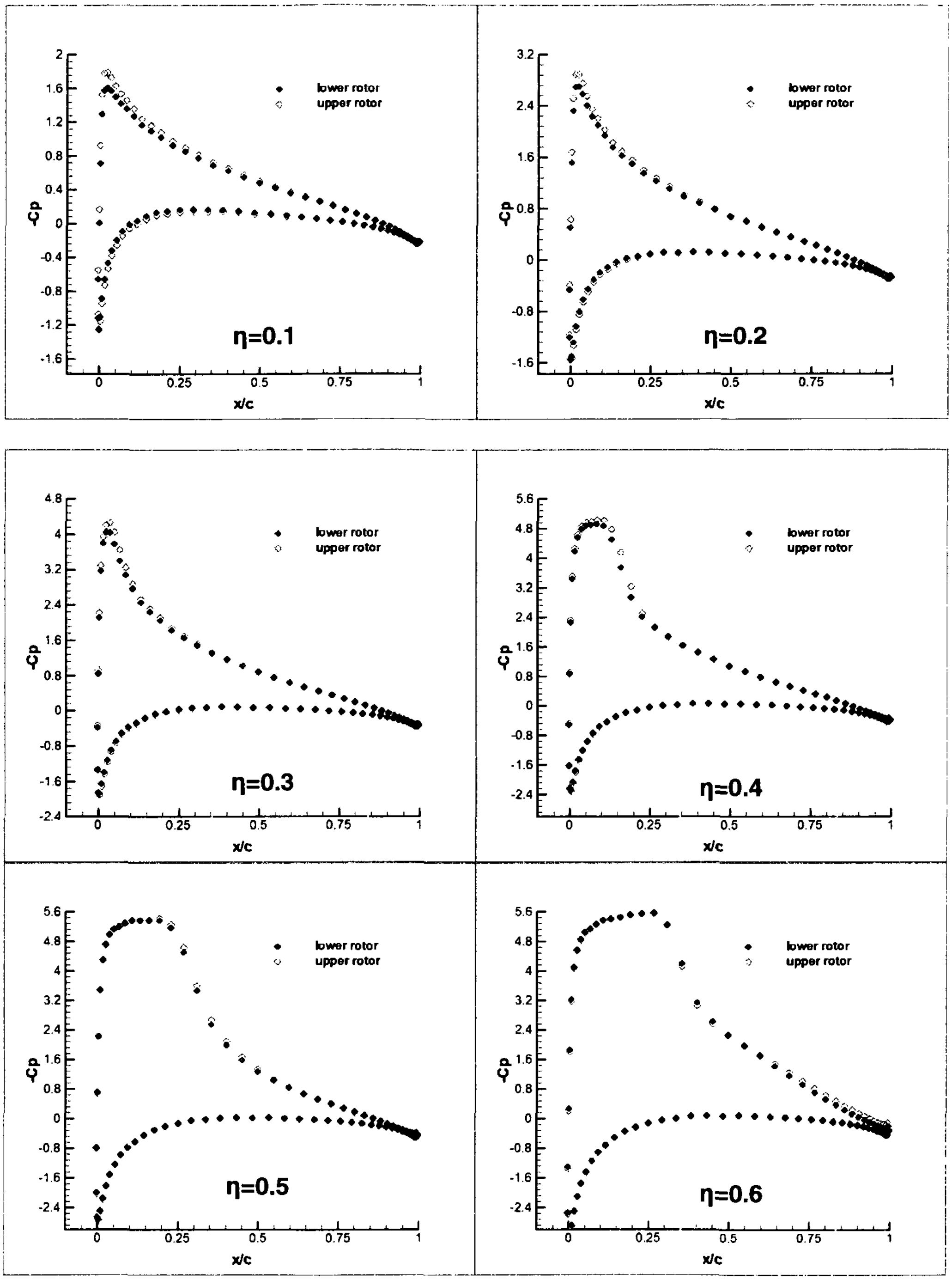

Figure 6.45: Pressure coefficient distributions at r/R=0.80 on the lower and upper rotors, forward flight, M_{tip}=0.52, Spalart–Allmaras.

In Figures 6.38-6.44, the effect of increasing the forward speed can easily be observed. The figures show the instantaneous pressure contours at $t=t_0+t_1$ (up, left), $t=t_0+t_2$ (up, right) $t=t_0+t3$ (low, left) and $t=t_0+t_4$ (low, right). At $t=t_0+t_1$, an aerodynamic symmetry has been observed for each forward speed case. In Figure 6.45, a comparison of the section pressure coefficient distributions have been displayed. Pressure values on the lower and upper rotor surfaces are almost equal. Therefore, it may be concluded that aerodynamic symmetry has been achieved by the coaxial rotor configuration in different forward flight speeds.

6.3.4 EFFECT OF ROTOR SEPARATION DISTANCE ON LIFT

In this section of the present study, the effect of the rotor separation distance on the lift produced by the upper and the lower rotors has been investigated. For this purpose, five grids with different rotor separation distances have been generated. Simulations have been performed for these five H/D values (0.18, 0.19, 0.20, 0.21 and 0.22).

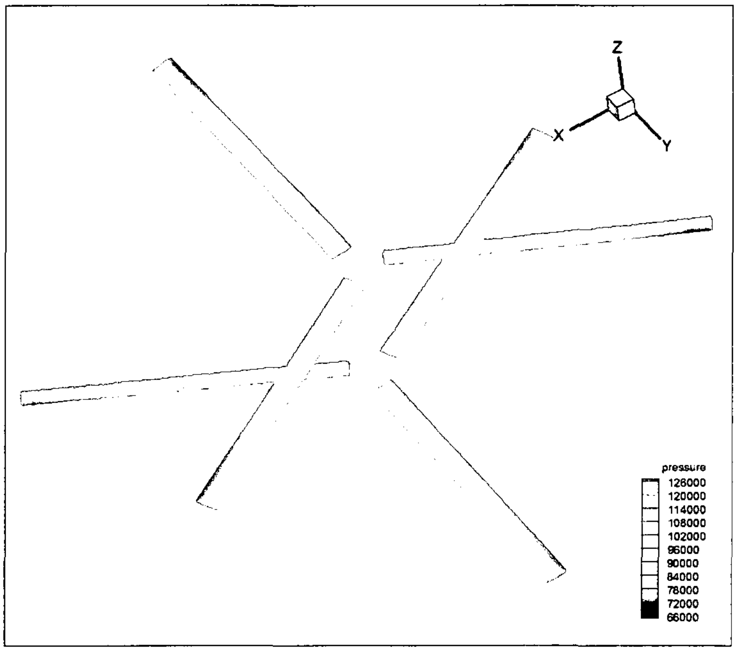

Figure 6.46: Pressure contours on the upper and lower rotors, hover, H/D=0.18.

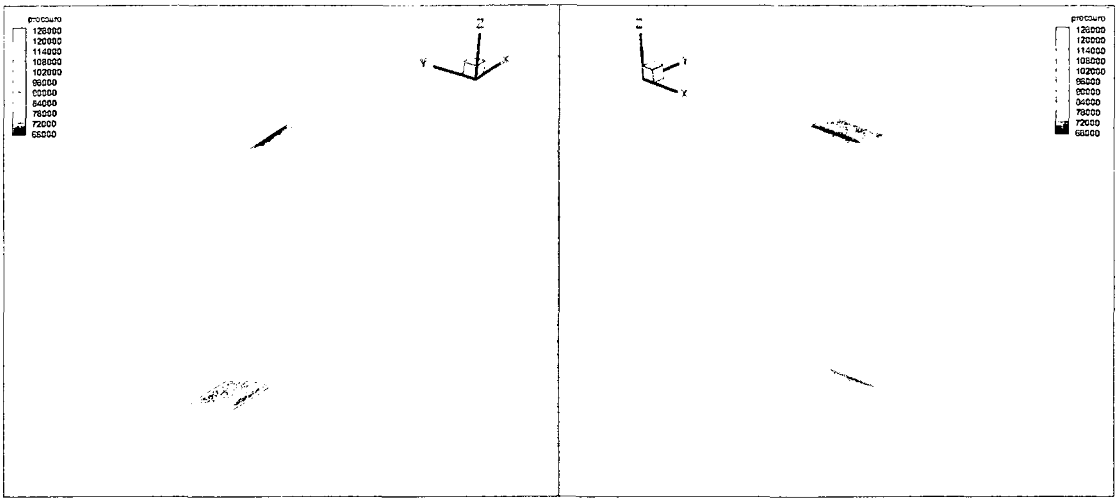

Figure 6.47: Pressure contours at r/R=0.89, left; ψ=90°, right; ψ=270°, H/D=0.20.

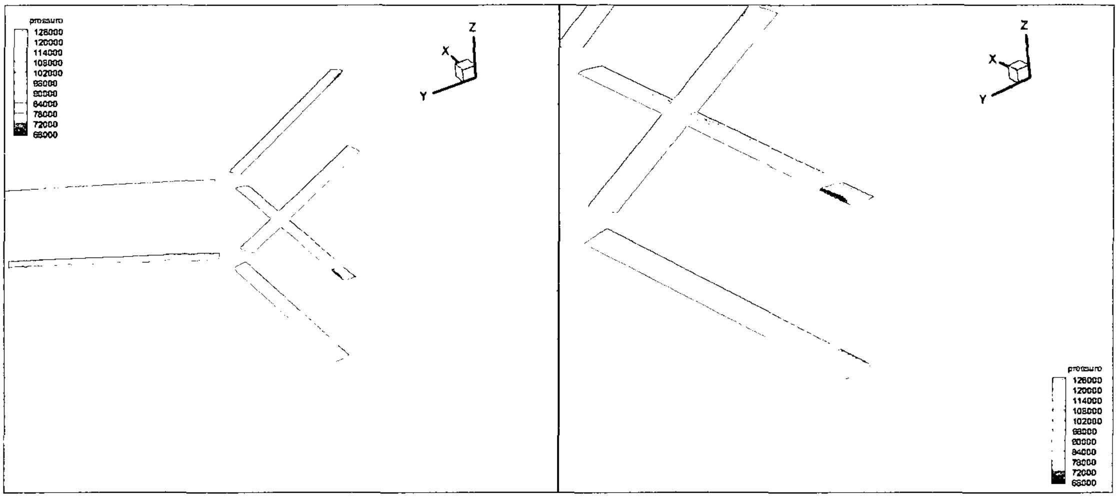

Figure 6.48: Interaction between the upper and lower rotors; pressure contours at r/R=0.89, ψ=270°, H/D=0.20.

Figures 6.46 and Figure 6.47 display the interaction between the upper and lower rotors for H/D=0.20 case.

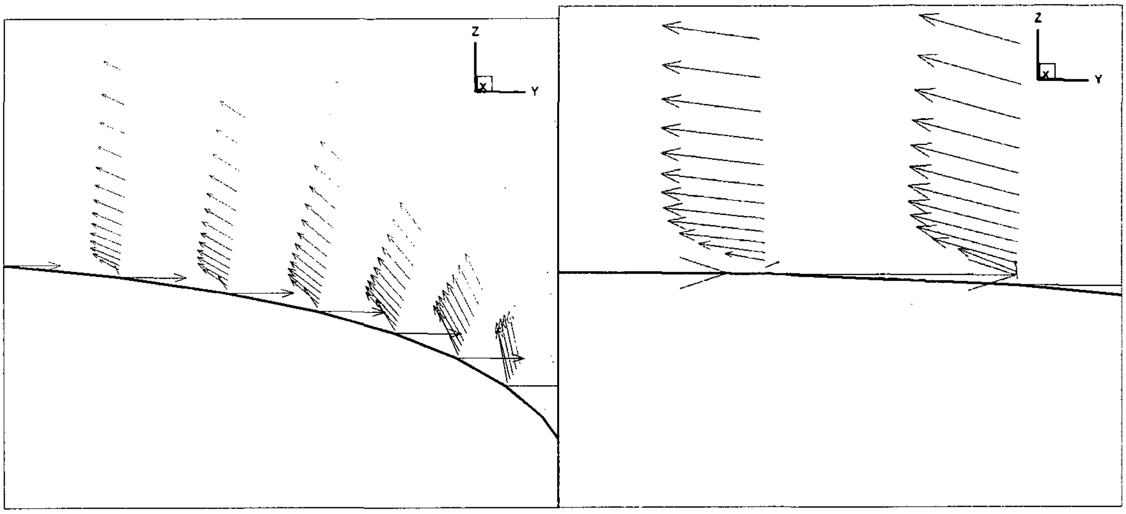

Figure 6.49: Development of the boundary layer, r/R=0.89, ψ=270°

Several hover experiments carried out in 1965 at the United Aircraft Research Laboratories (UARL) studied the collective rotor spacing and the inter-rotor phase angle. It was concluded that rotor spacing had little effect on the performance although only two different rotor separation distance values were tested.

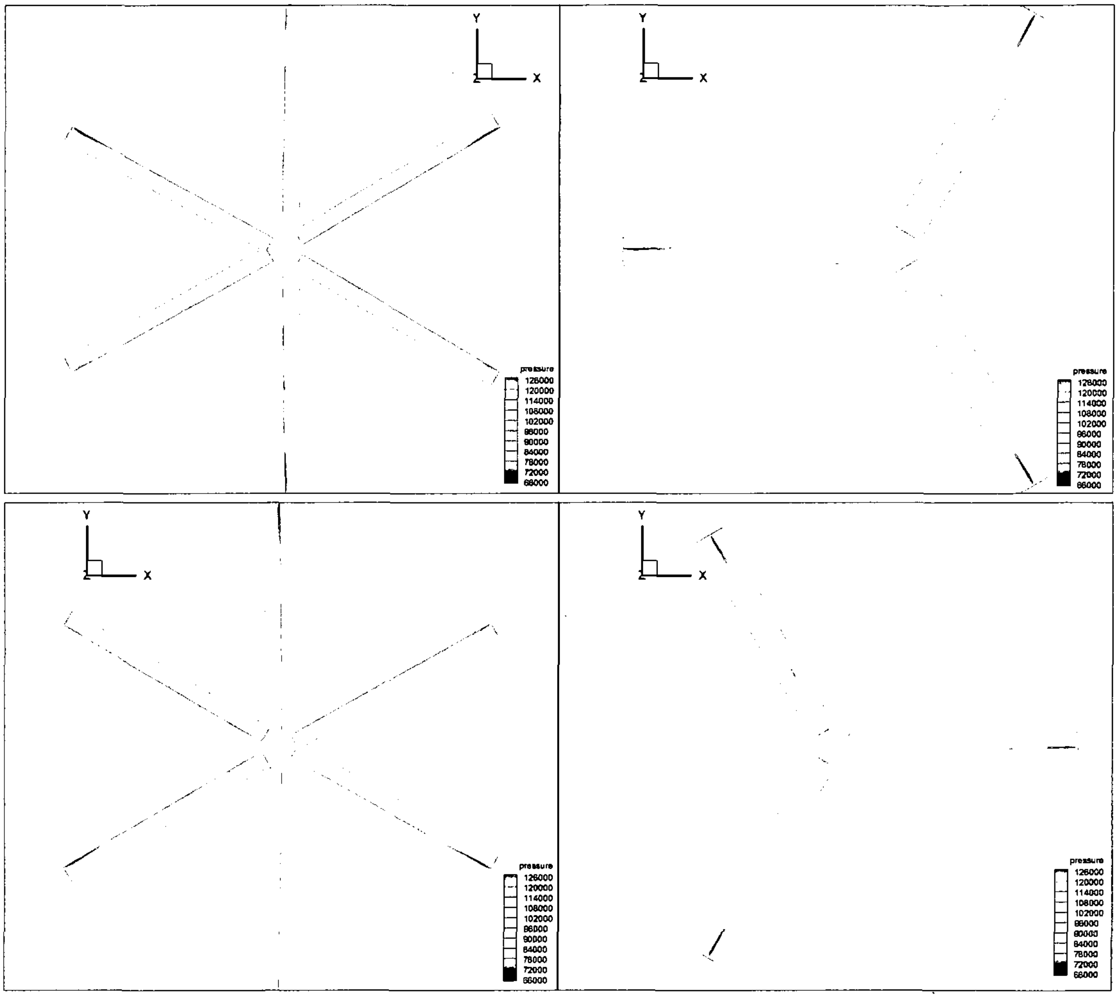

Figure 6.50: Pressure contours at different time steps, hover, M_{tip}=0.52, Spalart–Allmaras, H/D=0.22.

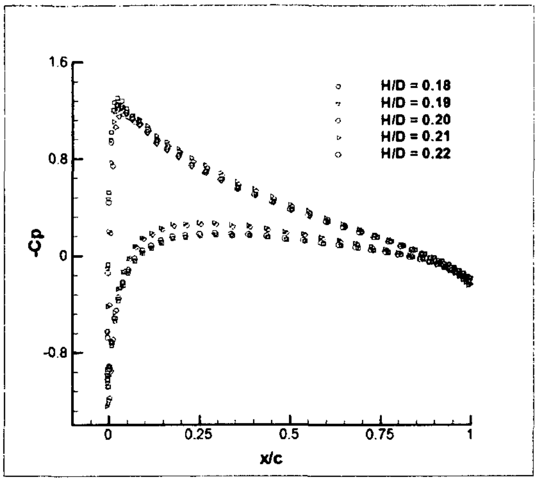

Figure 6.51: Comparison of pressure coefficient distributions on the lower surface for five H/D values, hover, M_{tip}=0.52, Spalart–Allmaras.

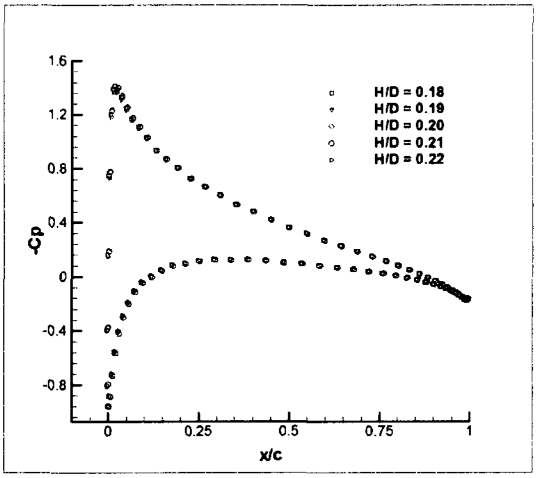

Figure 6.52: Comparison of pressure coefficient distributions on the upper surface for five H/D values, hover, M_{tip}=0.52, Spalart–Allmaras.

Figure 6.51 displays the pressure coefficient distributions on lower surface for 5 H/D values. No significant difference has been observed between the pressure values on the lower surface. However, there seems to be a small difference for H/D = 0.20 and 0.21 cases. In Figure 6.52, a comparison of pressure coefficient distributions on the lower surface for five H/D values is presented. On the upper surface, the pressure values seem to be identical for all the tested H/D cases.

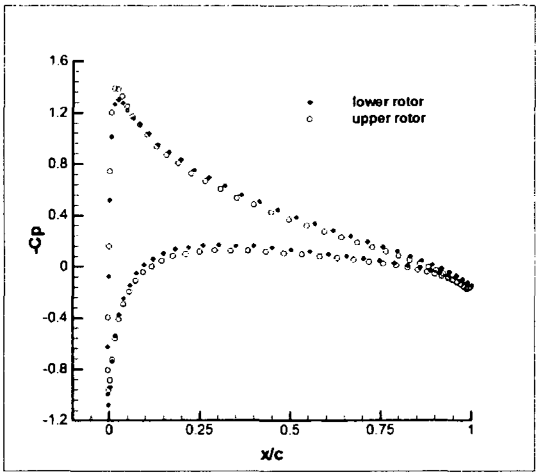

Figure 6.53: Pressure coefficient distributions on the upper and lower rotors, H/D=0.1, hover, M_{tip}=0.52, Spalart–Allmaras.

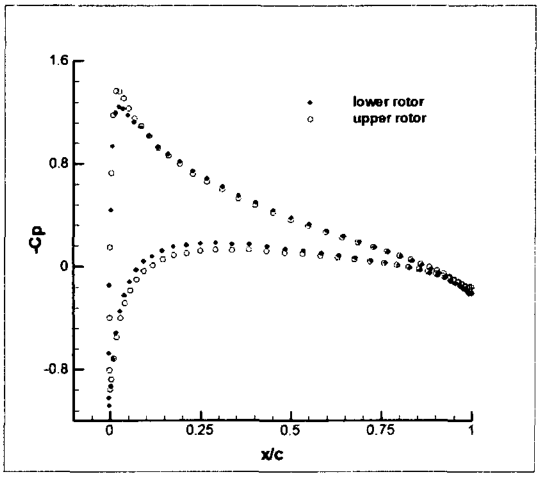

Figure 6.54: Pressure coefficient distributions on the upper and lower rotors, H/D=0.5, hover, M_{tip}=0.52, Spalart–Allmaras.

In Figures 6.53 and 6.54, pressure values on lower and upper surfaces are compared for H/D=0.1 and H/D=0.5 values. These results seem to suggest that the change in the H/D value does not have a significant effect on the lift produced. This is consistent with the findings of the experimental study of Ref. 61.

CHAPTER VII

CONCLUSIONS AND RECOMMENDATIONS

7.1 CONCLUSIONS

A framework for rotorcraft analysis has been developed, validated and utilized for the prediction of aerodynamics of single and coaxial helicopter rotors. The framework has been based on the unsteady solution of the three-dimensional, compressible, Navier-Stokes equations expressed in a rotating frame of reference. The computations have been carried out by solving the governing equations on hybrid grids around single and coaxial rotor configurations. To reduce the computational time and memory requirements, parallel processing with distributed memory has been employed.

The simulations have been performed by employing unsteady, density–based (that is, compressible) solver with implicit, dual–time–stepping scheme (2nd order accurate). The third-order MUSCL scheme has been applied for spatial discretization. The mesh and its block have been rotated with an angular velocity which corresponds to a case-specific tip Mach number, M_{tip}. A uniform computational time step of $\delta t=1x10^{-5}$ has been decided upon and used in all the computations. At 3rd revolution, limiting cycle is deemed as attained. The conclusions that can be drawn from the present study are presented next.

1. In order to understand the suitability of the model and its solver for the problem at hand, a series of comparisons have been obtained between the results and previously published results. Initially, unstructured grids have been used for the validation cases. For this purpose, unstructured meshes of different sizes, with volume cell numbers ranging from 1 million to 6 million, have been tested. However, the outputs obtained by using unstructured grids have not

been satisfactory. It has been concluded that unstructured grids used in computations are not suitable for the present problems. Therefore, the decision has been made to try hybrid meshes, which indeed have produced successful results. The validation cases have been designed so to compare with the experimental data obtained by Caradonna and Tung in 1981. Inviscid then laminar viscous results have been obtained where the C_p values at three span wise stations have been compared. It has been concluded that the overall agreement with the experimental data has been deemed satisfactory. Subsequently, the decision has been made that the modeling framework is robust and can be used for more complicated cases.

2. To decide on the suitable turbulence model to be employed in the simulations, various turbulence models have been tested: Spalart-Allmaras, standard k–ε, RNG k–ε, realizable k–ε, standard k-ω, shear-stress transport (SST) k-ω, and large eddy simulation (LES) models. Among the models that have produced successful results, only Spalart-Allmaras is a one-equation model. Since that would translate into being computationally the most efficient, the Spalart-Allmaras model has been chosen to be utilized in the subsequent simulations.

3. For the single-rotor simulations, a series of four-digit NACA profiles (0012, 2112, 2712, 4112, 4712, 6212, 6612) have been considered for the blade geometry. The intention has been to investigate and compare the lift forces generated by these airfoil sections in the generated rotational flows. The C_p distributions at three span wise stations have been computed for the angle of attack values at $\alpha=0^\circ$ and $\alpha=8^\circ$. It has been observed that as the camber increases, the lift increases. The airfoil section, which has the highest camber, that is, NACA 6612, appears to be the most effective profile for both at $\alpha=0^\circ$ and $\alpha=8^\circ$.

4. Before getting into the coaxial rotor forward flight simulations, analyzing the aerodynamic dissymmetry on forward-flying single rotors has been considered. That is, before proposing a solution, the problem needed to be observed and

studied. For this purpose, a hybrid mesh has been generated for a single rotor with NACA 0012 blade sections pitched at $\alpha=8^{\circ}$. The advance ratio has been set to six different values, $\eta=0.1$, 0.2, 0.3, 0.4, 0.5 and 0.6. It has been observed that as the advance ratio increases, the difference in the lift becomes higher and aerodynamic dissymmetry starts to develop. This is the root cause for the conventional helicopters not reaching higher forward flight speeds. Therefore, a coaxial-rotor configuration has been proposed as a solution.

5. Dissymmetry of lift imposes an upper speed limit (also known as, the Never-Exceed Speed or V_{NE}) on the single-rotor helicopters. A coaxial rotor configuration where the rotors turn in opposite directions may solve this problem. The dissymmetry generated by one rotor should be cancelled by the corresponding increased lift on the same side of the other rotor, and vice versa. This should result in a helicopter that can fly faster. One of the major objectives of the present study has been the verification of this proposal. For this purpose, the hybrid mesh generated for the L3 case (H/D=0.2) has been utilized and simulations have been performed for six different forward flight speeds. Indeed, aerodynamic symmetry has been successfully achieved for all forward flight speeds.

6. In the final part of the present study, the effect of rotor separation distance (H/D) on lift has been investigated. Five different grids have been generated by setting the H/D value to 0.18, 0.19, 0.20, 0.21 and 0.22. Then, the obtained C_p values on the upper and lower rotors have been compared. For these cases, either small or almost no effect on lift has been observed.

7.2 RECOMMENDATIONS AS FUTURE WORK

The main objective of this dissertation has been to develop a framework for investigating the flowfields around coaxial helicopter rotors. To pose a problem that is amenable to a reasonable solution verifying the direction taken, many assumptions have been made and some aspects worth studying have been omitted. The following suggestions should be considered in the next phase in order to extend the present framework achieve more realistic and higher-fidelity simulations.

1. The blades studied in the present study are assumed to be rigid, untwisted and untapered, with constant collecting and cyclic pitches. Simulating tapered and/or linearly twisting blades should be a straightforward process within the current framework.

2. A real helicopter blade is highly flexible and blade deformations are an integral part of the rotor movement. To obtain higher-fidelity results, the aeroelasticity of the rotor should be included in the model. This would require that the flow solver be coupled with a finite element solver, such as, NASTRAN, and the deformations be calculated after a certain number of time steps with either a weak or strong coupling.

4. The present investigation has been conducted for constant collective angles for both the lower and the upper rotor. Future simulations with independently changing lower and upper rotor collective angles will be helpful to better understand the aerodynamics of coaxial rotors.

5. Including the fuselage in the computational model should also have noticeable effect on the flowfield generated by the rotors. Therefore, generating a mesh for a domain that includes the rotor and the fuselage should result in more realistic simulations.

6. Generated vortices continue to roll up in regions far from the blades. Typically, however, the computational grid becomes progressively coarser for the regions away from the solid surfaces. Consequently, the simulated vortices become highly diffused due to the inevitable numerical discretization error. To reduce this diffusive property of the vortical flow simulations, "vorticity confinement method" has been proposed. In this method, a source term is

added to the Navier-Stokes equations, which effectively convects the discretization error back into the vortex center. The method has been applied to flows around helicopter rotors, and shown reasonable improvements in the vortex resolution.

7. The effect of phase shift between the two rotors on its operation has not been examined in the present study. Performing simulations of varying phase angles between the rotors should help one to design more effective coaxial rotor configurations.

8. The vertical pitch of the generated vortices per rotor revolution has not been considered in the present study. In order to minimize the BVI noise and improve aerodynamic performance, particularly for coaxial rotor configurations, such an investigation is recommended.

9. Final recommendation is for a study to analyze the effects of changing the following parameters: 1) blade number, 2) planform shape, 3) rotor solidity, and 4) section profile. Each one of these variables may substantially change, for the better or the worse, the performance of a coaxial rotor.

REFERENCES

Allen, C.B., “Parallel Simulation of Lifting Rotor Wakes in Forward Flight,” *International Journal Of Numerical Analysis And Modeling,* Volume 4, Number 1, Pages 1–15, 2007, Institute for Scientific Computing and Information.

Ananthan, S., Leishman, J. G., and Ramasamy, M., “The Role of Filament Stretching in the Free-Vortex Modeling of RotorWakes,” American Helicopter Society 58th Annual National Forum, Montreal, Canada, June 11–13, 2002.

Anikin, V. A., “Aerodynamic Feature of a Coaxial Rotor Helicopter,” Proceedings of the 17th European Rotorcraft Forum, Sept. 1991.

Antopov, V. F. et al., “Eksperimental’nyye Issledovaniya Po Aerodinamike Vertoleta (Experimental Research on Helicopter Aerodynamics),” Moscow, *Mashinostroyeniye*, 1980 (in Russian).

Baysal, O., Fouladi, K., and Lessard, V.R., “Multigrid and Upwind viscous Flow solver on 3-D Overlapped and Embedded Grids,” *AIAA Journal,* Vol. 29, No. 6, June 1991, pp. 903-910.

Berkman, M.E., and Sankar, L.N, “A Navier–Stokes/Full Potential/Free Wake Method For Advancing Multi-Bladed Rotors,” *American Helicopter Society 53rd Annual Forum,* Virginia Beach, Virginia, April 29-May 1, 1997.

Bermes, C., Sartori, K., Schafroth, D., Bouabdallah, S., and Siegwart, R., “Control of a Coaxial Helicopter with Center of Gravity Steering,” *Workshop*

Proceedings of SIMPAR 2008, pp. 492-500, Intl. Conf. on Simulation, Modeling And Programming for Autonomous Robots, Venice(Italy), Nov 3-4,2008.

Boelens, O.J., Van der Ven, H., Oskam, B., and Hassan, A.A., "Accurate and efficient vortex-capturing for a helicopter rotor in hover," National Aerospace Laboratory NLR-TP-2000-420.

Boisard, R., and Baeder, J. D., "Impact of Three-Dimensional and Compressible Effects of Blade Loading on BVI Noise Signature," American Helicopter Society 57th Annual National Forum, Washington D.C, May 9-11 2001.

Brown, R.E., and Line, A.J., "Efficient High-Resolution Wake Modeling Using the Vorticity Transport Equation," *AIAA Journal,* Vol. 43, No. 7, July 2005.

Brown, R.E., and Leishman, R.G, "Blade Twist Effect On Rotor Behavior in the Vortex Ring State," European Rotorcraft Forum, Bristol, England, September 17–20, 2002.

Burton, T., Sharpe, D., Jenkins, N., and Bossanyi, E., Wind Energy Handbook, John Wiley & Sons, Ltd., 2001.

Burger, C., and Hartfield, R., "Wind Turbine Airfoil Performance Optimization using the Vortex Lattice Method and a Genetic Algorithm," *AIAA 2006-4051,* 4th AIAA Energy Conversion Engineering Conference 26–29, June 2006, San Diego, CA.

Cao, Y., Yu, Z., and Su, Y. "A Coupled Free Wake–CFD Method for the Simulation of Helicopter Rotor Flow," *Canadian Aeronautics and Space Journal,* Vol. 48, No. 4, December 2002.

Caradonna, F. X., and Tung, C., "Experimental and Analytical Studies of a Model Helicopter Rotor in Hover," NASA Technical Memorandum 81: 232, September 1981.

Cheney, M.C., "The ABC Helicopter," AIAA/AHS VTOL Research, Design and Operations Meeting, Atlanta, GA., February 17–19, 1969.

Chow, J.S., Zilliac, G.G., and Bradshaw, P., "Mean and Turbulence Measurements in the Near Field of a Wingtip Vortex," *AIAA Journal,* Vol. 35, No. 10, 1997.

Coleman, C.P., "A Survey of Theoretical and Experimental Coaxial Rotor Aerodynamic Research," NASA Technical Paper 3675, March 1997.

Conlisk, A.T., "Modern Helicopter Rotor Aerodynamics," *Progress in Aerospace Sciences*, 37 (2001) 419–476.

Devenport, W.J., Rife, M.C., Liapis, S.I., and Follin, G.J., "The Structure and Development of a Wing-tip Vortex," *Journal of Fluid Mechanics,* Vol. 312, 1996.

Dingledein, R. C., "Wind-Tunnel Studies of the Performance of Multi-rotor Configurations," *NACA TN-3236, Aug. 1954.*

Doerffer, P., and Szulc, O., "Numerical Simulation of Model Helicopter Rotor in Hover," *Task Quarterly,* 12 No 3, 227–236.

Filippone, A., Chollet, J.P., and Lewandowska, J., "CFD Actuator Disk Solutions For A Helicopter Rotor In Hover Flight," DESS Modelisation & Simulation en Mécanique Département Mécanique Université, Joseph Fourier, Grenoble, France and Mechanical, Aerospace and Manufacturing Engineering Department, University of Manchester Institute of Science and Technology, United Kingdom, September 2003.

Fluent 6.3 User's Guide, © Fluent Inc. 2006-09-20.

Geçgel, M., Parallel, Navier–Stokes Computation of the Flow field of a Hovering Helicopter Rotor Blade, M.S. Thesis, Middle East Technical University, Ankara, Turkey, 2003.

Gregory, N., and Wilby, P.G., "NPL 967 and NACA 0012, A Comparison of Aerodynamic Data," *Royal Ministry of Defense Aeronautical Council Current Papers*, C.P. No: 1261.

Green, S.I., Fluid Vortices, Kluwer Academic Publishers, 1995.

Hahn, S., Ananthan, S., Iaccarino, G., Baeder, J.D., and Moin, P., "Coupled URANS Simulation For The MDART Rotor In Forward Flight," Center for Turbulence Research Annual Research Briefs 2007.

Hahn, S., Duraisamyy, K., and Iaccarino, G., "Coupled High–Fidelity URANS Simulation for Helicopter Applications," Center for Turbulence Research Annual Research Briefs 2006.

Harrington, R. D., "Full-Scale-Tunnel Investigation of the Static-Thrust Performance of a Coaxial Helicopter Rotor," NACA TN-2318, Mar. 1951.

Hazra, S.B., "An Efficient Method for Aerodynamic Shape Optimization," AIAA 2004-4628, 10th AIAA/ISSMO Multidisciplinary Analysis and Optimization Conference, 30 August-1 September 2004, Albany, New York.

Hirsch, C., Numerical Computation of Internal and External Flows, Vol.2, John Wiley & Sons, 1988.

Hussain M.M., Mehdi, S.N., and Reddy, P.R., “CFD Analysis of Low Speed Vertical Axis Wind Turbine with Twisted Blades,” *International Journal of Applied Engineering Research*, Volume 3, Number 1 (2008), pp. 149–159.

Jacquin, L., and Pantano, C., “On the Persistence of Trailing Vortices," *Journal of Fluid Mechanics,* Vol. 471, 2002.

Joncheray, P., “Aerodynamics of Helicopter Rotor in Hover: The Lifting-Vortex Line Method Applied to Dihedral Tip Blades,” *Aerospace Science and Technology,* 1997, No. 1, 17-25.

Kalkhoran, I.M., Wilson, D.R, and Seath, D.D., “Experimental Investigation of the Perpendicular Rotor Blade-Vortex Interaction at Transonic Speeds,” *AIAA Journal,* Vol. 30, No. 3, March 1992.

Kim, H.W., and Brown, R., “Modelling the Aerodynamics of Coaxial Helicopters–from an Isolated Rotor to a Complete Aircraft,” Springer Proceedings in Physics, Proceedings of the EU-Korea Conference on Science and Technology, 2008, Vol.124, Pages: 45-59.

Krothapalli, K. R., Prasad, J. V. R., and Peters, D. A., “Helicopter Rotor Dynamic Inflow Modeling for Maneuvering Flight,” *Journal of the American Helicopter Society,* Vol. 46, No. 2, 2001.

Le Pape, A., and Beaumier, P. “Numerical Optimization of Helicopter Rotor Aerodynamic Performance in Hover,” *Aerospace Science and Technology,* 9 (2005) 191–201.

Leishman, J.G., Principles of Helicopter Aerodynamics, Cambridge University Press, 2006.

Leishman, J. G., "Aeroacoustics of 2-D and 3-D Blade Vortex Interaction Using the Indicial Method," American Helicopter Society 52nd Annual Forum, Washington, DC,, June 4–6, 1996.

Leweke, T., Meunier, P., Laporte, F., and Darracq, D., "Controlled Interaction of Co-rotating Vortices," Proc. 3rd ONERA-DLR Symposium, 2001.

Lim, J., and Tung, C., "2GCHAS Predictions of HART Blade-Vortex Interaction Loading," Proceedings of the AHS Technical Specialists' Meeting for Rotorcraft Acoustics and Aerodynamics, Williamsburg, VA, October 28–30, 1997.

Lorber, P., McCormick, D., Anderson, T., Wake, B., and MacMartin, D., "Rotorcraft Retreating Blade Stall Control," AIAA 2000–2475, Fluids 2000 Conference and Exhibit, 19-22 June 2000, Denver, Colorado.

Mahalingam, R., Structure of the Near Wake of a Rotor in Forward Flight and its Effect on Surface Interactions, Ph.D. Dissertation, School of Aerospace Engineering, Georgia Institute of Technology, June 1999.

Mahalingam, R., and Komerath, N.M., "Measurements of the Near Wake of a Rotor in Forward Flight," AIAA Paper 98-0692, January 1998.

O'Brien Jr., D.M., and Smith, M.J., "Analysis of Rotor-Fuselage Interactions Using Various Rotor Models," AIAA 2005-0468, AIAA 43rd Aerospace Sciences Meeting Reno, NV January 10-13, 2005.

Park, Y.M., Nam, H.J., and Kwon, O.J. "Simulation of Unsteady Rotor-Fuselage Interactions Using Unstructured Adaptive Meshes," American Helicopter Society 59th Annual Forum, Phoenix, Arizona, May 6-8, 2003.

Pomin, H., and Wagner, S., "Navier–Stokes Analysis of Helicopter Rotor Aerodynamics in Hover and Forward Flight," *Journal of Aircraft,* 39 (5), 813–821, Presented as Paper 2001–0998 at the AIAA 39th Aerospace Sciences Meeting & Exhibit, Reno, NV, January 2001.

Potsdam, M., Yeo, H., and Johnson, W. "Rotor Airloads Prediction Using Loose Aerodynamic/Structural Coupling," American Helicopter Society 60th Annual Forum, Baltimore, MD, June 7–10, 2004.

Prasad, J. V. R., Zhao, J., and Peters, D. A., "Helicopter Rotor Dynamic Wake Distortion Models for Maneuvering Flight," 28th European Rotorcraft Forum, Bristol, UK, September 17-20 2002.

Prasad, J. V. R., Franciullo, T., Zhao, J., and Peters, D. A., "Toward a High Fidelity Inflow Model for Maneuvering and In-Ground Effect Flight Simulation," American Helicopter Society 57th Annual Forum, Washington D.C., May 9-11 2001.

Qin, J.H., Numerical Simulations of a Turbulent Axial Vortex, Ph.D. Thesis, Department of Aerospace Engineering, Purdue University, 1998.

Quaranta, G., Bindolino, G., Masarati, P., and Mantegazza, P., "Toward a Computational Framework for Rotorcraft Multi-Physics Analysis: Adding Computational Aerodynamics to Multibody Rotor Models," 30th European Rotorcraft Forum Marseilles, France, September 14–16 2004.

Ragab, S. and Sreedhar, M., "Numerical Simulations of Vortices with Axial Velocity Deficits," *Physics of Fluids,* Vol. 7, 1995.

Rahier, G., and Delrieux, Y., "Influence of Vortex Model on Blade-Vortex Interaction Load and Noise Predictions," Proceedings of the AHS Technical Specialists' Meeting for Rotorcraft Acoustics and Aerodynamics, Williamsburg, VA, October 28–30, 1997.

Ramaswamy, M., Johnson, B., and Leishman, J.G., "Toward Understanding the Aerodynamic Efficiency of a Hovering Micro-Rotor," American Helicopter Society International Specialists Meeting on Unmanned Rotorcraft, January 23–25, 2007, Phoenix, AZ.

Ramaswamy, M., and Leishman, J. G., "The Interdependence of Straining and Viscous Diffusion Effetcs on Vorticity in Rotor Flow Fields," American Helicopter Society 59th Annual National Forum, Phoenix, Arizona, May 6–8, 2003.

Ringler, T. D., George, A. R., and Steele, J. B., "The Study of Blade-Vortex Interaction Sound Generation and Directionality," Proceedings of the AHS Technical Specialists Meeting, Philadelphia, PA, October 1991.

Sheffer, S.G., Alonso, J.J., Martinelli, L., and Jameson, A., "Time-Accurate Simulation of Helicopter Rotor Flows Including Aeroelastic Effects," AIAA, Aerospace Sciences Meeting & Exhibit, 35th, Reno, NV, Jan. 6-9, 1997.

Schmitz, F.,H., and. Sim, B. W.C., "Acoustic phasing, directionality and amplification effects of helicopter blade-vortex interactions," *Journal of the American Helicopter Society,* vol. 46, pp. 273–282, October 2001.

Schmitz, F.H., and Yu, Y.H., “Helicopter impulsive noise: Theoretical and experimentalstatus,” *Journal of Sound and Vibration,* vol. 109, no. 3, pp. 361–442, 1986.

Shinoda, P.M., Yeo, H., and Norman, T.R., “Rotor Performance of a UH-60 Rotor System in the NASA Ames 80- by 120-Foot Wind Tunnel,” American Helicopter Society 58th Annual Forum, Montreal, Canada, June 11-13, 2002.

Sim, B.W-C., Schmitz, F.H., and Aoyama, T., “Radiation and Directionality Characteristics of Advancing Side Blade-Vortex Interaction (BVI) Noise," AIAA/CEAS 6th Aeroacoustics Conference, Hawaii, 2000.

Singh, K.P., Newman, J.C., III, and Baysal, O., “Dynamic Unstructured Method for Flows Past Multiple Objects in Relative Motion,” *AIAA Journal,* Vol. 33, No. 4, Apr. 1995, pp. 641-649.

Srinivasan, G.R., Baeder, J.D., Obayashi, S., and McCroskey, W.J. “Flowfield of a Lifting Hovering Rotor–A Navier-Stokes Simulation,” NASA Technical Memorandum 102862, 1990.

Srinivasan, G.R., Raghavan, V., and Duque, E.P.N., “Flowfield Analysis of Modern Helicopter Rotors in Hover by Navier–Stokes Method,” International Technical Specialist Meeting, Rotorcraft Acoustics and Rotor Fluid Dynamics, October 15-17, 1991, Philadelphia, Pennsylvania, USA.

Steijl, R.,Barakos, G.N, and Badcock, K.J., “A Framework for CFD Analysis of Helicopter Rotors in Hover and Forward Flight,” *International Journal For Numerical Methods in Fluids,* 2006; 51:819–847.

Strawn, R., and Biswas, R., "Computation of Helicopter Rotor Acoustics in Forward Flight," 19th Army Science Conference, 20-24 June, 1994, Orlando, Florida.

Su, Y., and Cao, Y., "A Nonlinear Inverse Simulation Technique Applied to Coaxial Rotor Helicopter Maneuvers," *Journal of Aircraft Engineering and Aerospace Technology,* 2002, Vol.74, issue:6, Page:525-533.

Tatossian, C.A., and Nadarajah, S.K., "Optimum Shape Design of Helicopter Rotors in Forward Flight via Control Theory," AIAA 2007-3951, 18th AIAA Computational Fluid Dynamics Conference 25-28 June 2007, Miami, FL

Taylor, M., "A Balsa-Dust Technique for Air-Flow Visualization And its Application to Flow Through Model Helicopter Rotors in Static Thrust," NACA TN-2220, Nov. 1950.

Usta, E., Wake, B.E., Egolf, T.A., and Sankar, L.N., "Application of a Symmetric Total Variation Diminishing Scheme to aerodynamics and Aeroacoustics of Rotors," American Helicopter Society 57th Annual Forum, Washington, D.C., May 9-11 2001.

Usta, E., Wang, G., and Sankar, L.N., "Application of a Symmetric Total Variation Diminishing Scheme to Shock Noise of Rotors," American Institute of Aeronautics and Astronautics, Copyright © 1999 by E. Usta.

Uzol, N.S., and Long, L.N., "3-D Time-Accurate CFD Simulations of Wind Turbine Rotor Flow Fields," AIAA Paper No: 2006–0394.

Vassberg, J., Gopinath, A. K., and Jameson, A., "Revisiting the Vertical-Axis Wind-Turbine Design Using Advanced Computational Fluid Dynamics," AIAA 43rd Aerospace Sciences Meeting & Exhibit, Reno, NV, AIAA Paper 2005–0047.

Vermeera, L.J, Sorensen, J.N., and Crespo, A., Wind Turbine Wake Aerodynamics, Progress in Aerospace Sciences 39 (2003) 467–510.

Vil'dgrube, L. S., "Vertolety, Raschet Integral'nykh Aerodynamicheskikh Kharakteristick i Letnomekhanicheskikh Danykh (Helicopters-Calculations of Integral Aerodynamic Characteristics and Flight-Mechanics Data)," Moscow, Mashinostroyeniye, 1977 (in Russian).

Wachspress, D.A., and Quackenbush, T.R., "Impact of Rotor Design on Coaxial Rotor Performance, Wake Geometry and Noise", American Helicopter Society 62nd Annual Forum, Phoenix, AZ, May 9-11, 2006.

Walsh, J.L., Bingham, G.J., and Riley, M.F., "Optimization Methods Applied to the Aerodynamics Design of Helicopter Rotor Blades," 26th AIAA/ASME/ASCE/AHS Structures, Structural Dynamics and Materials Conference, Orlando, Florida, April 1985.

Walsh, J.L., "Performance Optimization of Helicopter Rotor Blades," NASA Technical Memorandum 104054, April 1991.

Wenren, Y., Fan, M., Dietz, W., Hu, G., Braun, C., Steinhoff, J., and Grossman, B., "Efficient Eulerian Computation of Realistic Rotorcraft Flows Using Vorticity Confinement," AIAA 39th Aerospace Sciences Meeting & Exhibit, Reno, NV, AIAA Paper 2001–0996.

Xu, H., Zhang, S., and Khalid, M., "Numerical Simulations of Unsteady Flows Past a Four-Bladed Rotor in Forward-Flight," AIAA 17th Computational Fluid Dynamics Conference, Toronto, Canada, AIAA Paper 2005–5125.

Xu, H., and Khalid, M., "Numerical Investigation of Turbulent Flow Past a Four-Bladed Helicopter Rotor Using *k*–ω SST Model," 2nd International Bhurban Conference on Applied Sciences and Technology, Bhurban, Pakistan, June 16–21, 2003.

Yağız, B., and Aslan, A.R., "Effect of Rotor Tip Shape on Helicopter Main Rotor Performance," 11th International Symposium on Flow Visualization, August 9-12, 2004, University of Notre Dame, Notre Dame, Indiana, USA.

Yağız, B., "Analysis of the Flow Field Around Hovering Helicopter Blades with Fluent 6.1," Istanbul Technical University Rotorcraft Research and Development Center Report R280-AAA-R-04-002, March 2004.

Yang, Z., Sankar, L.N., Smith, M., and Bauchau, O., "Recent Improvements to a Hybrid Method for Rotors in Forward Flight," *Journal of Aircraft,* 39 (5), 804–812, Presented as Paper 2000-0260 at the AIAA 38th Aerospace Sciences Meeting & Exhibit, Reno, NV, January 2000.

VITA

Mr. Murat Gecgel was born on May 6, 1973 in Ankara, Turkey. He received his Bachelor of Science degree in Aerospace Engineering in August 1995 from the Turkish Air Force Academy, Istanbul, Turkey. While serving in the Air Force, he started his graduate studies on helicopter aerodynamics and flight mechanics at the Middle East Technical University, Ankara, Turkey. Mr. Gecgel conducted his research entitled "Parallel, Navier–Stokes Computation of the Flowfield of a Hovering Helicopter Rotor Blade," under the supervision of Professor Yusuf Ozyoruk. In September 2003, he received his Master of Science degree in Aerospace Engineering from the Middle East Technical University.

Mr. Gecgel was accepted to the Department of Aerospace Engineering at Old Dominion University in August 2007 to pursue his Ph.D. studies on computational fluid dynamics and helicopter aerodynamics. His dissertation work entitled "Modeling and Simulation of Coaxial Helicopter Rotor Aerodynamics" was performed under the supervision of Professor Oktay Baysal. He is currently a Ph.D. candidate at Old Dominion University, a major in the Turkish Air Force, and a student member of the American Institute of Aeronautics and Astronautics.